Università degli Studi di Udine

Dipartimento Politecnico di Ingegneria e Architettura (DPIA)
PhD in Industrial and Information Engineering

THESIS FOR THE DEGREE OF DOCTOR OF PHILOSOPHY

Modeling and Simulation of Ferroelectric-based Devices for Neuromorphic Computing Applications

Supervisor
Prof. David Esseni

Candidate
Mattia Segatto
119913

Academic Years 2020-2022 (XXXVI cycle)

Abstract

In recent years, there has been a growing diffusion of computing systems based on artificial neural networks and artificial intelligence, which can be used in a very wide range of applications. However, these bio-inspired systems are often very energy-intensive due to continuous data transfer between the processing unit and memory; this continuous data transfer is also known as the Von Neumann bottleneck. A new computing paradigm, called neuromorphic computing, suggests to overcome this bottleneck by integrating the logic and memory functionalities within a single chip thus reducing the continuous data and emulating the working principle of biological neural networks.

Memristive devices, which store information in a non-volatile manner as the value of their resistance, have gained appeal as possible hardware candidates to enable neuromorphic computing. Among the many candidates proposed as memristors, one of the most prominent is represented by ferroelectric-based devices. Ferroelectric materials are a sub-class of dielectric materials that possess a hysteretic polarization versus electric field characteristic. The energy required for their operation is significantly lower than it is in competing technologies for memristive applications, thus explaining their appeal in the scientific community.

This thesis aims to study and model the behavior of ferroelectric devices as hardware for neuromorphic computing. This manuscript provides insights into the operation of ferroelectric materials in Ferroelectric Tunnel Junctions, as well as a novel approach to the modeling of antiferroelectric materials within the context of the Landau-Ginzburg-Devonshire framework.

Overall, this work contributes to advancing the understanding and application of ferroelectric devices for energy-efficient computing applications.

Contents

List of Figures

List of Tables

Chapter 1

Introduction

Figure 1.1: Sketch of a Von Neumann and a neuromorphic computing architecture. a) Sketch of the conventional Von Neumann paradigm in which the memory and computational unit are separated, and information travels between them through dedicated buses. In particular the data bus is the origin of the Von Neumann bottleneck [1]. b) Sketch of the hardware organization for neuromorphic computing, where the logic and processing functionalities are integrated inside the memory unit, reducing or eliminating the need for continuous data transfer between such two units.

In recent years there has been a growing diffusion of computing systems that are based on neural networks and artificial intelligence. These bio-inspired computing systems are used in a wide range of applications, such as pattern recognition in data analysis, forecasts in financial and logistic applications, automation of time-consuming and repetitive tasks, medical

1. Introduction

diagnoses, autonomous driving and so on [2].

However, these computing systems are very energy intensive, mainly due to the continuous data transfer between the processing unit and the memory unit [1], [3] (see Fig. 1.1a). This is the so-called Von Neumann bottleneck [1], and its name is due to the homonymous computing architecture, which in fact implies the separation between the CPU and memory unit.

In neuromorphic computing, the logic and memory functionalities are
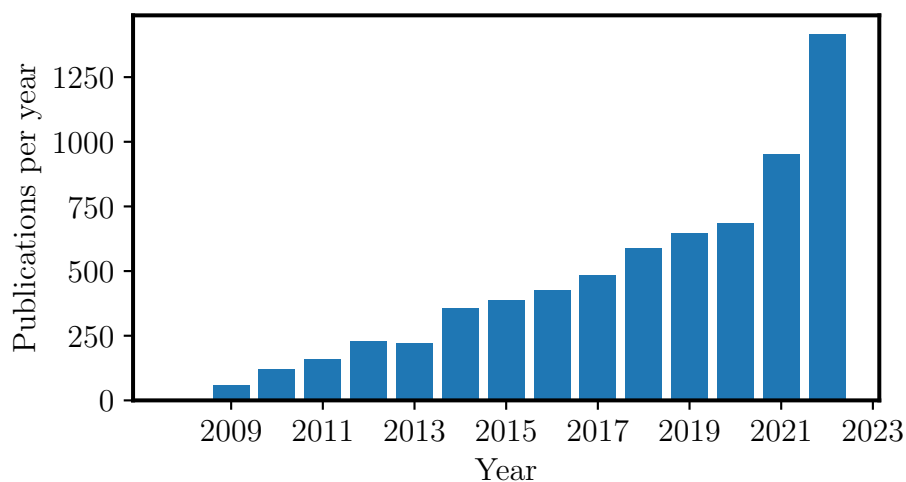
Figure 1.2: Number of academic publications regarding memristors per year, in the time interval 2009-2022. Data from *scopus.com* with research keyword "memristors".

integrated into a single chip (see Fig. 1.1b) thus eliminating the need for continuous data transfer between the two [1], that resembles how biological neural networks work [4], [5]. A sketch of the Von Neumann and neuromorphic computing paradigms is shown in Fig. 1.1.

The most widespread mechanism for information storge is the charge in a static Random Access Memory (SRAM), a dynamic Random Access Memory (DRAM) or flash memory [6]. However, a new class of memory devices is emerging, where the information is stored as a value of resistance rather than the presence of charge, and this class of devices is called memristive devices or memristors.

The memristor was first theorized in 1971 by Leon Chua as the fourth fundamental passive circuit element along with the resistor, capacitor and inductor [7], but only in 2008 it was manufactured by Hewlett-Packard [8]. Memristors are one of the most prominent candidates to enable neuromorphic computing, and the research interest about these devices is steadily growing, as illustrated by Fig. 1.2.

1.1 Memristors as artificial synapses

A biological synapse is the site of transmission of electrical nerve pulses between neurons. This connection allows the communication between neurons, and in particular the synapse is located between the axon of the pre-synaptic neuron and the dendrite of the post-synaptic neuron [9]. Axons and dendrites are the transmitting and receiving ends of neurons, respectively. Neurons possess a membrane potential and when the pre-synaptic neuron generates an action potential, called spike, the synapse is responsible for the transmission of the spike to the dendrites of the receiving neurons (see Fig. 1.3) via the release of neurotransmitters that bind with receptors located on the membrane of the post-synaptic neuron. The strength of the transmission by the synapse, which is modulated by the quantity of neurotransmitters, is modified by the rate or the intensity of the transmitting signal. This property of the synapse is called synaptic plasticity [10], which is believed to play a key role in the formation of short and long-term memories in human beings.

The synaptic plasticity is also called synaptic weight and synapses possess two
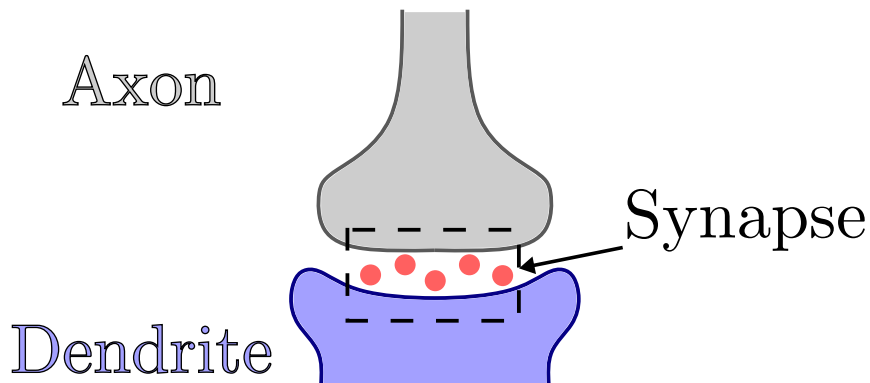
Figure 1.3: Sketch of a biological synapse. The axon is the transmitting end of the pre-synaptic neuron, while the dendrite is the receiving end of the post-synaptic neuron. The synapse is the channel that enables the transmission of signals between the neurons. Usually the synaptic channel is formed by neurotransmitters (red circles), that bind with receptors on the receiving end [11].

types of plasticity: LTP and STP [9]. Under the LTP plasticity it is possible to identify long-term potentiation and depression of the synaptic weight, which refer to a strengthening or weakening of the synaptic connection. In particular, it is believed that long-term potentiation occurs when the synapse is stimulated with a strong or high-frequency stimulus applied to the synapse itself, whereas long-term depression is the result of weak or low-frequency

stimuli [11]. Both long-term potentiation and depression result in a long-lasting change of the synaptic weight. STP, instead, refers to short-term potentiation and depression, which are due to similar mechanisms as their LTP counterpart, but their effect is much more short-lived. In fact, while effects of LTP can last up to a lifetime, STP usually decays after minutes [12].

Memristors represent a promising candidate to realize artificial synapses due to their properties similar to their biological counterpart. Indeed, their resistance represents the synaptic weight which can be changed (ideally in an analog way) by the application of control signals, essentially obtaining the artificial equivalent of synaptic plasticity. Moreover, their retention properties determine their ability to emulate the long-term plasticity of synapses.

1.2 State of the art for memristive devices

Memristors can be classified by their switching mechanism and, in particular, they can be divided into three main categories [13]:

- Conductive filament memristors

- Phase-change memristors

- Electronic effect memristors

1.2.1 Conductive filament memristors: Resistive RAM (ReRAM)

In a filament memristor, the formation and destruction of the conductive filament in the oxide layer of the device switches the memristor between a high-resistance state (HRS) and a low-resistance state (LRS). The processes of formation and destruction of the filament are widely believed to be based on electrochemical metallization, valence change and thermochemical mechanisms. A possible example of conductive filament memristor is given by devices realized with metal oxides such as titanium dioxide (TiO_2), hafnium oxide (HfO_2) or tantalum oxide (Ta_2O_5). These metal oxide-based devices are among the most popular conductive filament memristors, as they are compatible with BEOL integration on chips. These oxides provide a possible implementations of the so-called Resistive-RAM or ReRAM, where the formation of a conductive filament is due to the presence of defects called oxygen vacancies [14], as sketched in Fig. 1.4. ReRAMs can store their resistance in an analog fashion via electrical pulses [15], which translates in the possibility to

a)   b)   c)
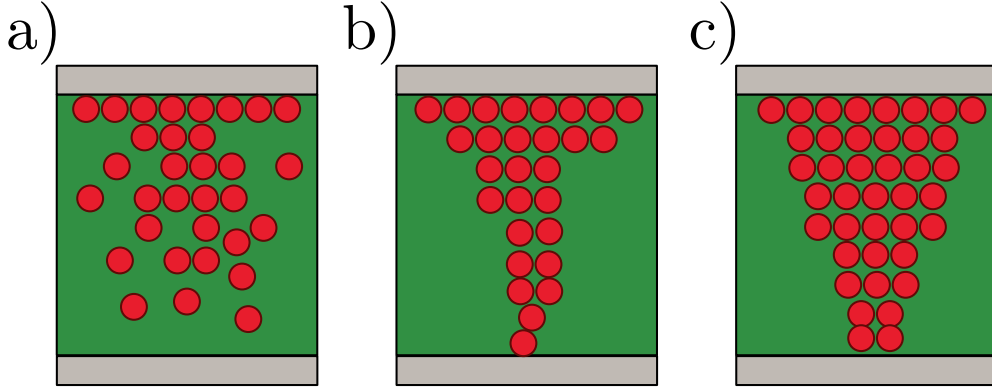
Figure 1.4: Sketch of the working principle for ReRAMs. a) The device is RESET and no conductive filament is present. b) Upon the application of SET pulses, the oxygen vacancies (red circles) redistribute in the oxide creating a conductive path. c) The larger the conductive filament, the lower the resistance of the device.

implement long and short-term potentiation and depression of their synaptic weight.

However, in conductive filament memristors the multi-level operation is not easy to control, the devices tend to suffer from quite severe program and read disturbs and the resistance of these memristors is still too low to support ultra-low energy neuromorphic computing applications [15], [16]. In addition, the physics behind and thus the modelling of their conduction mechanism is still under debate [15], [17].

1.2.2 Phase-change memories

Non-volatile phase-change memories are usually realized with chalcogenide materials [18]. These materials, which are alloys based on the group 16 elements of the periodic table also known as "chalcogen", are alluring for the change in their electronic properties due to the reversible and non-volatile switching between a poly-crystalline and an amorphous phase of their lattice. The change of phase is obtained by heating the materials to either obtain the poly-crystalline state, which is the SET process, or to return to the amorphous state by abrupt cooling after reaching the melting temperature, which is the RESET process [18]. These stable phases lead to a different resistivity of the materials. In fact, when the materials are in the amorphous phase their resistivity is higher, serving as the HRS, and when the materials are in the poly-crystalline phase their resistivity is lower (LRS). One of the most promising features of PCMs is their ability to store a continuum of resistance values upon the application of partial SET or RESET pulses [15],
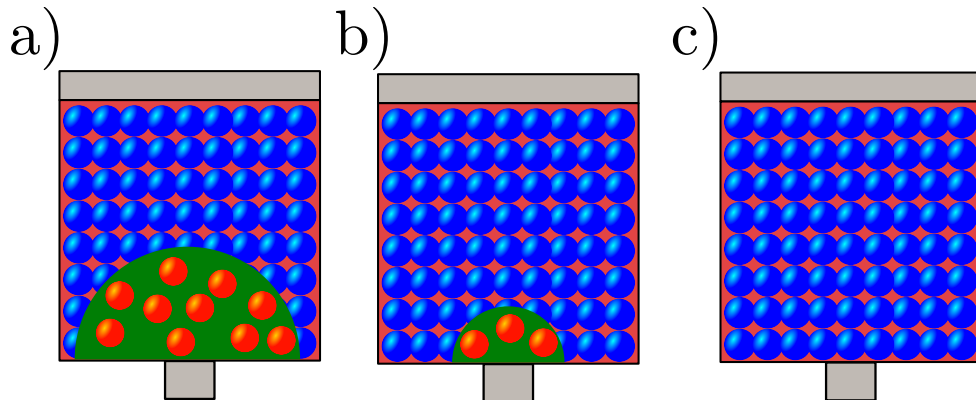
Figure 1.5: Sketch of the working principle for PCMs. a) the device is RESET and two distinct crystal phases are present: poly-crystalline (blue spheres) and amorphous (red spheres). b) by applying SET pulses the amorphous phase is reduced and so is the resistance of the device, until it is no longer present, as shown in c).

[19]. Their ability to store "analog" resistance values facilitates the matrix-vector multiplication on chip, which targets the hardware acceleration of Deep Neural Networks. However, the precision in the setting of the resistance states is severely hindered by the 1/f noise and resistance drift [15], [20]. Another key property of PCMs is the accumulative properties of input signals, which can be leveraged in the training part of Deep Neural Networks, even though the accumulative process has been shown to be highly non-linear and exhibit quite large variability [21].

While PCMs possess very high endurance and retention, two key challenges associated with their exploitation as hardware for neuromorphic computing are given by the high variability of their SET states and their difficult integration into large on-chip arrays [15].

1.2.3 Ferroelectric devices

The working principle of ferroelectric-based memristive devices is based on the change of the ferroelectric spontaneous polarization, which switches the devices from the HRS to the LRS and vice versa.

Ferroelectric FETs (FeFETs) are transistors with a ferroelectric material in the gate stack. By changing the polarization value, the threshold voltage of the device is changed and the source-to-drain current of the device can be modulated (see Figs. 1.6a and 1.6b).
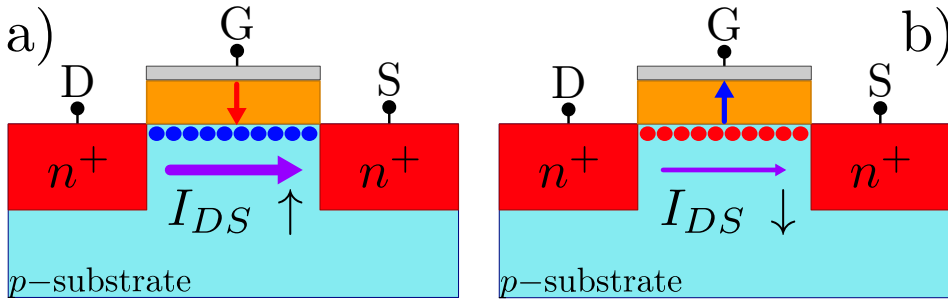
Figure 1.6: Sketch of the working principle of FeFETs. a) When the ferroelectric polarization points towards the channel, it attracts minority carriers forming a conductive path between the source (S) and drain (D) contacts, obtaining a non-negligible current I_{DS}. b) When the polarization points in the opposite direction, the conductive path is dismissed and the current I_{DS} is reduced.

Another ferroelectric-based memristive device is the Ferroelectric Tunnel Junction (FTJ). The device concept for ferroelectric tunnel junctions was first proposed in 1971 by Leo Esaki *et al.* [22] in an embodiment based on a Metal-Ferroelectric-Metal stack. In this first device concept for the Ferroelectric Tunnel, the non-idealities of the metal contacts in terms of the screening length coupled with different polarization states should lead to different effective heights for the tunneling barrier, as depicted in Fig. 1.7. This should result in obtaining a low-resistance state (see Fig. 1.7a) and a high-resistance state (see Fig. 1.7b) of the device, allowing its exploitation as a memristor. Its main limitation, however, resulted from the fact that in order to have large enough current densities the thickness of the ferroelectric layer had to be scaled down to a few nanometers, and only recently it has been possible to fabricate ultra-thin layers which still possess ferroelectric properties [23]–[25]. Currently, one of the most explored architectures for Ferroelectric Tunnel Junctions is the Metal-Ferroelectric-Dielectric-Metal stack (MFDM), where the tunneling occurs through a thin dielectric layer. In this device concept, different polarization states lead to different band profiles
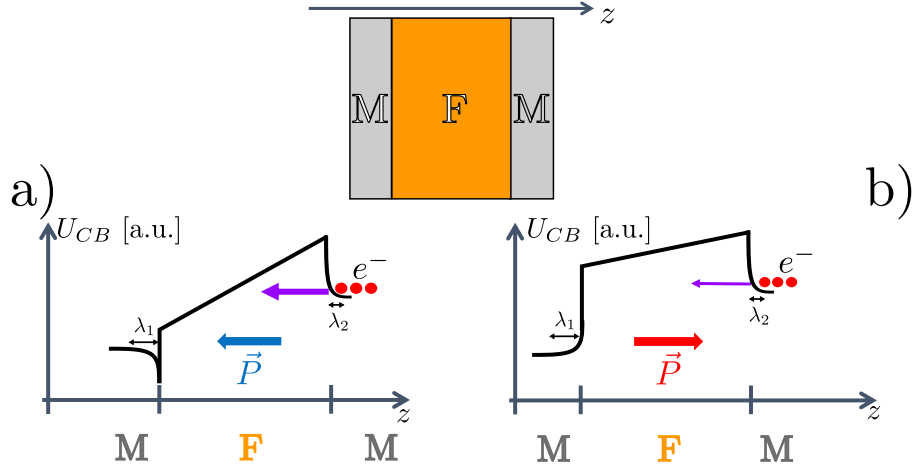
Figure 1.7: Sketch of the working principle of Metal-Ferroelectric-Dielectric-Metal FTJs. Thanks to the different screening lengths of the metal contacts ($\lambda_1 > \lambda_2$) it is possible to obtain an asymmetric band profile for the different directions of the polarization a) depicts the low-resistance state in which the effective tunneling barrier height is lower therefore the tunneling current is higher. b) due to the different screening lengths, the different direction of the polarization results in a higher effective tunneling barrier height which leads to lower values of tunneling current.

in the dielectric stack and thus to different values of tunneling current (see Figs. 1.8a and 1.8b), thus enabling the switching of FTJs from a HRS to an LRS, and vice versa.

Since the operating principle of these devices is supposed to be the tunneling current, it is of paramount importance to model this current correctly. The state of the art regarding tunneling current modeling is based on the WKB approximation [26]–[28]. This approximation is used in its one-dimensional version, which, however, is problematic given the strongly three-dimensional nature of the potential energy profile in the ferroelectric material. Moreover, further study and research are necessary to determine whether it is necessary to include other conduction mechanisms other than tunneling, such as Poole-Frenkel conduction or hopping conduction, in order to have a modeling of the read-out current consistent with the experimental behavior.

The most promising ferroelectric materials proposed for neuromorphic computing are Hafnium-based oxides, which are compatible with CMOS technology fabrication processes. In this respect, FeFET devices having sub 50 ns switching at sub 5 V pulse voltage have been reported [29]. However their application is limited by their relatively low endurance and the challenging scaling below 10 nm thickness that usually leads to a deterioration of the ferroelectric properties of the material [15].

Figure 1.8: Sketch of the working principle of Metal-Ferroelectric-Metal FTJs. a) In FTJs, when the ferroelectric polarization points towards the ferroelectric-dielectric interface, the tunneling is limited by the thin dielectric layer, leading to relatively high values of tunneling current. b) If the polarization points in the opposite direction, the resulting band profile displays a thicker tunneling barrier which in turn leads to lower values of the tunneling current.

Another challenge is posed by the "wake-up" effect and fatigue, which are an increase and decrease of the remanent polarization at low and high cycling, respectively. The ferroelectric "wake-up" and fatigue effects are problematic also for ferroelectric tunnel junctions. The low I_{ON}/I_{OFF} ratio is also a challenge for ferroelectric tunnel junctions, however their small current density makes them suitable for the realization of massively parallel operations, such as matrix-vector multiplications in cross-bar arrays. Hence, ferroelectric tunnel junctions are still perceived as promising candidates for neuromorphic computing applications [15].

1.3 Performance of different memristors

Memristive devices can be evaluated with respect to different metrics. In particular, the essential characteristics that a memristor should have to support neuromorphic computing are [13]:

- dynamic range: it is the ratio between the HRS and LRS, and essentially indicates how stable the operation of the memristor is and how amenable the device is for a multilevel operation;

- linearity: it indicates how linear the response of the memristor is when

its control inputs changes;

- symmetry: it represents how symmetric the $I - V$ characteristic of the memristor is for different polarities of the applied voltage. A high symmetry is desirable because it allows one to use similar electrical stimuli to modulate the resistance for both voltage polarities [13];

- area factor: the smaller the memristor is, the better on-chip integration can be achieved; the higher density can reduce the size and power consumption of the overall device;

- retention: it refers to the ability of the memristor to retain the resistance value over time;

- endurance: it identifies the number of write and erase cycles that a memristor can go through before its performance is degraded;

- switching energy: it is the maximum energy required by the writing and reading operations.

	Charge-based memories			Emerging memristors			
	SRAM	DRAM	FLASH (NAND)	PCM	RRAM	FTJ	FeFET
Area	$150\ F^2$	$6F^2$	$4\ F^2$	$4\text{-}50\ F^2$	$4\text{-}50\ F^2$	$1\text{-}10\ F^2$	$6\text{-}50\ F^2$
Multi-bit	1	1	3-4	2-3	2-3	1	2-3
Read time	1 ns	10 ns	10 μs	10 ns	10 ns	50 ns	50 ns
Write time	1 ns	10 ns	0.1-1 ms	50 ns	100 ns	100 ns	100 ns
Retention	N/A	$\sim$ ms	10 y	10 y	10 y	10 y	1 y
Endurance	10^{16}	10^{16}	10^5	$10^6\text{-}10^9$	$10^3\text{-}10^9$	10^7	$10^6\text{-}10^9$
Switching Energy	$\sim$ fJ	$\sim$ 10 fJ	$\sim$ 10 fJ	$\sim$ 10 pJ	$\sim$ pJ	10 fJ	$\sim$ fJ

Table 1.1: Key features for conventional and emerging memory technologies key features reported in [13], [30]. F is the minimum size of the lithography. Endurance is expressed in number of cycles. The switching energy is referred to the energy required to switch one bit.

Table 1.1 reports a comparison of the key features of several memory technologies and some emerging memristors. As it can be inferred, the emerging memristive technologies offer superior performances in terms of energy consumption with respect to conventional charge-based memories. Among the proposed memristors, ferroelectric devices (in their FTJ or FeFET implementation) represent one of the most promising candidates for ultra-low energy neuromorphic computing. This is the main reason why ferroelectric materials and their device implementation are the core of the research activity detailed in this thesis.

1.4 Purpose of this thesis

This thesis aims to study and model the behaviour of ferroelectric devices used as hardware for neuromorphic computing via numerical simulations based on the Landau-Ginzburg-Devonshire (LGD) theoretical framework. In addition, this thesis proposes to test the applicability of this model to similar materials, namely antiferroelectric materials, and to explore a novel formulation of the LGD model accounting for extrinsic nucleation events, that are not accounted for in the conventional application of the model.

The manuscript is organized as follows. Chapter 2 presents a brief overview on ferroelectric materials history, characteristics and models. Chapter 3 reports a detailed analysis of the behaviour of ferroelectric materials in Ferroelectric Tunnel Junctions. In particular, Chapter 3 deals with a comparison between large signal and small-signal response in C-V and P-V experiments, and with a re-interpretation of the PUND measurements in FTJ stacks. Chapter 4 presents a modified version of the LGD model to provide a physics-based description of antiferroelectricity in novel zirconium oxides. Finally, Chapter 5 proposes a revisitation of the LGD framework for ferroelectric materials accounting for the effect of extrinsic nucleation events, that are not accounted for in the conventional usage of this modelling approach.

1. Introduction

Chapter 2

Modeling of Ferroelectric Materials

Ferroelectric materials are a subclass of dielectric materials that possess both piezoelectric and pyroelectric properties, meaning that their polarization is influenced by mechanical excitations and changes in temperature, respectively. This classification derives from the organization of lattice crystal structures in thirty-two symmetry classes [31]. Out of these thirty-two classes, twenty-one are non-centrosymmetric and, more specifically, twenty of these non-centrosymmetric classes are piezoelectric. Ten of the twenty piezoelectric classes are polar and categorized as pyroelectric and, finally, ferroelectric materials are a subset of pyroelectric materials and are polar (see Fig. 2.1a). The pyroelectric properties of ferroelectric materials manifest through the Curie transition temperature T_C, which is the temperature above which the material is no longer ferroelectric, because its crystal structure undergoes a phase transition from a polar to a non-polar phase.

Ferroelectric materials possess a hysteretic polarization versus applied electric field characteristic where some notable points can be identified: the remanent polarization P_r, which is the polarization value for zero applied electric field, and the coercive field E_C, which is the value of applied electric field that produces a reversal of the spontaneous polarization (see Fig. 2.1b). Ferroelectric behaviour was first reported in 1920s by Valasek in his Ph.D. thesis regarding Rochelle's salts, which were employed for their electro-mechanical properties [32]. During the 1940-1950s, perovskite ferroelectrics (PZT and BTO) were also discovered and concurrently the first phenomenological descriptions of these materials were proposed [33]–[35], but only in 2011 ferroelectricity was observed in hafnium-oxide-based thin films. This was a key discovery for ferroelectric nanoelectronic devices due to the fact that hafnium-based oxides are compatible with CMOS technology fabrication processes, thus enabling
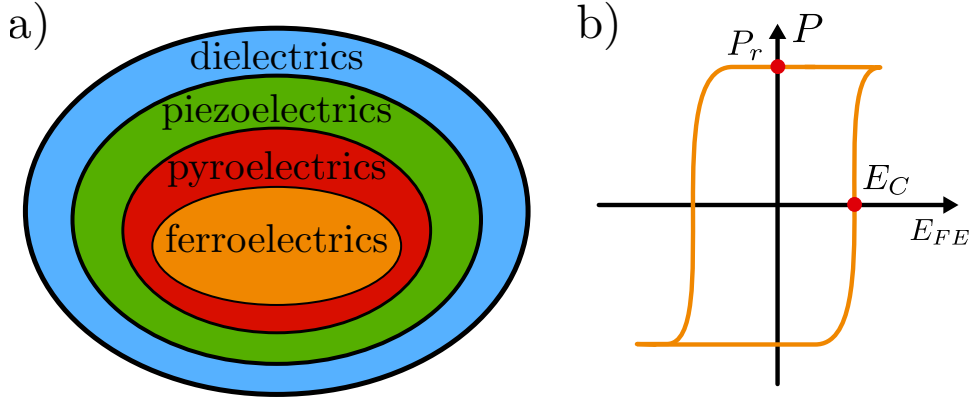
Figure 2.1: a) Definition of sub-classes of dielectric materials. Ferroelectric materials are a particular sub-class of dielectric materials that possess both piezoelectric and pyroelectric properties. b) Hysteretic characteristic of the spontaneous polarization P versus applied electric field E_{FE} of ferroelectric materials. The notable points marked by red bullets are the remanent polarization P_r and the coercive field E_C.

the integration of these newly discovered materials into the Back-End-Of-Line (BEOL) of the wafer.

2.1 Polarization, Depolarization Field and Ferroelectric Domains

As stated in the introduction of this chapter, ferroelectric materials are a specific subset of pyroelectric materials. These materials possess a unit cell lattice that is non-centrosymmetric and supports an electric dipole moment in its unstrained state [36]. This permanent electric dipole is referred to as *spontaneous polarization*. While these characteristics are present in pyroelectric materials as well, the orientability of the dipole moment with the applied electric field is a feature possessed only by ferroelectric materials [36].

The orientability of the spontaneous polarization reasonably suggests that there may be regions of ferroelectric material with the same intensity of spontaneous polarization but with different orientations. We define ferroelectric domains as those regions of ferroelectric material that possess the same intensity and orientation of spontaneous polarization and are separated by an interface called domain wall [36].

We can express the surface charge between two neighboring domains σ_B as [38]:

$$\sigma_B = \boldsymbol{P} \cdot \hat{\boldsymbol{n}} \tag{2.1}$$

Figure 2.2: Orthorhombic unit cell of ferroelectric HfO_2 from [37]; a) and b) depict two possible displacements of the unit cell lattice that give rise to two possible directions of the spontaneous polarization P. In general, the orientation of the polarization is switched with the application of an electric field to the ferroelectric material.

where $\boldsymbol{P}$ is the spontaneous polarization vector and $\hat{\boldsymbol{n}}$ is the versor normal to the surface of the domain wall. Among the many possible arrangements of domain walls, there are two that lead to a net zero surface charge at the interface: one where the polarizations of the domains are anti-parallel and parallel to the domain wall, called 180° domain wall (see Fig. 2.3a), and one where the domain wall interface bisects the angle between two domains pointing head to tail, often called 90° domain wall (see Fig. 2.3b) [38].

While a 180° domain wall poses no concern regarding the strain of the
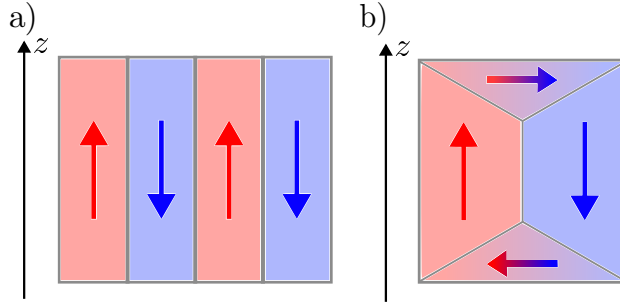
Figure 2.3: Two configurations of domain walls that lead to zero surface charge at the domain wall interface. a) displays the configuration called 180° domain wall where the polarization of the domains is anti-parallel, b) depicts the configuration called 90° domain wall, in which the polarization of a domain points to the tail of its neighbors' polarization.

ferroelectric material, the situation depicted in Fig. 2.3b is far from ideal in terms of strain and in general only certain kinds of domain structures are allowed in the material without introducing dislocations or cracks into the crystal [38].

2. Modeling of Ferroelectric Materials

It is also interesting to mention that in ferroelectric materials the surface polarization charges are screened by electrical charges stemming from impurities, defects, migrating ions and so on. The motion of these charges to the domain walls can provide a mechanism for memory applications [38], [39]. Domain walls can be either soft or hard: a soft domain wall provides a smooth transition between an up-polarized and a down-polarized domain, whereas in the case of a hard domain wall, the transition is abrupt. This distinction arises from thermodynamic considerations stemming from the Landau theory for ferroelectric materials [40] which will be discussed in Section 2.3.
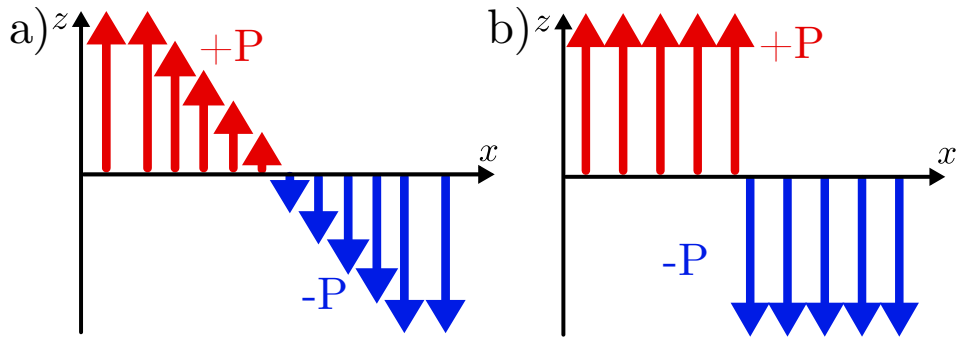
Figure 2.4: Sketch of soft and hard type of domain wall for a simple 2D case. In a) the transition between the "up" state of the spontaneous polarization ($+P$ aligned with the z axis) occurs gradually, depicting a soft domain wall. b) displays an abrupt transition between "up" and "down" domains, which is representative of a hard domain wall.

The presence of spontaneous polarization in the ferroelectric material generates to the so-called depolarization field $\boldsymbol{E_{dep}}$, which in a vacuum can be defined as [41]:

$$\boldsymbol{E_{dep}} = -\frac{\boldsymbol{P}}{\varepsilon_0 \varepsilon_F} \tag{2.2}$$

where $\boldsymbol{P}$ is the spontaneous polarization vector, ε_0 is the vacuum dielectric permittivity and ε_F is the dielectric permittivity of the ferroelectric material. This definition results from the fact that the spontaneous polarization of the ferroelectric is an electric dipole with parallel flat faces that generates an electric field independent of the thickness of the ferroelectric.

If the ferroelectric material is sandwiched between two metal electrodes that are able to perfectly compensate for the spontaneous polarization then the depolarization field can be totally suppressed as shown in Fig. 2.5a. However, it should be remembered that this represents a purely theoretical case, since metals always have a non-zero screening length [42] and therefore, even in a simple metal-ferroelectric-metal (MFM) type capacitor a depolarization field can be developed (see Fig. 2.5b), whose magnitude depends on the screening

length of the metal contact. All the more so, when the ferroelectric material is inserted into stacks that are more complex than an MFM capacitor, such as Ferroelectric FETs or Ferroelectric Tunnel Junctions reported in Chapter 1, the influence of the depolarization field on the behaviour of the stack is more complex and therefore it must be considered and analyzed extensively. Section 3.3 focuses precisely on analyzing the consequences of the presence of the depolarization field in ferroelectric devices designed for neuromorphic computing applications, such as Ferroelectric Tunnel Junctions.
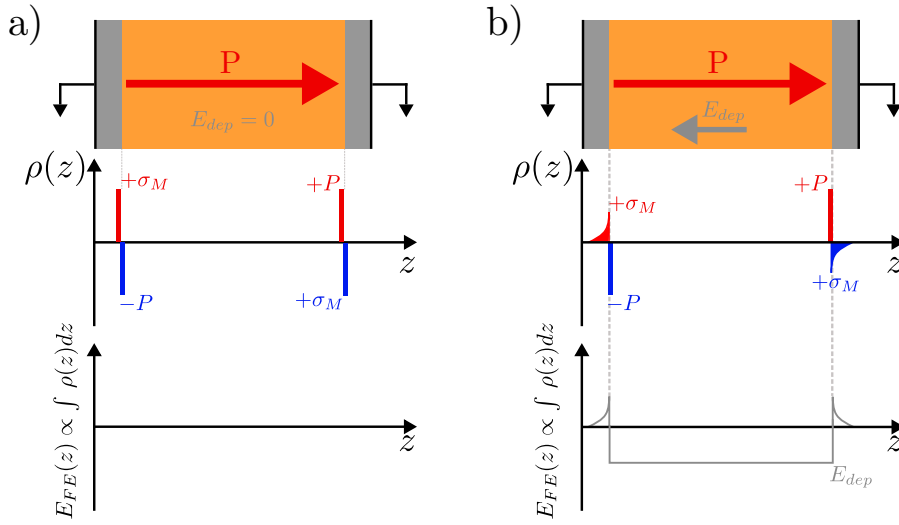
Figure 2.5: Sketch of the depolarization field for a Metal Ferroelectric Metal structure. a) depicts a perfect compensation of the spontaneous polarization when the metal contacts don't have a screening length. b) shows non-ideal metal contacts with a finite screening length resulting in a non–null depolarization field E_{dep}.

2.2 Modeling of Polarization Switching in Ferroelectric Materials

Given the widespread deployment of ferroelectric materials in recent years for various applications, including neuromorphic computing, a good and reliable understanding of the polarization switching mechanisms is of paramount importance[43]. In this respect, many models have been proposed in the past years trying to provide a relation between the applied electric field in the ferroelectric material and the dynamics of the polarization.

One of the first phenomenological models proposed to describe the polarization switching in bulk materials or epitaxial layers is the Kolmogorov-Avrami-Ishibashi (KAI) model [43]. In the context of this model, the polarization switching (also called polarization reversal) is described as the formation of a nucleus, see Fig. 2.6b, and its unrestricted propagation in a crystal with infinite size [44] through the movement of domain walls (see Fig. 2.6c) until the whole layer is flipped to the opposite polarization state [43]. In this model, the dynamics of the polarization switching is therefore limited by the growth and propagation of the nucleated domain.
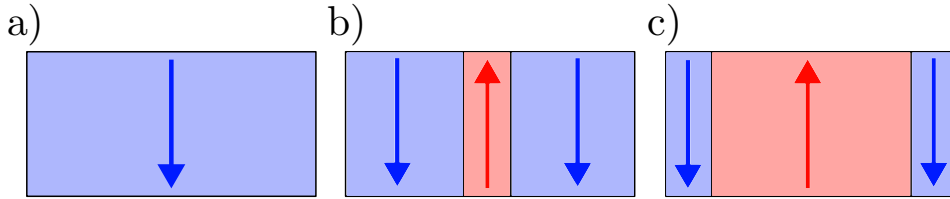
Figure 2.6: Sketch of the polarization switching time evolution in the framework of the KAI model. In a) the stack is completely polarized in the down state. Once a nucleation occurs in b) it can then propagate to the whole stack due to the large dimension of the material's grains, as shown in c).

While this model is valid for bulk materials or epitaxially grown ferroelectrics, it proves to be ineffective in the description of poly-crystalline ferroelectric materials (such as HfO_2-based ferroelectric materials), especially at very low applied electric fields, due to the high amount of defects in such layers [43], [45], [46].

To overcome the limitations of the KAI model, a new formulation has been established where a statistical distribution of the characteristic switching time is introduced, in order to better describe the polarization reversal experiments in ferroelectric thin films that are usually poly-crystalline [47], [48]. In this updated formulation, the KAI-like nucleation and its propagation are still

valid within a grain, but in poly-crystalline films the propagation is stopped rather quickly due to the reduced size of the grains of the material, as depicted in Fig. 2.7c. Therefore, the limiting factor to the complete switching of the whole layer becomes the rate at which nucleations occur in the material rather than their growth.
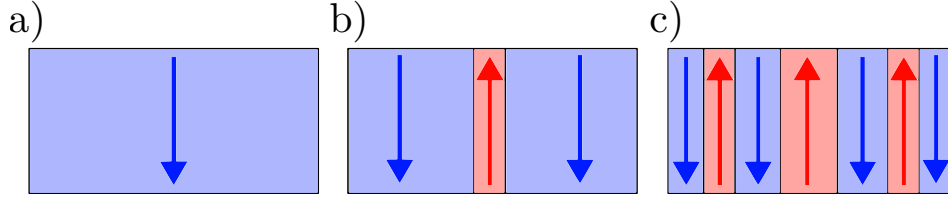
Figure 2.7: Sketch of the polarization switching time evolution in the framework of the NLS model. Once again the stack starts from a down-polarized state. In b) a nucleation occurs, but in this model, due to the large number of grain boundaries, it cannot propagate to the whole film. In c) the first nucleation slightly expanded but did not propagate due to the reduced size of the ferroelectric grains while other nucleations occurred in the film; the rate of these nucleations limits the complete switching of the layer.

In fact, this modeling approach is called Nucleation-Limited Switching (NLS) and is often used to describe polarization switching experiments in poly-crystalline hafnium-based ferroelectric layers [48], [49].

Further details regarding both the KAI and NLS models will be provided in Chapter 5, where they will be compared to a new interpretation of the Landau Theory for ferroelectric modelling, that aims to link nucleation events and their propagation in the ferroelectric layer. In this respect, the Landau Theory is another possible strategy to the modeling of the polarization switching in ferroelectric materials, where now the polarization reversal occurs between two energy minima in each crystal-like domain [43]. It is a homogeneous switching that occurs by means of a progressive change in the direction of the polarization which becomes abrupt once the coercive field of the ferroelectric material is reached, as sketched in Fig. 2.8.

While the Kolmogorov-Avrami-Ishibashi and Nucleation-Limited switching models usually describe the polarization switching under the application of a constant electric field to the ferroelectric material, the Landau Theory coupled with the Landau-Khalatnikov equation [50] can describe the evolution of the polarization under an arbitrary applied electric field. Moreover, the Landau Theory approach is also employed to describe the transient Negative Capacitance behaviour [40], [51]–[53], that is observed in experimental data [54], [55].

Because of its versatility, the Landau Theory-based modeling approach is
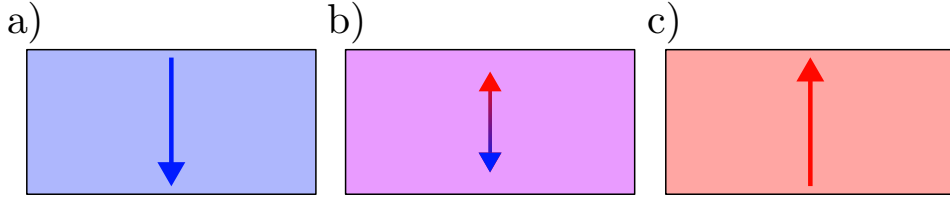
Figure 2.8: Sketch of the polarization switching time evolution in the framework of the Landau Theory. The material is in a down-polarized state in a) and with the application of an electric field it is progressively switched to the up-polarized state, as shown in b). c) Once the applied electric field reaches the coercive field of the ferroelectric material, the switching becomes abrupt.

the cornerstone on which all the simulation results reported in this thesis are based on, and some of its details are provided in the following section.

2.3 Landau Theory for Ferroelectric materials

The Landau theory for the description of ferroelectric materials is based on thermodynamics. In thermodynamics, the macroscopic systems are characterized by quantities that depend uniquely on the equilibrium state of the system, and these quantities are called state functions. The equilibrium states of a system subject to specific constraints minimize or maximize specific functions, that are called thermodynamic potentials [56], [57]. Among the many thermodynamic potentials, the most commonly used one to describe ferroelectric materials is the Gibbs' free energy [58].

By assuming that all vectors are aligned along the thickness of the ferroelectric, the Gibbs' free energy in its differential form can be written using scalar quantities as

$$dg = -D(E_{FE}) \, dE_{FE} \qquad [\text{J/m}^3] \tag{2.3}$$

where D is the electric displacement vector component and E_{FE} is the applied electric field vector component, both aligned along the z axis. In Eq. (2.3) the possible effects of strain and stress are neglected.

The electric displacement can be written as $D(E_{FE}) = P + \varepsilon_0 \varepsilon_F E_{FE}$, where P is the spontaneous polarization vector component aligned with E_{FE}, so that the integral form of Eq. (2.3) is obtained as:

$$g(P, E_{FE}) = g_0 - P E_{FE} - \int_0^{E_{FE}} \varepsilon_0 \varepsilon_F E'_{FE} \, dE'_{FE} = g_0 - P E_{FE} - \frac{1}{2} \varepsilon_0 \varepsilon_F E_{FE}^2. \tag{2.4}$$

Lastly, g_0 can be expressed in the form of the Landau free energy functional, so that the Gibbs' free energy eventually becomes

$$g(P, E_{FE}) = \underbrace{\alpha P^2 + \beta P^4 + \gamma P^6}_{\text{Landau free energy}} - P E_{FE} - \frac{1}{2}\varepsilon_0 \varepsilon_F E_{FE}^2 \qquad (2.5)$$

where α, β and γ are the anisotropy coefficients of the Landau functional. The anisotropy coefficients are typically extracted from a comparison to experiments and, in particular, to reproduce the experimental values of the remanent polarization P_r and the coercive field E_C of the ferroelectric material. Furthermore, the effect of the Curie temperature T_C is usually taken into account in the α parameter, which can be written as:

$$\alpha = \alpha_0(T - T_C) \qquad (2.6)$$

where α_0 is a constant and T is the temperature of the ferroelectric material. When the temperature is lower than the Curie temperature, α is negative, and the material exhibits ferroelectric behaviour. Within the context of the Landau Theory, the disappearance of the polarization when the temperature reaches the Curie temperature is associated to a phase transition. In this respect, we can identify two types of phase transition: first order phase transition and second order phase transition. The distinction between the two types is made on the basis of the trend of the spontaneous polarization as a function of the temperature. If the polarization gradually decreases until it disappears by increasing the temperature, then the phase transition is labelled as second-order, while the phase transition is labelled as first order when the polarization disappears abruptly with the increase of the temperature. In the Landau free energy functional, this distinction is taken into account with the sign of the β anisotropy coefficient: a first order phase transition is described with a negative β value, while a second order phase transition is described with a positive β. In this thesis, we did not conduct a temperature phase transition analysis on the ferroelectric materials examined. Instead, we utilized the three anisotropy coefficients of the Landau theory as fitting parameters.

In the above discussion, it is always assumed that the polarization is homogeneous in the ferroelectric material. However, in ferroelectric films this is rarely the case, and usually the polarization is uniform only in certain regions of the materials, whose dimensions are comparable to the grains of poly-crystalline materials [59], and are named ferroelectric domains. When the polarization is not uniform, an additional energy term called domain wall energy u_{DW} has

to be added to the Gibbs' free energy which becomes

$$g_T(P, E_{FE}) = \alpha P^2 + \beta P^4 + \gamma P^6 - PE_{FE} + \underbrace{k|\nabla P|^2}_{=u_{DW}} - \frac{1}{2}\varepsilon_0\varepsilon_F E_{FE}^2 \qquad (2.7)$$

The domain wall term implies an energy penalty for non-uniform polarization configurations in the ferroelectric layer and, depending on the value of the domain wall coupling k, this term leads to the configuration of two possible cases regarding the domain wall: soft domain walls and hard domain walls [40]. A soft domain wall implies a gradual transition of the polarization between the up (i.e. aligned with the z axis) and down polarization state, while a hard domain wall is present whenever the transition between the two possible polarization states is abrupt [40], [51].
Equation (2.7) is the equation used in the so-called Landau-Ginzburg-Devonshire (LGD) modeling framework, which is used throughout this thesis to describe the polarization dynamics of ferroelectric materials.

2.4 Metal-Ferroelectric-Dielectric-Metal stack

One of the most common device architecture is the Metal-Ferroelectric-Dielectric-Metal (MFDM) stack, which is used for Ferroelectric Tunnel Junctions and also in Negative Capacitance operation experiments [1], [55]. Chapter 3 will report simulations for this device architecture.
Ferroelectric materials in MFDM stacks are described with the Gibbs' free
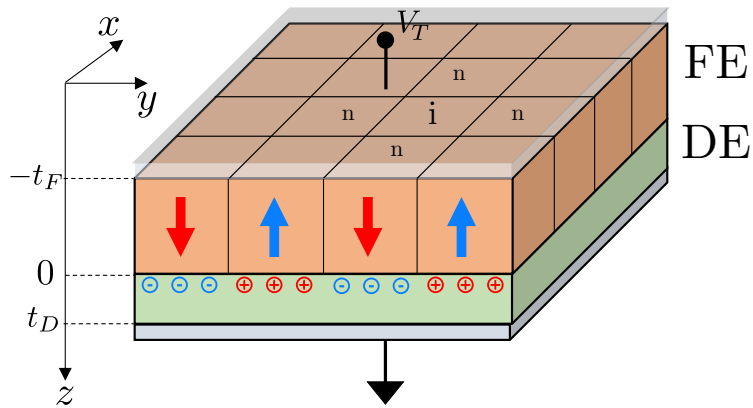
Figure 2.9: Sketch of the Metal-Ferroelectric-Dielectric-Metal stack. The ferroelectric layer has thickness t_F and background dielectric permittivity ε_F, resulting in a capacitance per area $C_F = \varepsilon_0\varepsilon_F/t_F$; the dielectric layer has thickness t_D and dielectric permittivity ε_D, resulting in a capacitance per area $C_D = \varepsilon_0\varepsilon_D/t_D$.

energy already introduced in the previous section, but its electrostatic component is modified due to the presence of the dielectric layer.

For a homogeneous polarization case, the continuity condition for the electric displacement at the ferroelectric-dielectric interface and the link between the external voltage V_T and the electric field in the dielectrics result in:

$$\varepsilon_0\varepsilon_D E_D = P + \varepsilon_0\varepsilon_F E_{FE}$$

$$V_T = t_F E_{FE} + t_D E_D$$

(2.8)

where t_D e t_F are the thicknesses of the dielectric and ferroelectric, respectively (see Fig. 2.9). From Eq. (2.8) it is possible to extract the expressions for the electric field in the ferroelectric and dielectric (E_{FE} and E_D, respectively):

$$E_{FE} = \frac{1}{t_F C_0}\left(C_D V_T - P\right)$$

$$E_D = \frac{1}{t_D C_0}\left(C_F V_T + P\right)$$

(2.9)

In Eq. (2.9), C_D and C_F are the capacitances of the dielectric and the ferroelectric layer defined as $C_D = \varepsilon_0\varepsilon_r/t_D$, $C_F = \varepsilon_0\varepsilon_F/t_F$ and their sum is denoted as $C_0 = C_D + C_F$.

The electrostatic component of the Gibbs' free energy in the homogeneous case is [53]:

$$\mathcal{U}_{EL} = \frac{1}{2}PV_D + \frac{\varepsilon_0\varepsilon_F}{2}E_{FE}V_T = \frac{P^2}{2C_0} + \frac{V_T^2 C_S}{2} \quad [\text{J/m}^2] \qquad (2.10)$$

where C_S is the series capacitance between C_D and C_F.

The battery term for the Gibbs' free energy is

$$\mathcal{U}_B = -V_T\, P_T = -V_T\left(P + \varepsilon_0\varepsilon_F E_{FE}\right) = -PV_T\frac{C_D}{C_0} - V_T^2 C_s \quad [\text{J/m}^2] \quad (2.11)$$

where $P_T = P + \varepsilon_0(\varepsilon_F - 1)E_{FE} \simeq P + \varepsilon_0\varepsilon_F E_{FE}$.

The overall surface Gibbs' free energy is, therefore, the sum of the Landau free energy, the electrostatic term and the battery term

$$\mathcal{G}_{T,MFDM} = \left(\alpha P^2 + \beta P^4 + \gamma P^6\right)t_F + \frac{P^2}{2C_0} + \frac{V_T^2 C_S}{2} - \left(PV_T\frac{C_D}{C_0} + V_T^2 C_S\right)$$

(2.12)

where α, β and γ are the anisotropy coefficients for the Landau free energy, that are usually extracted from experiments to match the remanent polarization P_r and the coercive field E_C.

The dynamics equation for the spontaneous polarization of a ferroelectric material is obtained with the Landau-Khalatnikov equation (LKE) [50] which, for the homogeneous case, can be written as:

$$t_F \rho \frac{\partial P}{\partial t} = -\frac{\partial \mathcal{G}_{T,MFDM}}{\partial P} \tag{2.13}$$

By deriving the total energy expressed in Eq. (2.12) with respect to the spontaneous polarization P, the dynamics for the homogeneous case results in:

$$t_F \rho \frac{\partial P}{\partial t} = -t_F \left(2\alpha P + 4\beta P^3 + 6\gamma P^5 \right) - \frac{P}{C_0} + \frac{C_D}{C_0} V_T \tag{2.14}$$

For the non-homogeneous polarization case, the Gibbs' free energy also contains a term related to the domain wall energy [53], and the resulting dynamics equation for the polarization is the following:

$$t_F \rho \frac{\partial P_i}{\partial t} = - \left(2\alpha_i P_i + 4\beta_i P_i^3 + 6\gamma_i P_i^5 \right) t_F +$$
$$- \left[t_F \frac{k}{w} \frac{d}{(d+w)^2} \sum_{n,i} (P_i - P_{n,i}) \right] \tag{2.15}$$
$$- \left[\frac{1}{2} \sum_{j=1}^{n_D} \left[\frac{1}{C_{i,j}} + \frac{1}{C_{j,i}} \right] (P_j + Q_{S,j}) - \frac{V_T}{2} \left(B_i + 1 + \frac{C_D}{C_0} \right) \right]$$

where k is the domain wall coupling factor, w is the domain wall width, d is the fixed domain size, the $C_{i,j}$ terms are the capacitive coupling between ferroelectric domains through the dielectric layer and $Q_{S,j}$ represents the trapped charge for the $j-$th domain. A derivation of Eq. (2.15) can be found in [53], [60] with some details also provided in Appendix A.

2.5 Double Dielectric Stack

Another stack configuration where ferroelectric materials are employed is the Metal-Dielectric-Ferroelectric-Dielectric-Metal stack. These architectures have been used, for example, for Negative Capacitance applications [52], [61], [62]. Chapter 4 of this thesis also reports a study based on this device structure.
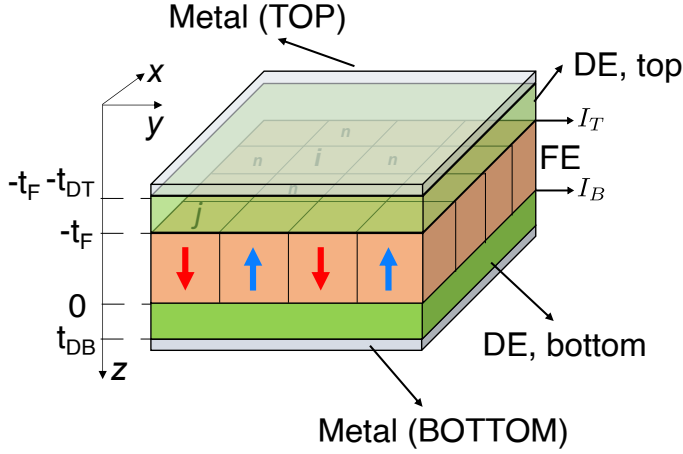
Figure 2.10: 3D sketch of the MDFDM stack where the thicknesses t_{DT} and t_{DB} of the top and bottom dielectrics, respectively, are indicated. $C_{DT} = \varepsilon_0 \varepsilon_{DT}/t_{DT}$ represents the capacitance of the top layer, $C_{DB} = \varepsilon_0 \varepsilon_{DB}/t_{DB}$ the corresponding capacitance of the bottom layer, $C_F = \varepsilon_0 \varepsilon_F/t_F$ is the capacitance associated to the background permittivity of the ferroelectric layer. The interface between the top dielectric (DE,top) and the ferroelectric layer is denoted I_T while the interface between the bottom dielectric (DE, bottom) and the ferroelectric layer is called I_B.

Starting from the homogeneous picture, for a stack composed as in Fig. 2.10, the continuity conditions for the electric displacement at the interfaces between the materials and the link between the external voltage V_T and the electric field in the dielectrics result in:

$$\varepsilon_0 \varepsilon_{DB} E_{DB} - \varepsilon_0 \varepsilon_F E_{FE} = P \tag{2.16}$$

$$\varepsilon_0 \varepsilon_{DT} E_{DT} = P + \varepsilon_0 \varepsilon_F E_{FE} \rightarrow \varepsilon_0 \varepsilon_{DT} E_{DT} - \varepsilon_0 \varepsilon_F E_{FE} = P \tag{2.17}$$

$$V_T = t_{DB} E_{DB} + t_F E_{FE} + t_{DT} E_{DT} \tag{2.18}$$

From Eq. (2.16) and Eq. (2.17) it is possible to obtain the relationship between the electric fields in the top and bottom dielectrics:

$$E_{DT} = \frac{\varepsilon_{DB}}{\varepsilon_{DT}} E_{DB} \tag{2.19}$$

By substituting in Eq. (2.18) we have

$$V_T = E_{DB} t_{DB} \left[1 + \frac{\varepsilon_0 \varepsilon_{DB}}{t_{DB}} \left(\frac{C_F + C_{DT}}{C_F C_{DT}} \right) \right] - \frac{P}{C_F} \tag{2.20}$$

25

2. Modeling of Ferroelectric Materials

Therefore E_{DB} is:

$$E_{DB} = \frac{V_T + \dfrac{P}{C_F}}{t_{DB}\left[1 + C_{DB}\left(\dfrac{C_F + C_{DT}}{C_F C_{DT}}\right)\right]} \tag{2.21}$$

With Equation (2.21) the voltage of each layer can be calculated as:

$$V_{DB} = \left(\frac{C_S}{C_{DB}}V_T + \frac{C_S}{C_{DB}C_F}P\right) \tag{2.22a}$$

$$V_{DT} = \left(\frac{C_S}{C_{DT}}V_T + \frac{C_S}{C_{DT}C_F}P\right) \tag{2.22b}$$

$$V_{FE} = \frac{C_S}{C_F}V_T - \frac{C_S}{C_{DB}C_F}\left(1 + \frac{C_{DB}}{C_{DT}}\right)P \tag{2.22c}$$

$$V_{IT} = V_T - V_{DT} = \left(1 - \frac{C_S}{C_{DT}}\right)V_T - \frac{C_S}{C_{DT}C_F}P \tag{2.22d}$$

where the capacitances per unit area are defined in caption of Fig. 2.10 and V_{IT} is the electrostatic potential at the interface between the top dielectric and the ferroelectric material (I_T in Fig. 2.10).
It is now possible to write the electrostatic term for the stack $\mathcal{U}_{EL}$ as

$$\mathcal{U}_{EL} = \frac{1}{2}PV_{DB} - \frac{1}{2}V_{IT} + \frac{1}{2}V_T\varepsilon_0\varepsilon_{DT}E_{DT}$$

$$= \frac{1}{2}P\frac{C_S}{C_{DS}}V_T + \frac{1}{2}\frac{C_S}{C_F C_{DS}}P^2 - \frac{1}{2}PV_T + \frac{1}{2}V_T\varepsilon_0\varepsilon_{DT}E_{DT} \tag{2.23}$$

where C_{DS} is defined as the series capacitance between C_{DT} and C_{DB}. Now, the battery term $\mathcal{U}_B$ is evaluated as:

$$\mathcal{U}_B = -V_T\varepsilon_0\varepsilon_{DT}E_{DT} \tag{2.24}$$

which combined with Eq. (2.23) results in:

$$\mathcal{U}_{EL} + \mathcal{U}_B = \frac{1}{2}P\frac{C_S}{C_{DS}}V_T + +\frac{1}{2}\frac{C_S}{C_F C_{DS}}P^2 - \frac{1}{2}PV_T+$$

$$+ \frac{1}{2}V_T\varepsilon_0\varepsilon_{DT}E_{DT} - V_T\varepsilon_0\varepsilon_{DT}E_{DT} =$$

$$= \frac{1}{2}P\frac{C_S}{C_{DS}}V_T + \frac{1}{2}\frac{C_S}{C_F C_{DS}}P^2 - \frac{1}{2}PV_T - \frac{1}{2}V_T\underbrace{\frac{\varepsilon_0\varepsilon_{DT}}{t_{DT}}}_{=C_{DT}}\underbrace{E_{DT}t_{DT}}_{=V_{DT}}$$

$$= \frac{1}{2}\frac{C_S}{C_F C_{DS}}P^2 - \frac{1}{2}PV_T\left[\underbrace{1 - \frac{C_S}{C_{DS}}}_{=\frac{C_S}{C_F}} + \frac{C_S}{C_F}\right] - \frac{1}{2}C_S V_T^2$$

$$= \frac{1}{2}\frac{C_S}{C_F C_{DS}}P^2 - PV_T\frac{C_S}{C_F} - \frac{1}{2}C_S V_T^2 \qquad (2.25)$$

To test the validity of the expressions derived so far, it is possible to let the top dielectric thickness tend to zero to obtain the following:

$$\lim_{t_{DT}\to 0} C_{DT} \to +\infty$$

$$\lim_{t_{DT}\to 0} C_S = \frac{C_F C_{DB}}{C_F + C_{DB}}$$

$$\lim_{t_{DT}\to 0} C_{DS} = C_{DB}$$

$$\lim_{t_{DT}\to 0} \frac{C_S}{C_F} = \frac{C_{DB}}{C_F + C_{DB}}$$

$$\lim_{t_{DT}\to 0} \frac{C_S}{C_{DS}} = \frac{C_F}{C_F + C_{DB}}$$

$$\lim_{t_{DT}\to 0} \mathcal{U}_{EL} + \mathcal{U}_B = \frac{1}{2}\frac{P^2}{C_F + C_{DB}} - PV_T\frac{C_{DB}}{C_F + C_{DB}} - \frac{1}{2}\frac{C_F C_{DB}}{C_F + C_{DB}}V_T^2 \quad (2.26)$$

2. Modeling of Ferroelectric Materials

As it can be seen, Eq. (2.26) is coincident with the sum of Eq. (2.10) and Eq. (2.11). Therefore, the overall Gibbs' free energy density g for the homogenous case of the MDFDM stack is the sum of Eq. (2.25) and the Landau free energy component related to the ferroelectric material. Similarly to Section 2.4, the dynamics equation can be extracted with the Landau-Khalatnikov theory [63]:

$$t_F \rho \frac{\partial P}{\partial t} = -t_F \frac{\partial G}{\partial P}$$
$$t_F \rho \frac{\partial P}{\partial t} = -\left(2\alpha t_F + \frac{1}{C_{IFI}}\right) P - 4t_F \beta P^3 - 6t_F \gamma P^5 + \frac{C_S}{C_F} V_T \qquad (2.27)$$

with $G = \int_A g \, d\boldsymbol{r}$, C_{IFI} is defined as

$$\frac{1}{C_{IFI}} = \frac{C_{DT} + C_{DB}}{C_{DT}C_{DB} + C_{DT}C_F + C_F C_{DB}} \qquad (2.28)$$

and the variational derivative $\delta G/\delta P$ is evaluated as explained in Section 2.3. For the non-homogeneous polarization picture in the MDFDM stack, the electrostatic energy components can be expressed as:

$$\mathcal{U}_{IB} = \sum_{j=1}^{n_D} \int_{IB_j} \frac{P_j V_{IB}(\mathbf{r})}{2} d\mathbf{r} \qquad (2.29)$$

$$\mathcal{U}_{IT} = \sum_{j=1}^{n_D} \int_{IT_j} \frac{-P_j V_{IT}(\mathbf{r})}{2} d\mathbf{r} \qquad (2.30)$$

$$\mathcal{U}_B = -V_T \int_A \varepsilon_0 \varepsilon_{DT} E_{TM}(\mathbf{r}) d\mathbf{r} \qquad (2.31)$$

$$\mathcal{U}_{TM} = \frac{V_T}{2} \int_A \varepsilon_0 \varepsilon_{DT} E_{TM}(\mathbf{r}) d\mathbf{r} \qquad (2.32)$$

$$\mathcal{U}_B + \mathcal{U}_{TM} = -\frac{V_T}{2} \int_A \varepsilon_0 \varepsilon_{DT} E_{TM}(\mathbf{r}) d\mathbf{r} \qquad (2.33)$$

with $\mathcal{U}_{IB}$, $\mathcal{U}_{IT}$, $\mathcal{U}_B$ and $\mathcal{U}_{TM}$ being the energy related to the bottom interface, top interface, battery and top metal, respectively, with I_{Tj}, $I_{B,j}$ being the

top and bottom interface of the $j-$th domain. The quantities $E_{TM}(\mathbf{r})$, $V_{IB}(\mathbf{r})$ and $V_{IT}(\mathbf{r})$ can be expressed as

$$\varepsilon_0 \varepsilon_{DT} E_{TM}(\mathbf{r}) = C_S V_T + \varepsilon_0 \varepsilon_{DT} \sum_{h=1}^{n_D} P_h G_{TM,h}(\mathbf{r}) \tag{2.34}$$

$$V_{IB}(\mathbf{r}) = V_{DB}(\mathbf{r}) = \frac{C_S}{C_{DB}} V_T + \sum_{h=1}^{n_D} P_h G_{IB,h}(\mathbf{r}) \tag{2.35}$$

$$V_{IT}(\mathbf{r}) = V_T \left(1 - \frac{C_S}{C_{DT}} \right) + \sum_{h=1}^{n_D} P_h G_{IT,h}(\mathbf{r}) \tag{2.36}$$

where $G_{TM,h}$, $G_{IT,h}$ and $G_{IB,h}$ are defined as Green's functions of a pair of charges, a positive $+P$ charge at the bottom interface I_B and a negative $-P$ charge at the top interface I_T. The sum of the energies related to the top and bottom interfaces can be written as

$$\frac{1}{d^2} \left[\mathcal{U}_{IB} + \mathcal{U}_{IT} \right] = \frac{1}{2} \sum_{j=1}^{n_D} P_j V_T \left(\frac{C_S}{C_{DS}} - 1 \right) + \frac{1}{2} \sum_{j,h}^{n_D} \frac{P_j P_h}{C_{jh}} \tag{2.37}$$

where C_{jh} is defined as $1/C_{jh} = (1/C_{jh}^{(IB)} + 1/C_{jh}^{(IT)})$ and $C_{jh}^{(I_B)}$, $C_{jh}^{(I_T)}$ are expressed via the Green's functions as

$$\frac{1}{C_{jh}^{I_B}} = \frac{1}{d^2} \int_{I_{Bj}} G_{IB,h}(\mathbf{r}) > 0 \tag{2.38}$$

$$\frac{1}{C_{jh}^{I_T}} = \frac{-1}{d^2} \int_{I_{Tj}} G_{IT,h}(\mathbf{r}) > 0 \tag{2.39}$$

and represent the electrostatic coupling between ferroelectric domains through the dielectric layers. The battery and top metal energy terms can be summed as well

$$\frac{1}{d^2} \left[\mathcal{U}_{TM} + \mathcal{U}_B \right] = -\frac{V_T}{2} \left[C_S V_T \underbrace{\frac{A}{d^2}}_{n_D} + \sum_{h=1}^{n_D} P_h B_h \right] \tag{2.40}$$

with the term B_h defined with a Green's function as well

$$B_h = \frac{\varepsilon_0 \varepsilon_{DT}}{d^2} \int_A G_{TM,h}(\mathbf{r}) d\mathbf{r} \tag{2.41}$$

Therefore, the overall expression for the electrostatic energy is

$$U_{ET} = -\frac{1}{2}C_S V_T^2 n_D - \frac{V_T}{2}\sum_{j=1}^{n_D} P_j\left(1 + B_j - \frac{C_S}{C_{DS}}\right) + \frac{1}{2}\sum_{j,h}^{n_D}\frac{P_j P_h}{C_{jh}} \quad (2.42)$$

With the overall Gibbs' free energy and by using the relation $t_F \rho\, \partial P_i/\partial t = -t_F \delta G/\delta P_i$ [63] where again $G = \int_A g\, d\boldsymbol{r}$ is the integral over the area of the overall Gibbs' free energy, the dynamics equation can be readily obtained for the MDFDM stack similarly to Section 2.4 by using Eq. (2.42) as the total energy expression:

$$t_F \rho \frac{\partial P_i}{\partial t} = -\left(2\alpha P_i + 4\beta P_i^3 - 6\gamma P_i^5\right)t_F +$$

$$-\left[t_F \frac{2\,k}{d^2}\sum_{n,i}(P_i - P_{n,i})\right] + \quad (2.43)$$

$$-\left[\frac{1}{2}\sum_{j=1}^{n_D} P_j\left(\frac{1}{C_{i,j}} + \frac{1}{C_{j,i}}\right) - \frac{V_T}{2}\left(1 + B_i - \frac{C_S}{C_{DS}}\right)\right]$$

2.5.1 MDFDM stack with interface charges
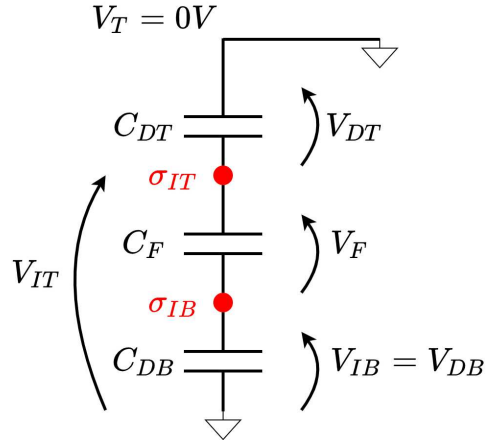
Figure 2.11: Equivalent circuit resulting from setting $V_T = P = 0$. The capacitances are defined in caption of Fig. 2.10. σ_{IT} and σ_{IB} are the fixed charges at the interfaces I_B and I_T.

Considering for the sake of simplicity the single domain case, it is possible to understand the contribution that two fixed charges at the interfaces, σ_{IT}

and σ_{IB} produce on the equations of the device stack. Solving the circuit demonstrates that the resulting expressions for the voltages across the layers are

$$V_{DB} = V_{IB} = \frac{C_S}{C_{DB}}V_T + \frac{C_S}{C_{DB}C_F}P + \frac{C_F}{C_{DB}+C_F}\frac{Q_{IT}}{C_{IT}} + \frac{Q_{IB}}{C_{IB}} \tag{2.44}$$

$$V_{IT} = \left(1 - \frac{C_S}{C_{DT}}\right)V_T - \frac{C_S}{C_{DT}C_F} + \frac{Q_{IT}}{C_{IT}} + \frac{C_F}{C_{DT}+C_F}\frac{Q_{IB}}{C_{IB}} \tag{2.45}$$

$$V_{FE} = \frac{C_S}{C_F}V_T - \frac{C_S}{C_{DB}C_F}\left(1 + \frac{C_{DB}}{C_{DT}}\right)P + \frac{Q_{IT}}{C_{IT}}\frac{C_{DB}}{C_{DB}+C_F} +$$
$$- \frac{Q_{IB}}{C_{IB}}\frac{C_{DT}}{C_{DT}+C_F} \tag{2.46}$$

with $C_{IT} = C_{DT} + C_{S,FDB}$ where $1/C_{S,FDB} = (1/C_F + 1/C_{DB})$ and C_{IB} is defined by exchanging the subscripts T with B and vice versa.

It is fairly easy to extend the contribution of the fixed charges to the multi-domain case, in fact, since the effects of the fixed charges are independent of the position, Eqs. (2.34) to (2.36) can be easily rewritten as

$$\varepsilon_0\varepsilon_{DT}E_{TM}(\mathbf{r}) = C_S V_T - \frac{C_{DT}}{C_{IT}}Q_{IT} - \frac{C_{DT}C_F}{C_{DT}+C_F}\frac{Q_{IB}}{C_{IB}} +$$
$$+ \sum_{h=1}^{n_D} P_h G_{TM,h}(\mathbf{r}) \tag{2.47}$$

$$V_{IB}(\mathbf{r}) = \frac{C_S}{C_{DB}}V_T + \frac{C_F}{C_{DB}+C_F}\frac{Q_{IT}}{C_{IT}} + \frac{Q_{IB}}{C_{IB}} + \sum_{h=1}^{n_D} P_h G_{IB,h}(\mathbf{r}) \tag{2.48}$$

$$V_{IT}(\mathbf{r}) = V_T\left(1 - \frac{C_S}{C_{DT}}\right) + \frac{Q_{IT}}{C_{IT}} + \frac{C_F}{C_{DT}+C_F}\frac{Q_{IB}}{C_{IB}} +$$
$$+ \sum_{h=1}^{n_D} P_h G_{IT,h}(\mathbf{r}) \tag{2.49}$$

and the same can be done for Eqs. (2.37) and (2.40)

$$\frac{1}{d^2}\left[\mathcal{U}_{IB} + \mathcal{U}_{IT}\right] = \frac{1}{2}\sum_{j=1}^{n_D} P_j \left[\left(\frac{C_S}{C_{DS}} - 1\right)V_T + \frac{Q_{IT}}{C_{IT}}\frac{C_{DB}}{C_{DB} + C_F} - \right. \tag{2.50}$$

$$\left. +\frac{Q_{IB}}{C_{IB}}\frac{C_{DT}}{C_{DT} + C_F} + \sum_{h=1}^{n_D}\frac{P_h}{C_{jh}}\right]$$

$$\frac{1}{d^2}\left[\mathcal{U}_{TM} + \mathcal{U}_B\right] = -\frac{V_T}{2}\left[C_S V_T n_D - \frac{C_{DT}}{C_{IT}}Q_{IT}n_D - \right. \tag{2.51}$$

$$\left. +\frac{C_{DT}C_F}{C_{DT} + C_F}\frac{Q_{IB}}{C_{IB}}n_D + \sum_{h=1}^{n_D}P_h B_h\right]$$

Overall, the resulting electrostatic term of the energy is

$$\mathcal{U}_{ET} = -\frac{C_S V_T^2}{2}n_D + \frac{V_T}{2}\left(\frac{C_{DT}}{C_{IT}}Q_{IT} + \frac{C_{DT}C_F}{C_{DT} + C_F}\frac{Q_{IB}}{C_{IB}}\right)n_D -$$

$$+\frac{V_T}{2}\sum_{j=1}^{n_D}P_j\left(1 + B_j - \frac{C_S}{C_{DS}}\right) +$$

$$+\frac{1}{2}\sum_{j=1}^{n_D}P_j\left(\frac{Q_{IT}}{C_{IT}}\frac{C_{DB}}{C_{DB} + C_F} - \frac{Q_{IB}}{C_{IB}}\frac{C_{DT}}{C_{DT} + C_F}\right) + \frac{1}{2}\sum_{j,h=1}^{n_D}\frac{P_j P_h}{C_{jh}} \tag{2.52}$$

From Eq. (2.52) it is evident that, if the structure is perfectly symmetric and the fixed charges at the two interfaces are equal, then they do not contribute to the dynamics of the structure and Eq. (2.52) reduces to Eq. (2.42).

Chapter 3

Ferroelectric Tunnel Junctions based on MFDM stacks

3.1   Introduction

Thanks to the discovery of a robust ferroelectricity in hafnium oxide thin films [37], several intriguing applications of ferroelectricity in CMOS electron devices have been proposed and are being presently scrutinized. Device concepts include nanoscale CMOS FETs exploiting the effective negative capacitance to improve the sub–threshold swing [64]–[69] as well as Ferroelectric Tunnel Junctions (FTJs) [70], [71] and ferroelectric FETs [72], [73], which may be used as non–volatile memories or as memristors for neuromorphic computing applications [1]. In fact, differently from most memristors, the ferroelectric polarization switching is not inherently driven by a current flow, but the polarization reversal is instead induced by an electric field, thus leading to a very energy-efficient switching operation.

Quite understandably, a dependable determination of the ferroelectric spontaneous polarization P is of primary importance in ferroelectric materials and ferroelectric-based electron devices, and in general the experimental characterization and sound modelling for large and small–signal regime are both paramount for an optimal design of ferroelectric devices. The multi–domain Landau, Ginzburg, Devonshire (LGD) theory is well credited for the ferroelectric dynamics, and it has been used for negative capacitance effects [52], [53], [74]–[76], as well as for the operation of FTJs [77] and of FeFETs [78].

33

3.2 Simulation Framework

The simulation framework has been in-house developed and comprises models for the ferroelectric dynamics, a dynamic equation for the traps at the FE-DE interface and a description of a tunnelling injection from the MF and MD electrodes to the traps. The dynamics of the ferroelectric
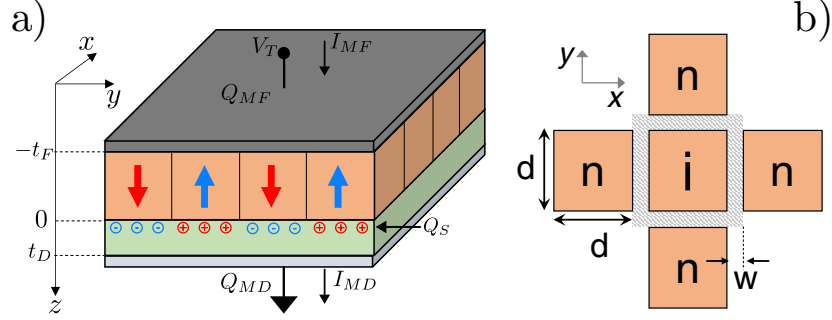
Figure 3.1: a) Three–dimensional sketch of an MFDM capacitor, where t_F and t_D are the ferroelectric and dielectric thicknesses, and V_T is the external bias. The neighboring domains of the i-th domain are indicated with n and they are included in the domain wall term of Eq. (3.1). The spontaneous polarization, P, is taken positive when it points to the dielectric. Q_{MF}, I_{MF}, Q_{MD}, I_{MD} denote the charges and currents at the MF and MD electrodes, respectively, with Q_S being the trapped charge at the ferroelectric-dielectric interface. b) Neighbours of the i-th domain, d is the domain size and w is the domain wall width. These parameters are involved in the domain wall energy.

domains is described by a formulation of the multi-domain Landau-Ginzburg-Devonshire (LGD) model and the minimization of an energy functional which was thoroughly discussed in the Chapter 2 of this thesis. The equation that describes the temporal evolution of the domain-wise polarization in the model is the following

$$
\begin{aligned}
t_F\, \rho\, \frac{\partial P_i}{\partial t} = & -\left(2\alpha_i\, P_i + 4\beta_i\, P_i^3 + 6\gamma_i\, P_i^5\right) t_F + \\
& - t_F \frac{k}{w} \frac{d}{(d+w)^2} \sum_n (P_i - P_n) + \\
& - \frac{1}{2} \sum_{j=1}^{n_D} \left(\frac{1}{C_{i,j}} + \frac{1}{C_{j,i}}\right) \cdot (P_j + Q_{S,j}) + \frac{C_D}{C_0} V_T
\end{aligned}
\tag{3.1}
$$

where α, β, γ are the anisotropy constants, ρ denotes the resistivity that sets a time scale $t_\rho = \rho/(2|\alpha|)$ for the ferroelectric switching and $Q_{S,j}$ denotes the trapped charge for the j-th domain. Moreover, the parameters $1/C_{i,j}$

describe the depolarization energy and depolarization field in the MFDM structure, with $C_{i,j}$ being the electrostatic coupling between the i–th and j–th domains that occurs through the dielectric layer. The capacitances $C_{i,j}$ are evaluated with a 3D description of the structure by an electrostatic solver that is based on the finite elements method [53]. The solver is used to extract the capacitance coupling between domains for all the structures reported in this thesis. Moreover, k and w are the domain wall coupling factor and the domain wall width involved in the formulation of the domain wall energy (see also Fig. 3.1b) and here it was assumed that $d + w \simeq d$.

The charge trapping model follows a first-order dynamic equation for the
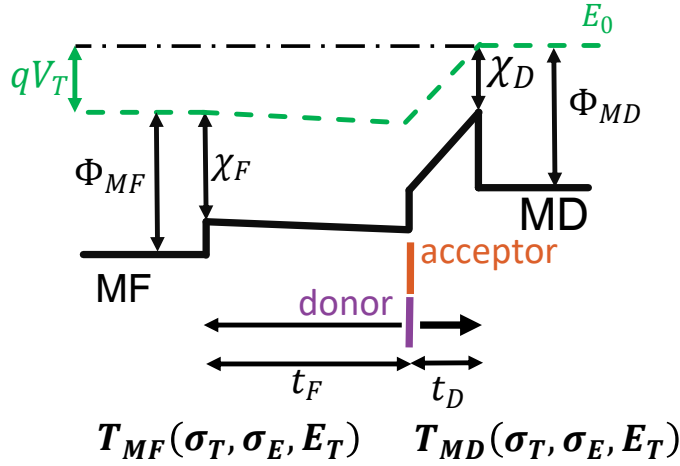
Figure 3.2: Sketch of the band diagram in an MFDM stack, where χ_D, χ_F are the electron affinity of the dielectric and ferroelectric material, while Φ_{MD}, Φ_{MF} are the workfunctions of the MD and MF electrodes. The energy position of acceptor and donor type traps is also depicted. The tunnelling coefficients T_{MD} and T_{MF} depend on the energy, σ_E, and geometric, σ_T, cross sections of the traps, as well as on the traps energy E_T [79].

occupation f_T of either acceptor or donor type traps at the FE-DE interface. By denoting with c_{MD0}, c_{MF0} the capture rate from the MD and MF metal electrodes the equation governing f_T can be written as

$$\frac{\partial f_T}{\partial t} = c_{MD0} \left[f_{0,MD} - f_T \right] + c_{MF0} \left[f_{0,MF} - f_T \right] \qquad (3.2)$$

where $f_{0,M}(E_T) = 1/[1 + \exp\left((E_T - E_{f,M})/(K_B T)\right)]$ is the Fermi occupation function in the metal electrodes, with $E_{f,MF} = E_{f,MD} - qV_T$. In the derivation of Eq. (3.2) a detailed balance condition was imposed, ensuring that the steady state f_T value at the equilibrium (i.e. for $V_T = 0$ V) is given by the Fermi function. The capture rates were attributed to tunnelling from and to the electrodes. One possible approach to the description of the tunnelling

35

transmission is to use a WKB approximation [80] that involves the tunnelling effective mass m_D, m_F in the two dielectrics, and the area and energy cross sections σ_T [m^2], σ_E [eV]:

$$c_{M-0}(E_T) = \sigma_T \sigma_E \frac{m_\parallel}{2\pi^2\hbar^3} \int\limits_0^{+\infty} T_{M-}(E_T - \varepsilon)d\varepsilon, \tag{3.3}$$

where T_{M-} represent the transmission coefficient from either the MF contact or MD contact (as depicted in Fig. 3.2) calculated with the WKB approximation. Equation (3.3) assumes an effective mass approximation in the metal electrodes and an energy separability $E = E_\perp + \varepsilon(\mathbf{k})$, with the transverse energy $\varepsilon(\mathbf{k})$ being conserved in the tunnelling process [81]. Here $m_\parallel$ corresponds to an effective mass for the density of states of the metals. In the absence of a better $m_\parallel$ determination, in calculations we used the popular assumption $m_\parallel \approx m_0$ [82].
Another possible approach in the description of the capture and emission rates, which is more phenomenological and less physics-based, is to use a fixed value of the parameter c_{M-0}, that thus becomes independent of the trap energy [53]. Although this is a simpler description of the tunneling from metal contacts, it provides better results in the linearization of the LGD model, as it will be discussed later in this section. More details about the trapping and tunnelling models may be found in [79].

From the occupations f_T one can readily calculate the charges Q_{acc} and Q_{don} respectively in acceptor and donor type traps, which can be written as:

$$Q_{acc} = \frac{-q}{n_D} \sum_{E_T} N_{acc} f_T(E_T) \Delta E, \tag{3.4a}$$

$$Q_{don} = \frac{q}{n_D} \sum_{E_T} N_{don} \left(1 - f_T(E_T)\right) \Delta E, \tag{3.4b}$$

where N_{acc}, N_{don} denote the trap densities and ΔE is the energy step between the discrete trap levels. The overall interface trapped charge is finally given by $Q_S = (Q_{acc} + Q_{don})$.
The knowledge of the time dependent polarization and trapped charge, in turn, allows one to numerically calculate all the quantities discussed in Section 3.3.1, such as I_{MF}, P_{AV}, $Q_{S,AV}$, and also $I_{MF,QS}$, $Q_{MF,QS}$.

3.3 Large Signal Analysis

This section focuses on the large-signal characterization of ferroelectric materials used in FTJs. In particular, in large–signal regime, the most common experimental technique to determine the spontaneous polarization P of a ferroelectric material is the so-called Positive-Up-Negative-Down (PUND) measurement technique, which was originally devised for Metal-Ferroelectric-Metal (MFM) structures [38], [83] (see also PUND waveforms in Fig. 3.3), and it is still used also in Metal-Ferroelectric-Dielectric-Metal (MFDM) device structures [84]–[87]. The main goal of the PUND technique for an MFM structure is an accurate determination of the ferroelectric remanent polarization, i.e. the spontaneous polarization for zero applied electric field. Given that a ferroelectric material possesses two possible polarization states, experiments cannot but extract the difference between the polarization of these two states, which is usually referred to as $2P_r$.

In an MFM stack with ideal metal electrodes the electric field can be set to zero by applying a null external voltage, and the PUND technique was essentially developed to minimize the contributions to $2P_r$ due to the background polarization induced by the electric field and to possible leakage currents (see also the discussion in Section 3.3.1). In an MFDM structure, however, the ferroelectric field cannot be directly imposed by an external applied voltage due to the presence of the depolarization field. Therefore, the application of the PUND technique to MFDM devices is not straightforward in several respects. In fact, the interpretation of PUND measurements performed for an MFDM stack can lead to artifacts and inaccuracies regarding the extracted remanent polarization of the ferroelectric layer. Theory and application of PUND measurements in MFDM structures are revisited in this section by using both analytical derivations and a comprehensive modelling framework, that has been previously validated and calibrated against experiments [79], [88].

3.3.1 Charge and current at the electrodes in the MFDM structure

In Figure 3.1 an MFDM structure is sketched, where $\boldsymbol{r} = (x, y)$ and z are the coordinate in the plane of the ferroelectric-dielectric interface and in the direction normal to the interface, while Q_{MF}, Q_{MD} are the charges per unit area at the MF and MD electrodes, respectively (see Figure 3.1). The electrostatic problem is linear if a perfect screening in the metal electrodes si assumed, consequently Q_{MF}, Q_{MD} can be written in terms of appropriate
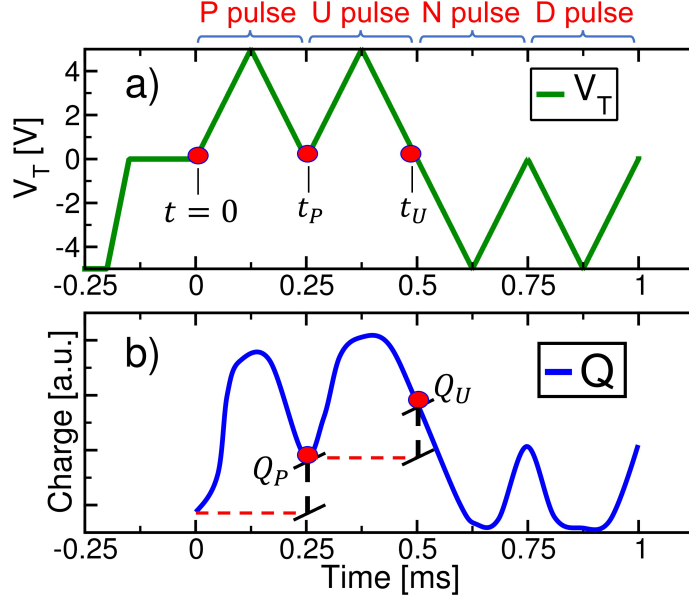
Figure 3.3: a) Examples of the V_T waveform used in PUND measurements. The 250 μs pulse width has been used in all the simulation results reported in Section 3.3.2 (so $t_U = 2t_P$), if not otherwise stated. A preset pulse at $V_T = -5$ V and for 125 μs is used to set an initial negative polarization state; b) Charge waveform sketch during the PUND simulation. Some key points are defined in order to simplify the notation of the thesis. (©2021 IEEE)

Green's functions for the charges in the structure. More specifically, for Q_{MF}

$$Q_{MF}(t) = \frac{1}{A} \int_A P(\mathbf{r}, t)\, d\mathbf{r} + \frac{1}{A} \int_A \varepsilon_0 \varepsilon_F\, E_{FT}(\mathbf{r}, t) d\mathbf{r} \qquad (3.5)$$

where A is the device area, P is the ferroelectric spontaneous polarization, $E_{FT}(\mathbf{r}, t)$ denotes the z component of the electric field at the position $\mathbf{r}$ of the MF-FE interface (located at $z=-t_F$).

At any time t, the $E_{FT}(\mathbf{r}, t)$ is determined by the external bias V_T and by the charges in the dielectric stack, whose position is denoted by $(\boldsymbol{r}_0, z0)$. More specifically, the depolarization field at the MF-FE interface $E_{DP}(\mathbf{r}, t)$ is here defined as the field produced by the distribution of the total charge $[P(\mathbf{r}_0, t) + Q_S(\mathbf{r}_0, t)]$ at the FE-DE interface located at $z = 0$, where $Q_S(\mathbf{r}_0, t)$ is an interface charge due to fixed Coulomb centers or to interface traps. Similarly, $E_\rho(\mathbf{r}, t)$ is defined as the field produced by the remaining charge densities $\rho(\mathbf{r}_0, z_0, t)$ in the dielectric stack at $z_0 \neq 0$. The $E_{FT}(\mathbf{r}, t)$ can thus be written as

$$\varepsilon_0 \varepsilon_F\, E_{FT}(\mathbf{r}, t) = C_S\, V_T + \varepsilon_0 \varepsilon_F [\, E_{DP}(\mathbf{r}, t) + E_\rho(\mathbf{r}, t)\,] \qquad (3.6)$$

where $C_S = (1/C_D + 1/C_F)^{-1}$, with $C_D = \varepsilon_0 \varepsilon_D/t_D$, $C_F = \varepsilon_0 \varepsilon_F/t_F$ and t_D,

ε_D being the thickness and relative permittivity of the dielectric, and t_F, ε_F being the thickness and background permittivity of the ferroelectric (see Figure 3.1). By substituting Equation (3.6) in Equation (3.5) we obtain

$$
\begin{aligned}
Q_{MF}(t) =& C_S\, V_T(t) + P_{AV}(t) + \\
&+ \varepsilon_0 \varepsilon_F\, E_{DP,AV}(t) + \varepsilon_0 \varepsilon_F\, E_{\rho,AV}(t)
\end{aligned}
\tag{3.7}
$$

where P_{AV}, $E_{DP,AV}$ and $E_{\rho,AV}$ denote respectively the average polarization and average fields at the MF-FE interface. From Appendix B it can be inferred that the average E_{DP} and E_ρ can be written as:

$$
\varepsilon_0 \varepsilon_F\, E_{DP,AV} = \frac{1}{A} \int_A [P(\mathbf{r}_0) + Q_S(\mathbf{r}_0)]\, G_{MF}(\mathbf{r}_0, z_0)\, d\mathbf{r}_0
\tag{3.8a}
$$

$$
\varepsilon_0 \varepsilon_F\, E_{\rho,AV} = \frac{1}{A} \int_A \int_{-t_F}^{t_D} \rho(\mathbf{r}_0, z_0)\, G_{MF}(\mathbf{r}_0, z_0)\, dz_0\, d\mathbf{r}_0
\tag{3.8b}
$$

where $G_{MF}(\mathbf{r}_0, z_0)$ is the Green's function defined as

$$
G_{MF}(\mathbf{r}_0, z_0) = \frac{\varepsilon_0 \varepsilon_F}{e} \int_A E_{FT,\boldsymbol{r}_0, z_0}(\boldsymbol{r})\, d\mathbf{r} \; .
\tag{3.9}
$$

with $E_{FT,\boldsymbol{r}_0,z_0}(\boldsymbol{r})$ being the field $E_{FT}(\mathbf{r})$ produced by a point charge e located at $(\mathbf{r}_0, z_0)$. Appendix B.1 reports the demonstration that, under realistic assumptions, the $G_{MF}(\mathbf{r}_0, z_0)$ for the MFDM structure in Figure 3.1 is independent of $\mathbf{r}_0$ and it can be evaluated analytically. For a charge located at the FE-DE interface, for example, we have $G_{MF}(\mathbf{r}_0, 0) \simeq -(C_F/C_0)$, which allows to rewrite Equation (3.8a) as

$$
\varepsilon_0 \varepsilon_F\, E_{DP,AV} \simeq -\frac{C_F}{C_0}(P_{AV} + Q_{S,AV})
\tag{3.10}
$$

At any $z_0 \neq 0$ the $G_{MF}(\mathbf{r}_0, z_0)$ can be similarly expressed with a z_0 dependent capacitance ratio. Since PUND measurements are based on the integral of the transient current at the electrodes, by definition only the variations of the polarization and charges in the device stack can be extracted from experiments. Below the discussion is carried out in terms of the current I_{MF} at the MF terminal, however in Appendix B.1 the corresponding expression for I_{MD} is also derived and the results reported in this section apply also to I_{MD}. In the presence of a charge trapping distributed throughout the device, it is difficult to express the influence of $\rho(\mathbf{r}_0, z_0, t)$ on I_{MF}, because

39

Equation (3.8b) shows that the information about the distribution along z_0 is required. Consequently, hereafter the picture is simplified by assuming that the time derivative of the charge trapped in the dielectric stack is dominated by the $(\partial Q_S/\partial t)$ term due to traps at the FE-DE interface, which implies $\partial E_{\rho,AV}/\partial t \ll \partial E_{DP,AV}/\partial t$. It is also assumed that $Q_S(t)$ can change only through the terminal currents $I_{QS,MF}$, $I_{QS,MD}$ shown in Figure 3.4, and I_{lkg} denotes a possible leakage current, not contributing to trapping. Consequently, the current at the MF electrode can be written as
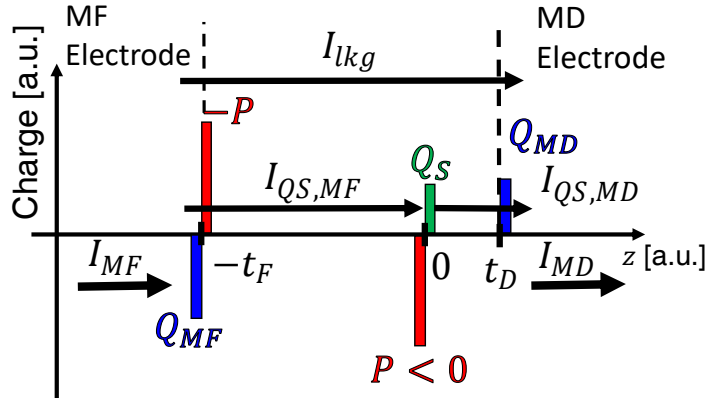
Figure 3.4: Sketch of the sheet charges in the MFDM structure of Figure Fig. 3.1, where Q_{MF}, Q_{MD} denote the overall charges at the electrodes. The picture illustrates an example corresponding to a negative polarization P and a positive interface charge Q_S. $I_{QS,MF}$ and $I_{QS,MD}$ denote the currents due to trapping and de-trapping at the FE-DE interface, and I_{lkg} is a possible leakage current through the whole structure. I_{MF}, I_{MD} denote the overall currents at the electrodes (see Equation (3.11)), that are used in the PUND characterization technique. (©2021 IEEE)

$$
\begin{aligned}
I_{MF} =& \frac{\partial Q_{MF}}{\partial t} + I_{QS,MF} + I_{lkg} = C_S \frac{\partial V_T}{\partial t} + \frac{\partial P_{AV}}{\partial t} \\
& + \varepsilon_0 \varepsilon_F \frac{\partial E_{DP,AV}}{\partial t} + I_{QS,MF} + I_{lkg} = \\
=& C_S \frac{\partial V_T}{\partial t} + \frac{C_D}{C_0} \frac{\partial P_{AV}}{\partial t} - \frac{C_F}{C_0} \frac{\partial Q_{S,AV}}{\partial t} + I_{QS,MF} + I_{lkg}
\end{aligned}
\tag{3.11}
$$

where Q_{MF} has been expressed via Equation (3.7) assuming $\partial E_{\rho,AV}/\partial t \ll \partial E_{DP,AV}/\partial t$, and the last equality is obtained via Eq. (3.10).

By considering the Positive (P) pulse of a PUND experiment starting at $t = 0$ s with $V_T(0) = 0$ V (see the waveform in Fig. 3.3(a)), the charge $Q_P(t)$ (with $0 \leq t \leq t_P$) can be evaluated by integrating the expression for I_{MF} in

Eq. (3.11), obtaining

$$Q_P(t) = \int_0^t I_{MF}(t') \, dt' \approx$$
$$\approx C_S V_T(t) + P_{AV}(t) + \varepsilon_0 \varepsilon_F E_{DP,AV}(t) +$$
$$+ Q_{QS,MF}(t) + Q_{lkg}(t) \tag{3.12}$$

where $Q_{QS,MF}$ and Q_{lkg} are the integral of $I_{QS,MF}$ and I_{lkg}, respectively. It is also understood that the quantities P_{AV}, $E_{DP,AV}$ and $Q_{QS,MF}$ in Equation (3.12) denote the variations from the corresponding values at $t = 0$ or, equivalently, that Equation (3.12) conventionally assumes $P_{AV} = E_{DP,AV} = Q_{S,MF} = Q_{MF} = 0$ at $t = 0$. The charges $Q_U(t)$, $Q_N(t)$, $Q_D(t)$ during respectively the Up (U), Negative (N) and Down (D) pulses of the PUND technique have expressions equivalent to Equation (3.12).

The first and last term at the right–hand side of Eq. (3.12) are the contributions due to the background linear polarization of the dielectrics and the leakage. Even in an MFM structure these contributions complicate the extraction of the remanent polarization $2P_r = P_{AV}(t = t_P)$, and PUND measurements address this issue by subtracting from Q_P the charge Q_U during the U pulse at the same external bias V_T. In the theoretical framework, such an approach results in the charge $Q_{PU} = (Q_P - Q_U)$, that can be written as

$$Q_{PU} \approx \left(P_{AV}^{(P)} - P_{AV}^{(U)} \right) + \left[\varepsilon_0 \varepsilon_F \left(E_{DP,AV}^{(P)} - E_{DP,AV}^{(U)} \right) \right] +$$
$$+ \left(Q_{QS,MF}^{(P)} - Q_{QS,MF}^{(U)} \right) + \left(Q_{lkg}^{(P)} - Q_{lkg}^{(U)} \right) \tag{3.13}$$

where the superscripts (P), (U) identify the P and U pulse and all charges are evaluated at times corresponding to the same V_T value during either a rising or a falling V_T ramp. As already mentioned about Eq. (3.12), the P_{AV}, $E_{DP,AV}$ and $Q_{QS,MF}$ in Eq. (3.13) denote the variations from the corresponding values at the beginning of either the P or the U pulse. The second and third term in the right–hand side of Equation (3.13) are due to the depolarization field and the current at the MF electrode contributing to trapping at the FE-DE interface, respectively.

In an MFM structure both these terms are negligible and, moreover, it is typically assumed that the polarization state can be stabilized after the P pulse due to the screening provided by the metal contacts, so that $P_{AV}^{(U)}$ is much smaller than $P_{AV}^{(P)}$. Furthermore, it is also usually assumed that the leakage affects the measurements to a similar extent during the P and U pulse, leading to $Q_{lkg}^{(U)} \approx Q_{lkg}^{(P)}$ [89]. Under these circumstances Equation (3.13) shows that the Q_{PU} in an MFM stack can be interpreted as the $P_{AV}^{(P)}$ that is

41

the quantity to be determined in experiments.

In an MFDM structure, instead, the terms in Eq. (3.13) due to the depolarization field can be comparable to $P_{AV}^{(P)}$, and the term $(Q_{QS,MF}^{(P)} - Q_{QS,MF}^{(U)})$ may also give a sizeable contribution to Q_{PU}. Hence in an MFDM stack the interpretation of Q_{PU} and the determination of $P_{AV}^{(P)}$ appear much more delicate than in the MFM counterpart. This is systematically investigated in Section 3.3.2 by using numerical simulations.

3.3.2   Simulation results and Discussion

The goal of the PUND measurements is to accurately determine the spontaneous polarization switched by the external bias, which is very challenging in an MFDM structure due to the depolarization field and the possible charge trapping. In this section, numerical simulations are used to investigate the possible errors and artifacts produced by PUND measurements in MFDM structures, and to provide some useful physical insights. Numerical simula-

α [m/F]	β [m^5/C^2/F]	γ [m^9/C^4/F]
$-4.8 \cdot 10^8$	$1.46 \cdot 10^9$	$3.14 \cdot 10^{10}$
ε_F	ε_D	m_F [m_0]
34	10	0.4
m_D [m_0]	σ_T [cm^2]	σ_E [eV]
0.18	$1 \cdot 10^{-15}$	$7 \cdot 10^{-3}$
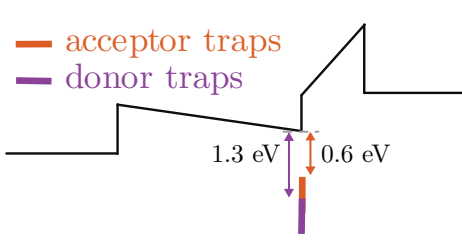
Table 3.1: Material parameters used in simulations for the Hf$_{0.5}$Zr$_{0.5}$O$_2$−Al$_2$O$_3$ MFDM system. Here α, β and γ are the mean values of the anisotropic constants which follow a Gaussian distribution, and calculations include domain to domain variations of the α_i, β_i, γ_i parameters (with i=1, 2, ..., n_D) corresponding to a ratio $\sigma_{EC} = 10\%$ between the standard deviation and the mean value of the coercive field E_C. m$_D$ and m$_F$ are the effective tunnelling masses for respectively Al$_2$O$_3$ and HZO, while σ_E, σ_T denote respectively the energy and geometric cross section of the traps, that are used in the tunnelling model. The maximum energy values for the traps are 0.6 and 1.3 eV below the conduction band minimum at the FE-DE interface for acceptor and donor traps, respectively. Both traps type extend in energy uniformly for 2 eV below their maximum. The electron affinity was set to $\chi_D = 1.4$ eV for Al$_2$O$_3$ [90] and to $\chi_F = 2.4$ eV for HZO [91], while the workfunction for both TiN metal electrodes was taken as $\Phi_M = 4.5$ eV [92].

tions emulate PUND measurements with a 1 kHz waveform and a 5 V peak voltage in an MFDM structure with different dielectric thicknesses t_D and trap densities N_{acc} and N_{don}. The ferroelectric HZO layer is 10 nm thick in all simulations. The mean values for α, β and γ used in simulations are reported in Table 3.1 and lead to remanent polarization and coercive field values that

are representative of a Hafnium-Zirconium-Oxide (HZO) ferroelectric, which is the ferroelectric most widely used in FTJs. In all simulations the domain wall coupling k was set to zero, by following recent first principles calculations for HfO$_2$ [93]. Moreover, a resistivity $\rho = 115$ Ωm is assumed, which is consistent with recently reported values for Hafnium-Zirconium (HZO) based capacitors [94], [95], and results in a time scale for the ferroelectric dynamics $t_\rho \approx 119.8$ ns. All simulations include $n_D = 1024$ domains and the domain size d is 5 nm; it was verified that results are insensitive to a further increase of n_D. The values of m_D, m_F, σ_T, σ_E used in simulations are reported in Table 3.1.

A possible leakage current flowing directly from MD to MF is not taken into account in this discussion, because it's likely that leakage is strongly technology-dependent, frequently governed by Poole-Frenkel and hopping mechanisms in the HZO and, as such, difficult to describe in simulations [96]. Moreover, while it is understood that a failure of the condition $Q_{lkg}^{(U)} \approx Q_{lkg}^{(P)}$ can induce artifacts in PUND experiments even in an MFM stack, this issue goes beyond the scope of this analysis, that is focused on the influence that the depolarization field and charge trapping have on the results of PUND measurements in MFDM structures.

Figure 3.5 reports simulation results for $t_D = 1.5$ nm and for different trap densities. The Q_{PUND} is here defined as either $Q_{PU} = (Q_P - Q_U)$ or $Q_{ND} = (Q_N - Q_D)$, respectively for the positive and negative V_T values. The interface charge $Q_{S,AV}$ typically has a sign opposite to the polarization, and Figure 3.5 reports $-Q_{S,AV}$, which together with P_{AV} determines $E_{DP,AV}$ according to Equation (3.10). All charges in Figure 3.5 are referred to the corresponding value at the beginning of the P pulse, namely at $t = 0$ s and $V_T = 0$ V in Figure 3.3. The Q_{PUND} in Figure 3.5a shows a hysteresis loop that is much more tilted and stretched than in the corresponding MFM curves (filled triangles). The features for an MFDM are similar to those experimentally observed in the P-V curves for an HZO capacitor serially connected to a discrete ceramic capacitor ensuring a negligible charge injection [97], or to measurements in MFDM structures with thicker Al$_2$O$_3$ layers [52]. In fact, the relatively low density of traps in Figure 3.5a results in an interface charge Q_S (green diamonds) that is practically negligible compared to the ferroelectric polarization (red squares). The lack of any compensation of the polarization results in a large depolarization field $E_{DP,AV}$ (see Equation (3.10)), which in turn leads to a vast discrepancy between Q_{PUND} and P_{AV}. In fact, Figure 3.5a shows that for $|V_T|$ above about 4 V a complete polarization switching occurs. Nevertheless, the corresponding Q_{PUND} is much smaller than P_{AV}, mainly because the $E_{DP,AV}$ term in Equation (3.13) subtracts from the P_{AV}
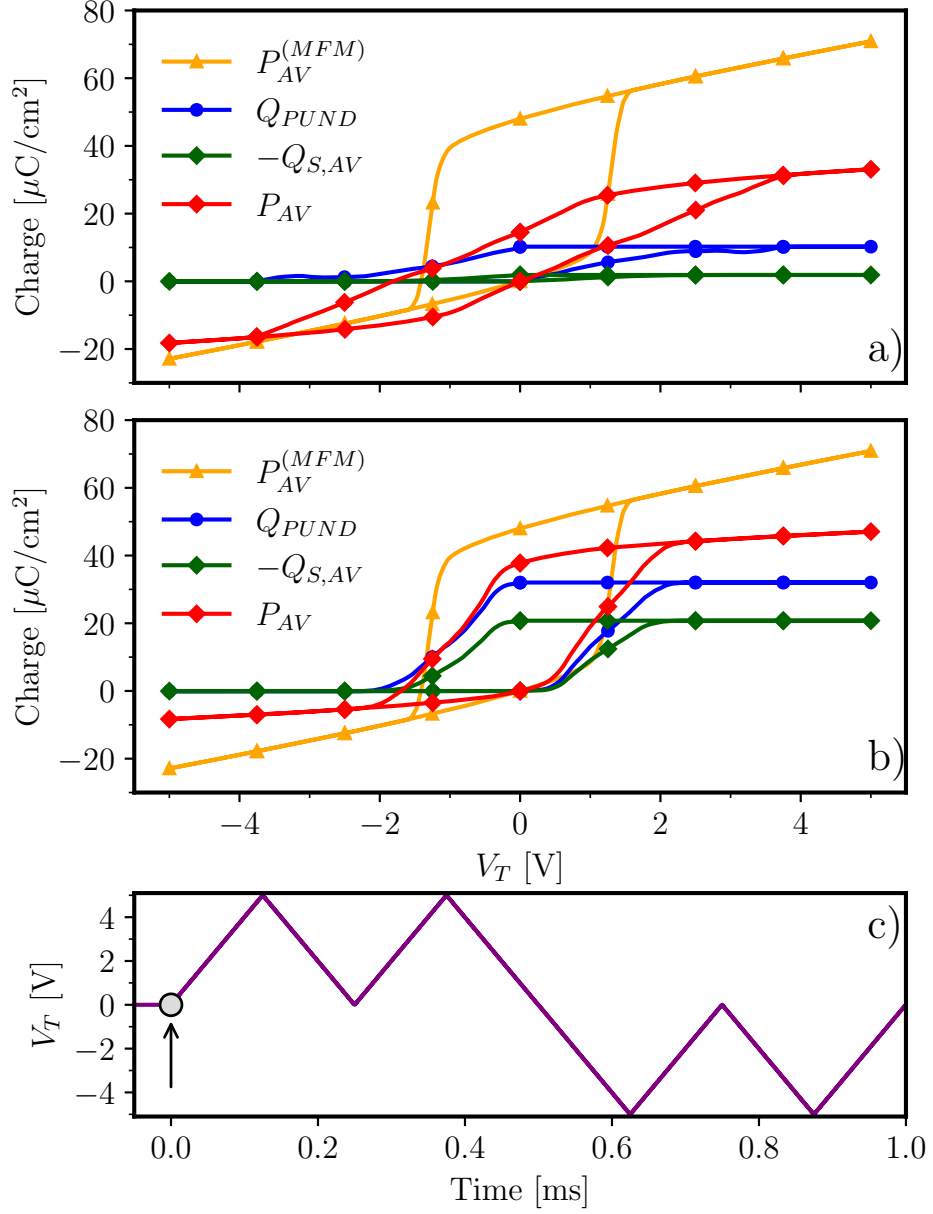
Figure 3.5: Simulated charges corresponding to a 1 kHz PUND waveform applied to an MFDM structure. The Q_{PUND} is either $Q_{PU} = (Q_P - Q_U)$ or $Q_{ND} = (Q_N - Q_D)$, respectively during the P pulse (i.e. for a positive V_T) or during the N pulse (i.e. for a negative V_T). The average polarization P_{AV} and trapped charge $-Q_{S,AV}$ during the P and N pulses are also shown. The Al_2O_3 layer thickness is $t_D = 1.5$ nm. a) Results for acceptor and donor type trap densities $N_{acc} = N_{don} = 0.5 \times 10^{13}$ [$cm^{-2}eV^{-1}$]; b) Results for $N_{acc} = N_{don} = 4 \times 10^{13}$ [$cm^{-2}eV^{-1}$]; c) voltage waveform used in simulations with the reference point in time for all the charges displayed in figure.
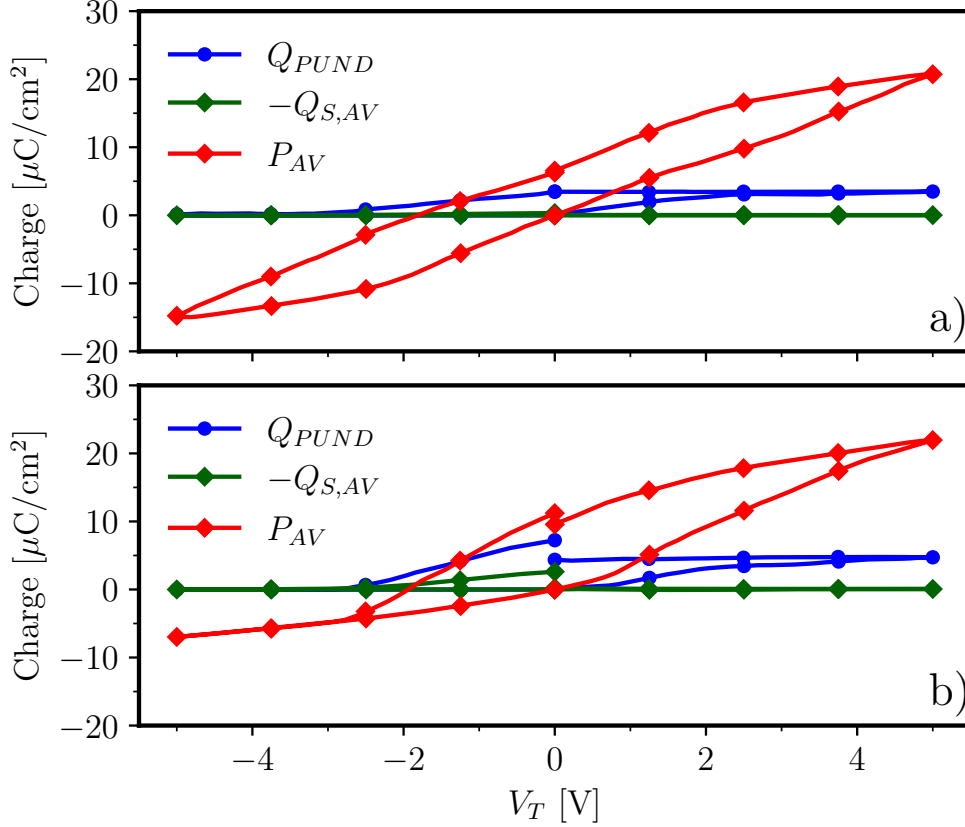
Figure 3.6: Same simulations for a PUND waveform in an MFDM structure as in Figure 3.5, but for an oxide thickness t_D of 2.5 nm. a) Results for acceptor and donor type trap densities $N_{acc} = N_{don} = 0.5 \times 10^{13}$ [cm^{-2}eV^{-1}]; b) Results for $N_{acc} = N_{don} = 4 \times 10^{13}$ [cm^{-2}eV^{-1}].

term due to the opposite sign. The results for Q_{PUND} are quite different in Figure 3.5b, because the $Q_{S,AV}$ can now compensate P_{AV} to a significant extent, thus drastically reducing the depolarization field. The hysteresis loop of the Q_{PUND} curve in Figure 3.5b is qualitatively similar to the experimental behaviour observed in FTJ structures with a thin tunnel oxide [71], [98], and the discrepancy between Q_{PUND} and P_{AV} is much smaller than in Figure 3.5a. Figure 3.6 illustrates the same analysis as in Figure 3.5, but for a larger dielectric thickness $t_D = 2.5$ nm. In this case the results of both small and large interface traps densities have a qualitative behaviour similar to Figure 3.5a, namely the Q_S is very small (green diamonds) and the compensation of the ferroelectric polarization is minimal. For both traps densities, the depolarization field results in a Q_{PUND} much smaller than P_{AV}. The different behaviour in

Figure 3.6b compared to Figure 3.5b is due to the fact that, according to the tunneling effective masses and traps cross-sections reported in Table 3.1, the trapping and de-trapping coefficients obtained for the simulation parameters reported in Table 3.1 and thus the resulting trapping dynamics cannot follow the 1 kHz V_T waveform for $t_D = 2.5$ nm or larger. In fact, because the HZO layer is 10 nm thick, in the simulations the trapping dynamics is governed by the tunnelling through the much thinner dielectric layer. The lack of Q_S modulation in Figure 3.6b is thus a dynamic effect. This highlights how the trapping-induced compensation of the ferroelectric polarization requires both a large enough trap density at the FE-DE interface, and a trapping dynamics fast enough to respond to the V_T waveform or, equivalently, a slow enough applied voltage waveform that enables the charge trapping.

This latter observation has been crucial in transient negative capacitance experiments, where thick dielectrics and fast voltage waveforms were used to avoid an undesired compensation of the ferroelectric polarization and to achieve a hysteresis-free behaviour [53], [55], [76]. While the t_D values at which traps can no longer respond to a given V_T waveform depend on the tunnelling model and the corresponding parameters in Table 3.1, the qualitative trend is expected to be independent of the tunnelling parameters.

3.3.3   Discrepancies between Q_{PUND} and P_{AV}

The discrepancies between Q_{PUND} and P_{AV} shown in Figures 3.5 and 3.6 correspond to errors in the outcome of the PUND method. Hence, in this section, the relative error $E_{PU} = |Q_{PU} - P_{AV}^{(P)}|/P_{AV}^{(P)}$ will be evaluated, assuming that all the quantities are evaluated at the end of the P or the U pulse, namely when V_T is zero. Similar definitions apply to the N and D pulses, and the simulation results are also completely similar (not shown). Figure 3.7 shows the Q_{PU} of the MFDM structures. It can be seen that a combination of a large t_D and low concentrations of traps lead to low simulated Q_{PU} values, because the corresponding $\varepsilon_0\varepsilon_F E_{DP,AV}^{(P)}$ term is comparable to $P_{AV}^{(P)}$ (as later shown in Figure 3.9). Figure 3.8 reports the evaluation of the error E_{PU} for different dielectric thicknesses and trap densities. As it can be seen, the error stemming from interpreting the Q_{PU} as the $P_{AV}^{(P)}$ tends to decrease for increasing trap densities, due to the corresponding reduction of the depolarization field E_{DP}. For the same reason the error increases for thicker dielectrics. This latter behavior results in a t_D dependence of the P_{AV} estimated by the PUND method, which is an artifact of the method when it is applied to an MFDM structure.

For $t_D = 2.5$ nm the error is fairly insensitive to the trap density, because the Q_S in the traps cannot respond to the V_T waveform according to the
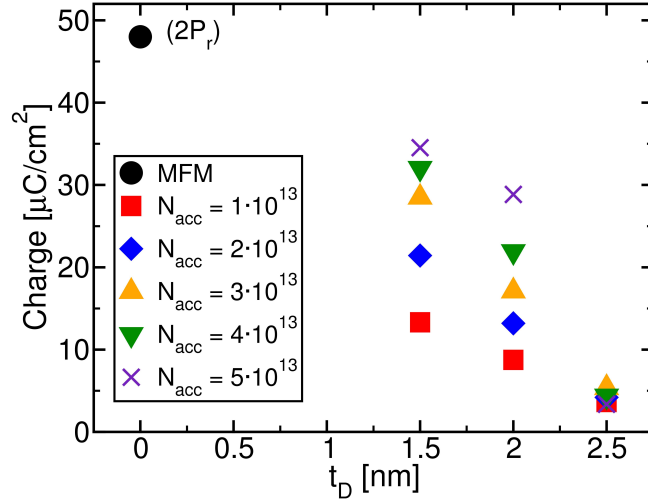
Figure 3.7: Q_{PU} extracted from PUND simulations in MFDM structures for $V_T = 0$ V, for different dielectric thickness t_D and different traps density $N_{acc}=N_{don}$ (in units of $cm^{-2}eV^{-1}$). The remanent polarization $2P_r$ extracted for an MFM structure is also reported for comparison. (©2021 IEEE)

tunnelling model used in simulations. This result highlights the necessity to use relatively slow voltage waveforms in experiments performed on devices with relatively large dielectric thickness, in order to ensure the traps' response to the applied bias. To gain an insight about the main causes of the errors shown in Figure 3.8, Equation (3.13) can be rewritten as

$$
\begin{aligned}
Q_{PU} \approx & \frac{C_D}{C_0} \left(P_{AV}^{(P)} - P_{AV}^{(U)} \right) - \frac{C_F}{C_0} \left(Q_{S,AV}^{(P)} - Q_{S,AV}^{(U)} \right) + \\
& + Q_{QS,MF}^{(P)} - Q_{QS,MF}^{(U)}
\end{aligned}
\tag{3.14}
$$

where Equation (3.10) is used to express the depolarization field $E_{DP,AV}^{(P)}$; the leakage part has been omitted because the leakage current is not included in simulations.

Figure 3.9(a) reports the quantities in the right–hand side of Equations (3.10), (3.13) and (3.14), for a dielectric thickness $t_D = 1.5$ nm and evaluated in the same condition used to evaluate the PUND error in Figure 3.8 (i.e. at $V_T = 0$ V).

Figure 3.9a conveys several important messages. The terms $Q_{QS,MF}^{(P)}$, $Q_{QS,MF}^{(U)}$ (diamonds) related to the trapping and de-trapping current at the MF electrode are negligible even for large trap densities, hence they do not appreciably influence Q_{PU} in Equations (3.13) and (3.14). This is not surprising because in the MFDM structures at study, traps exchange electrons primarily with
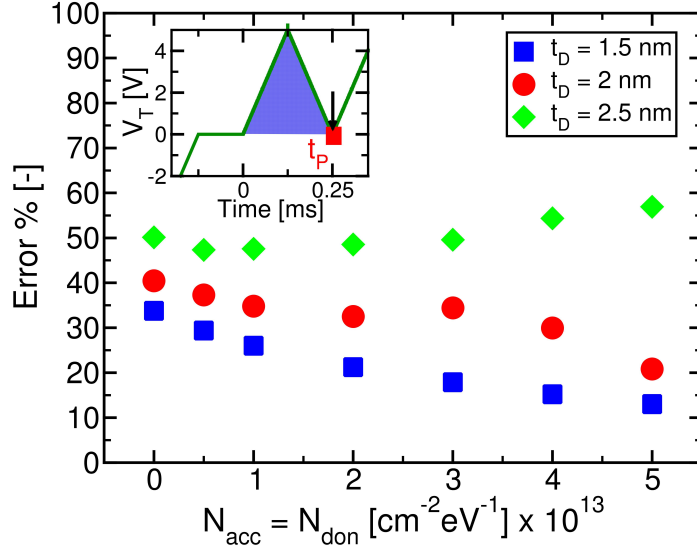
Figure 3.8: Error $|Q_{PU} - P_{AV}^{(P)}|/P_{AV}^{(P)}$ of PUND measurements in an MFDM structure for different thicknesses t_D and different trap densities $N_{acc} = N_{don}$. The error is calculated for the P and U pulses. a) Error evaluated at the end of the P pulse (see inset); b) Error evaluated at the peak of the P pulse. (©2021 IEEE)

the MD electrode due to the much thinner dielectric layer.

Moreover, at large trap densities the $Q_{S,AV}^{(P)}$ (filled circles) in the P pulse is comparable to $P_{AV}^{(P)}$ (filled squares), whereas $Q_{S,AV}^{(P)}$ becomes negligible at low trap densities. The $Q_{S,AV}^{(U)}$ in the U pulse, instead, is always negligible compared to $P_{AV}^{(P)}$. This is because, for the case at study in Figure 3.9, the band bending in the dielectric at the end of the P pulse is such that the energy levels of both acceptor and donor traps fall below the Fermi level of the MD contact (see Figure 3.4. Hence, essentially all traps have been filled at the end of the P pulse, and their occupation is not appreciably changed during the following U pulse. Figure 3.9a shows that also $P_{AV}^{(U)}$ in the U pulse is much smaller than $P_{AV}^{(P)}$. This is because the P_{AV} in the P and U pulse is a measure of the non–reversible switching, whereas most of the switching in the U pulse is reversible in nature because it is the switching of those domains that have back switched after the P pulse.

As mentioned above, Figure 3.9a shows that for low trap densities $|Q_{S,AV}^{(P)}| \ll P_{AV}^{(P)}$ and Equation (3.10) suggests that this results in

$$\varepsilon_0 \varepsilon_F E_{DP,AV}^{(P)} \simeq -(C_F/C_0) P_{AV}^{(P)}$$
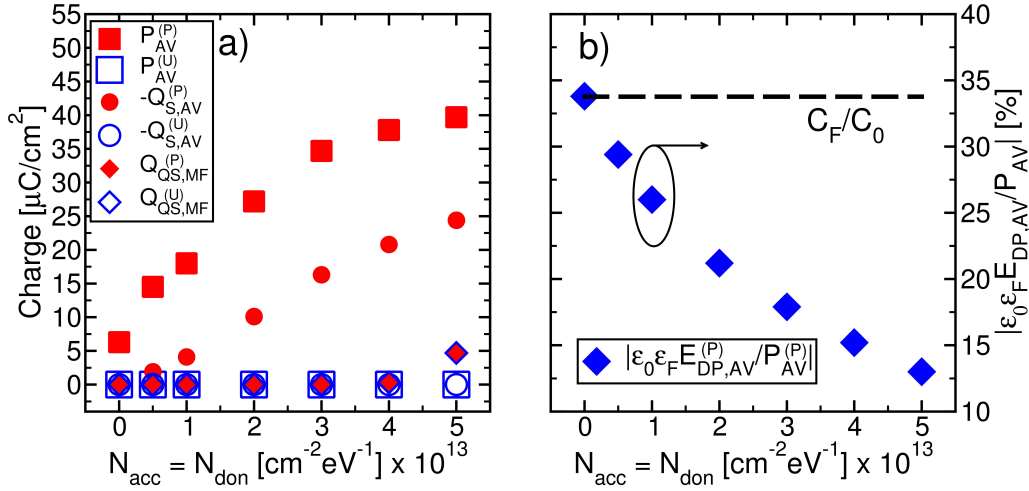
Figure 3.9: Charge components contributing to Q_{PU} according to Equation (3.14) and Equation (3.13) evaluated for t_D=1.5 nm and in the same conditions as in Figure 3.8 (i.e. at the end of the P pulse with $V_T = 0$ V). The sign of $Q_{S,AV}$ and $\varepsilon_0\varepsilon_F E_{DP,AV}^{(P)}$ is opposite to the sign of P_{AV} and the figure displays $-Q_S$ and $-\varepsilon_0\varepsilon_F E_{DP,AV}^{(P)}$. All the quantities shown in the figure are difference between the values at the end and at the start of the P pulse. (©2021 IEEE)

as it is confirmed by Figure 3.9b. These are the conditions that in Figure 3.8 correspond to the maximum discrepancy between Q_{PU} and $P_{AV}^{(P)}$, leading to the maximum error. Equation (3.14) shows that for $|Q_{S,AV}^{(P)}| \ll P_{AV}^{(P)}$ the extracted Q_{PU} tends to $(C_D/C_0)P_{AV}^{(P)}$, in fact resulting in a large underestimate of $P_{AV}^{(P)}$. At large trap densities, instead, $|Q_{S,AV}^{(P)}|$ becomes comparable to $P_{AV}^{(P)}$ and Equation (3.10) predicts a drastic reduction of the $|\varepsilon_0\varepsilon_F E_{DP,AV}^{(P)}/P_{AV}^{(P)}|$ term, which can be observed in Figure 3.9b. The error in Figure 3.8 is correspondingly reduced at large trap densities; in fact Equation (3.13) suggests that Q_{PU} tends to $P_{AV}^{(P)}$.

3.4 Small Signal Analysis

This section reports an investigation of the AC small–signal C–V curves (SSCV) in metal–ferroelectric–dielectric–metal (MFDM) FTJs (Fig. 3.10). Measurements are obtained with an experimental setup on-purposely developed in the nanoelectronic laboratory at the University of Udine to test the dependability of the assumptions behind the small signal AC analysis in ferroelectric devices.

An instructive insight is provided by comparing simulations and experiments

49

for both the large–signal P–V curves (LSPV) and the SSCV response.

3.4.1   Experimental setup and results
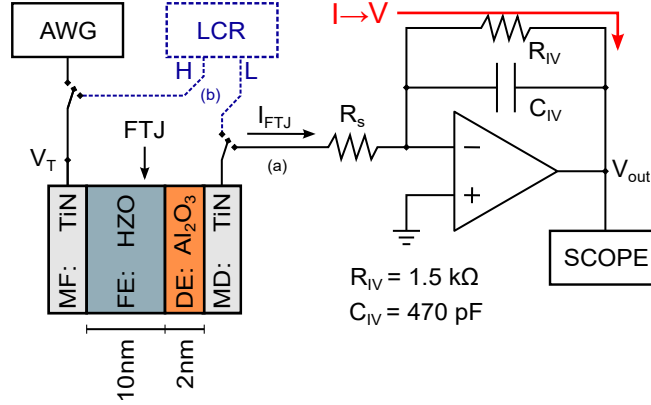
Figure 3.10: Sketch of the MFDM FTJs of this work and of the experimental setup. The setup consists of two distinct parts: (a) Virtual–grounded I→V converter (R_{IV}=1.5 kΩ, C_{IV}=470 pF) to measure the switching current I_{FTJ} through an oscilloscope. (b) An LCR meter to measure the AC small–signal capacitance. (©2022 IEEE)

The experimental measurements reported in this chapter have been carried out by Marco Massarotto, a fellow PhD student in the nanoelectronics team at the University of Udine, whom I collaborated with for the topics covered in the present chapter.

Triangular pulses with an amplitude of several Volts are typically used to measure LSPV curves, while an AC small-signal is used for SSCV measurements. From literature [99], [100], there is a consensus that the irreversible polarization switching dominates LSPV measurements giving a negligible contribution to SSCV curves. To verify this claim, we performed a direct inspection of the current response to the AC small-signal voltage in an FTJ. To this purpose, the experimental setup of Fig. 3.10 was developed, where an arbitrary waveform generator (AWG, Agilent 33250A) supplies the voltage V_T at the MF metal electrode, while the current I_{FTJ} is measured at the virtual–grounded MD metal contact through an $I \rightarrow V$ converter [101]. The OPAMP (TI TL082CP) feedback loop defines the trans–impedance of the amplifier ($V_{out} = -R_{IV}I_{FTJ}$) inside its bandwidth $BW = (2\pi R_{IV}C_{IV})^{-1}$. The V_{out} is finally monitored through an oscilloscope (Tektronix TDS520B). This custom experimental setup allows for the measurement of P–V curves using triangular pulses, as well as the AC small–signal response to a sinusoidal input. Moreover, the SSCV curves were also measured with an LCR
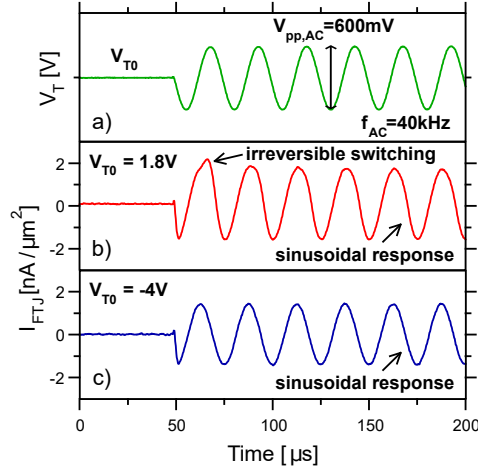
Figure 3.11: Emulation of an AC measurement by using the $I \to V$ converter of Fig. 3.10. (a) Sinusoidal V_T waveform superimposed to a DC bias V_{T0}. (b) Measured I_{FTJ} for $V_{T0} = 1.8$ V which is close to the positive coercive voltage of the FTJ (see Fig. 3.13a). A deviation of the I_{FTJ} from the sinusoidal waveform is observed during the first positive half–period, which is attributed to contribution of the irreversible polarization switching. I_{FTJ} for $V_{T0} = -4$ V showing a sinusoidal–only response. (©2022 IEEE)

meter (HP 4284A) to validate the custom experimental setup. Small–signal measurements are typically used to measure the FTJ capacitance, however, the measured small–signal capacitance does not match the effective capacitance extracted from the large–signals measurements [99], [102]. This is often attributed to the irreversible switching of the HZO, which is inherently non-linear and therefore cannot be sensed by small–signal sinusoidal pulses. While this point has not yet been completely assessed [99], [102], this behaviour raises questions on whether conventional small–signal analysis is applicable to these devices, especially in consideration of the hysteretic and potentially non–linear response of the spontaneous polarization in the FTJs.

As shown in Fig. 3.11, thanks to the AWG, the V_T waveform for different DC bias values V_{T0} (typically used in LCR based measurements) was emulated, and for each bias the current I_{FTJ} was recorded as well. The reasoning behind this test is the inspection of the I_{FTJ} waveform produced by a sinusoidal V_T waveform superimposed to an appropriate DC bias. Figure 3.11a shows that the irreversible polarization switching contribution seems to be observed only during the first positive AC semi–period, with a sizeable deviation from the sinusoidal shape. The I_{FTJ} is instead clearly sinusoidal in the following periods, despite the relatively large 300 mV amplitude of the AC signal. This is behaviour was observed for the bias $V_{T0} = 1.8$ V close to the positive coercive voltage (see Fig. 3.13a). In Fig. 3.11b, where the voltage bias $V_{T0} = -4$ V is
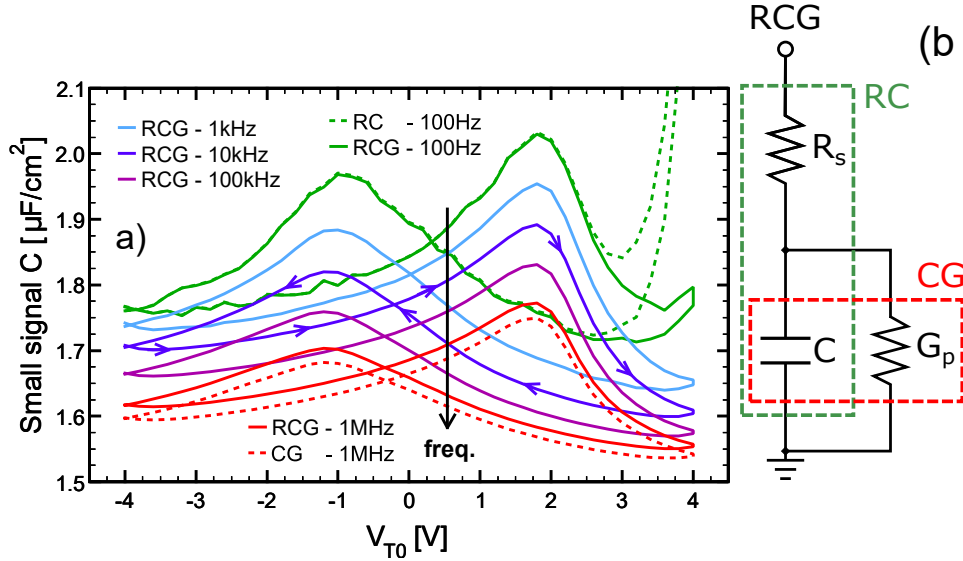
Figure 3.12: (a) SSCV curves measured with the LCR meter in the 100 Hz–1 MHz range and according to the different equivalent circuits sketched in (b), namely the RC series (green, dashed), the CG parallel (red, dashed) and the hybrid series–parallel RCG (solid line) circuit. (ⓒ2022 IEEE)

far from the coercive voltage observed in Fig. 3.13a, no deviation from the sinusoidal shape is observed.

The analysis in Fig. 3.11 excludes that a non–linear I_{FTJ} response to the AC V_T waveform can affect the SSCV curves detected by an LCR meter.

Therefore, having confirmed the dependability of the LCR meter measurements for the FTJ characterization, this analysis was used to study the FTJ SSCV characteristics.

Figure 3.12a shows the hysteretic butterfly–shaped C–V curves measured with a V_{T0} sweep from $-4\,\mathrm{V}$ to $+4\,\mathrm{V}$ at different AC frequencies f ranging from 100 Hz to 1 MHz. The reasonably bias–independent capacitance measured at $V_{T0}\approx\pm4\,\mathrm{V}$ is quite close to the estimated series capacitance $C_S=1.44\,\mathrm{\mu F\,cm^{-2}}$ due to the sole linear dielectric response of the FTJ stack (for $\varepsilon_{FE}=30$, $\varepsilon_{DE}=9$), and it shows only a limited dependence on f. Since the frequency dependence in Fig. 3.12a may be affected by the capacitance extraction method, different extraction circuits were used in the interpretation of the results (see Fig. 3.12b).

The simple parallel CG scheme (red, dashed) may be more suitable in the presence of a possible steady–state leakage (mainly affecting the current at low f) while it may be less accurate when series resistances become important, namely at high AC frequency f. On the other hand, the series RC model

(green, dashed) fails to de–embed the leakage contribution at low f, while being more reliable at high f.

In the attempt to use a single circuit, able to correctly model C in the whole f range, a hybrid series–parallel RCG circuit (Fig. 3.12b) was adopted, with the series resistance R_s extracted at each V_{T0} as the real part of the impedance at $1\,\mathrm{MHz}$, assuming a negligible contribution from leakage at $1\,\mathrm{MHz}$. The curves extracted with the hybrid RCG circuit closely match the results obtained with the simpler CG and RC schemes in their frequency range of applicability, thus confirming the reliability of the extraction circuit.

3.4.2   Small–Signal AC LGD model

This section is focused on the AC response of Ferroelectric Tunnel Junctions, therefore the LGD-based simulation framework is extended to the frequency domain by using the Small–Signal approximation. In particular, the following small–signal quantities can be introduced

$$P = P_0 + \Re\left[\widetilde{P}\exp\left(j\,\omega\,t\right)\right] \tag{3.15a}$$

$$V_T = V_{T0} + \Re\left[\widetilde{V}_T\exp\left(j\,\omega\,t\right)\right] \tag{3.15b}$$

$$f_T = f_{T0} + \Re\left[\widetilde{f}_T\exp\left(j\,\omega\,t\right)\right] \tag{3.15c}$$

where $\widetilde{P}$, $\widetilde{V}_T$ and $\widetilde{f}_T$ are the amplitudes of the AC polarization, voltage bias and trap occupation, respectively. Here $\Re[\cdot]$ denotes the real part of the complex number, and P_0, V_{T0} and f_{T0} are the polarization, voltage bias and trap occupation of the bias point around which the system is linearized. This approximation is valid if the changes of the state variables introduced by the AC input are small enough to ensure that the response of the system to perturbations is linear. The results in Section 3.4.1 experimentally confirmed the validity of such assumptions, thus corroborating the applicability of the small–signal approximation.

By recalling Equations (3.1) and (3.2), it is possible to formally re-write them as:

$$\frac{\partial P_i}{\partial t} = F_{P,i} \tag{3.16a}$$

$$\frac{\partial f_{T,i}}{\partial_t} = F_{T,i} \tag{3.16b}$$

which, by using the AC small–signal notation in Eq. (3.15) and at the angular frequency ω, become:

$$j\,\omega\widetilde{P}_i = \frac{\partial F_{P,i}}{\partial P_i}\bigg|_{\substack{P_0\\f_{T0}\\V_{T0}}}\widetilde{P}_i + \frac{\partial F_{P,i}}{\partial f_{Ti}}\bigg|_{\substack{P_0\\f_{T0}\\V_{T0}}}\widetilde{f}_{Ti} + \frac{\partial F_{P,i}}{\partial V_T}\bigg|_{\substack{P_0\\f_{T0}\\V_{T0}}}\widetilde{V}_T \qquad (3.17a)$$

$$j\,\omega\widetilde{f}_{Ti} = \frac{\partial F_{T,i}}{\partial P_i}\bigg|_{\substack{P_0\\f_{T0}\\V_{T0}}}\widetilde{P}_i + \frac{\partial F_{T,i}}{\partial f_{Ti}}\bigg|_{\substack{P_0\\f_{T0}\\V_{T0}}}\widetilde{f}_{Ti} + \frac{\partial F_{T,i}}{\partial V_T}\bigg|_{\substack{P_0\\f_{T0}\\V_{T0}}}\widetilde{V}_T \qquad (3.17b)$$

and result in the following linear system

$$j\,\omega\begin{bmatrix}\widetilde{\boldsymbol{P}}\\\widetilde{\boldsymbol{f_T}}\end{bmatrix} = \underbrace{\begin{bmatrix}\left[\dfrac{\partial F_{P,i}}{\partial\widetilde{\boldsymbol{P}}}\right] & \left[\dfrac{\partial F_{P,i}}{\partial\widetilde{\boldsymbol{f_T}}}\right]\\[3mm]\left[\dfrac{\partial F_{T,i}}{\partial\widetilde{\boldsymbol{P}}}\right] & \left[\dfrac{\partial F_{T,i}}{\partial\widetilde{\boldsymbol{f_T}}}\right]\end{bmatrix}}_{=J_F}\cdot\begin{bmatrix}\widetilde{\boldsymbol{P}}\\\widetilde{\boldsymbol{f_T}}\end{bmatrix} + \underbrace{\begin{bmatrix}\dfrac{\partial F_{P,i}}{\partial\widetilde{V}_T}\\[3mm]\dfrac{\partial F_{T,i}}{\partial\widetilde{V}_T}\end{bmatrix}}_{=J_V}\cdot\widetilde{V}_T \qquad (3.18)$$

where J_F is the Jacobian matrix obtained for the AC small–signal polarizations and trap occupations, while J_V is the column vector obtained for the small–signal voltage waveform. J_F has rank N_{PT} which is the total number of unknowns and equal to $n_D\cdot(1 + N_{E,acc} + N_{E,don})$, where n_D is the number of simulated domains, and $N_{E,acc}$ and $N_{E,don}$ are the number of energy discretizations for acceptor and donor traps, respectively. Equation (3.18) can be further rearranged to obtain the quantities of interest in the calculation of the small–signal admittance (and thus small–signal capacitance) in the following form:

$$\underbrace{\left[j\,\omega\,\boldsymbol{I} - \boldsymbol{J_F}\right]}_{=J_{TOT}}\widetilde{\boldsymbol{X}} = J_V \qquad (3.19)$$

with $\boldsymbol{I}$ being the identity matrix, and $\widetilde{\boldsymbol{X}} = \left[\widetilde{\boldsymbol{P}}\ \widetilde{\boldsymbol{f_T}}\right]/\widetilde{V}_T$. The size of the problem grows rapidly by increasing n_D, $N_{E,acc}$ and $N_{E,don}$, which makes AC simulations computationally demanding. Moreover, to obtain a better conditioning of the matrix J_{TOT}, which is critical for the accuracy of the numerical solution of the linearized system, all the entries of the matrix J_F are converted to a frequency in order to ensure that all the matrix elements of J_{TOT} have the same physical units.

The linear system can be solved for the unknowns $\widetilde{\boldsymbol{X}}$, and the quantities of

interest can then be written as

$$\frac{\widetilde{P}_{AV}}{\widetilde{V}_T} = \frac{1}{n_D} \sum_{i=1}^{n_D} \widetilde{X}_i \tag{3.20a}$$

$$\frac{\widetilde{Q}_{S,AV}}{\widetilde{V}_T} = -\frac{1}{n_D} \left(\sum_{i=n_D+1}^{N_{PT,acc}} \widetilde{X}_i + \sum_{N_{PT,acc}+1}^{N_{PT}} \widetilde{X}_i \right) \tag{3.20b}$$

where $N_{PT,acc}$ is defined as $n_D \cdot N_{E,acc}$.
With the linearized version of Equation (3.11) (ignoring the contributions of possible leakage or charge injection from the contact MF) and with Eq. (3.20), it is possible to write the small–signal admittance as

$$Y = \frac{\widetilde{I}_{MF}}{\widetilde{V}_T} = j\,\omega\,C_S + j\,\omega\,\left(\frac{C_D}{C_0} \frac{\widetilde{P}_{AV}}{\widetilde{V}_T} - \frac{C_F}{C_0} \frac{\widetilde{Q}_{S,AV}}{\widetilde{V}_T} \right) \tag{3.21}$$

whose imaginary part provides the small–signal capacitance, that is the main focus of the AC analysis.

3.4.3 Simulation Results and Discussion
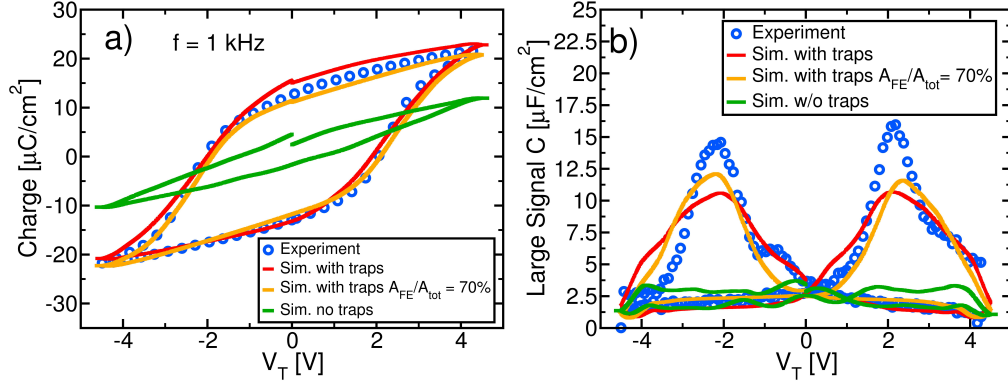
Figure 3.13: Comparison of measured (symbols) and simulated (lines) LSPV curves (a), and LSCV curves (b), for an Al_2O_3 thickness $t_{DE} = 2\,nm$. Simulations are shown for no trapped charge (green line), and for a density of acceptor and donor type traps equal to respectively $N_{acc}=4.7 \cdot 10^{13}\,cm^{-2}\,eV^{-1}$ and $N_{acc}=5.4 \cdot 10^{13}\,cm^{-2}\,eV^{-1}$ and over a $2.5\,eV$ energy range. Simulations for a 70% ferroelectric area in the HZO film (i.e. A_{FE}/A_{tot}=70%) are also reported for $N_{acc} = 5.9 \cdot 10^{13}\,cm^{-2}\,eV^{-1}$ and $N_{don} = 9.6 \cdot 10^{13}\,cm^{-2}\,eV^{-1}$. The bias-independent trapping emission rate $c_{MD0} = 2 \cdot 10^4\,s^{-1}$ was used in all simulation (see Eq. (3.2) in Section 3.2). (©2022 IEEE)

Simulation of SSCV curves in ferroelectric materials and devices has been investigated to a lesser extent in the literature compared to its LSPV counterpart. In particular, it is unclear if both LSPV and SSCV curves can be reproduced equally well in simulations using the same model and material parameters. There is a consensus that LSPV measurements probe the irreversible polarization switching, while SSCV measurements mainly probe the reversible response of the device, typically interpreted as a domain wall motion (DWM) [100]. While semi-empirical models to describe the DWM have been successfully used [100], it has been argued that the DWM effects are also adequately represented in the LGD equations [40], [103], thus even in their small–signal linearization, provided that a non–negligible domain wall coupling is considered. However, recent first principle calculations suggest that in HfO_2 the domain wall coupling should be negligible [93]. This aspect highlights the interest for an analysis of both LSPV and SSCV curves using the very same LGD model discussed in Section 3.2. Figure 3.13a reports the experimental $P-V$ curves corresponding to triangular pulses at a frequency $f = 1\,kHz$ used to calibrate the simulation model, and Fig. 3.13b shows also an effective large-signal capacitance curve (LSCV), that was extracted by dividing the current during the triangular pulse by the slope of the voltage
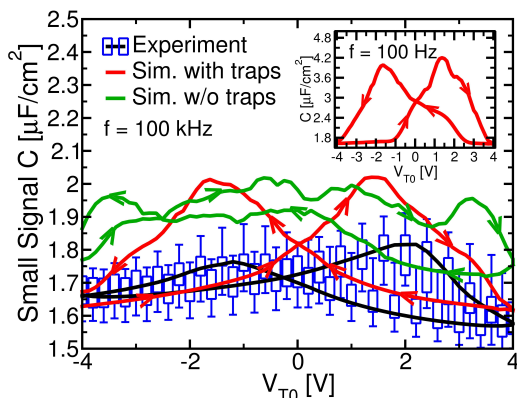
Figure 3.14: Measured (box plot, blue) and simulated (lines) small–signal capacitance curves at an AC frequency f=100 kHz and for the same device as in Fig. 3.13a. Measurements correspond to ten nominally identical devices. Simulations with and without trapping are displayed. The inset shows simulations at f=100 Hz. (©2022 IEEE)

ramp, namely as LSCV=$I_{FTJ}/(dV_T/dt)$. Figure 3.13b confirms that the measured LSCV curves are much larger than the SSCV counterparts (see Fig. 3.12a), due to the irreversible switching component. Figures 3.13a and 3.13b also report the corresponding simulated LSPV and LSCV curves. In simulations, the mean values of anisotropy constants α, β and γ are equal to $-3.8 \cdot 10^8$ m/F, $-3.2 \cdot 10^{10}$ m^5/(FC^2) and $7.9 \cdot 10^{11}$ m^9/(FC^4), respectively. A domain–to–domain random Gaussian distribution of α, β, γ was introduced in order to obtain standard deviation on the domain-wise coercive field σ_{Ec}=30% (normalized to mean value), which is higher than the one used in Section 3.3. Simulations assume a fully ferroelectric HZO film (i.e. 100% orthorhombic phase), unless otherwise stated. The switching resistivity was set to ρ=110 Ω m [94], which yields a ferroelectric characteristic time $t_\rho \sim$ 144 ns. Both values are in agreement with previously reported ones for HZO ferroelectrics, while the domain wall coupling k was set to zero, if not otherwise stated, by following recent first principle calculations for HfO$_2$ [93]. Since t_ρ sets the time–scale of the ferroelectric dynamics, it also sets the maximum AC frequency at which a ferroelectric small–signal response can be observed, with $f_\rho \simeq 1/t_\rho$. Trap parameters and trapping rates can be found in the caption of Fig. 3.13. For the simulations reported in this section, the simpler trapping model discussed in Section 3.2 was used and it was also assumed that trapping and de-trapping only occurs with the MD contact, essentially setting $c_{nMF0} = 0$. Figure 3.13a shows that simulations neglecting any trapping at the FE-DE interface result in much narrower and more tilted curves compared to experiments. This behavior has been already emphasized in Section 3.3, including the links to the previous literature. To reconcile
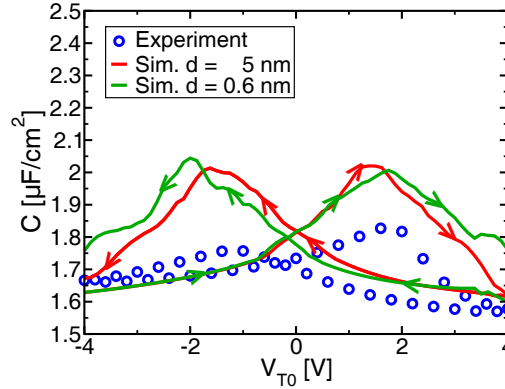
Figure 3.15: Capacitance simulations as in Fig. 3.14 but for different values of the domain size d with all other simulation parameters being the same. The AC frequency is f=100 kHz. Same measurements as in Fig. 3.14 are also shown (box plot, blue).

simulations with experiments, a substantial density of traps at the FE-DE interface has been assumed and consistent with values extracted in [102], [104]. As expected, this trend is also observed in LSCV curves, where simulations neglecting trapping show a large discrepancy with experiments, while the agreement improves remarkably with the inclusion of traps.

The simulations without traps do not exhibit the capacitance peaks at the coercive V_T voltages observed in experiments, following the same qualitative trend observed in LSPV experiments with lower trap densities. Simulations with traps reproduce quite well the capacitance at large $|V_T|$ values and the coercive voltages, but they overestimate the measured peak capacitance. At lower frequencies the discrepancy with experiments increases (see inset of Fig. 3.14), because the simulated small–signal capacitance grows significantly due to AC response of traps (which is negligible at $f = 100$ kHz due to the choice of c_{nMD0}, see caption of Fig. 3.13), whereas in experiments this increase is much less pronounced (see also Fig. 3.12a). One possible explanation of this mismatch could be attributed to traps being located not only at the interface between the two materials but also in the ferroelectric bulk, thus possessing multiple different and longer time constants with respect to the one used in simulations. Figure 3.15 reports simulations for different ferroelectric domain sizes d used in the LGD model and, as it can be seen, the simulated capacitance is not significantly affected by a reduction of d down to a value $d = 0.6$ nm comparable to the HZO unit cell. It is interesting to notice that when the size d is reduced, the model approaches a continuous formulation [53], and this will be further discussed in Chapter 5. Figure 3.16a illustrates the effect of a non-negligible domain wall coupling k, which is expected to augment the capacitance contribution by the inclusion of domain
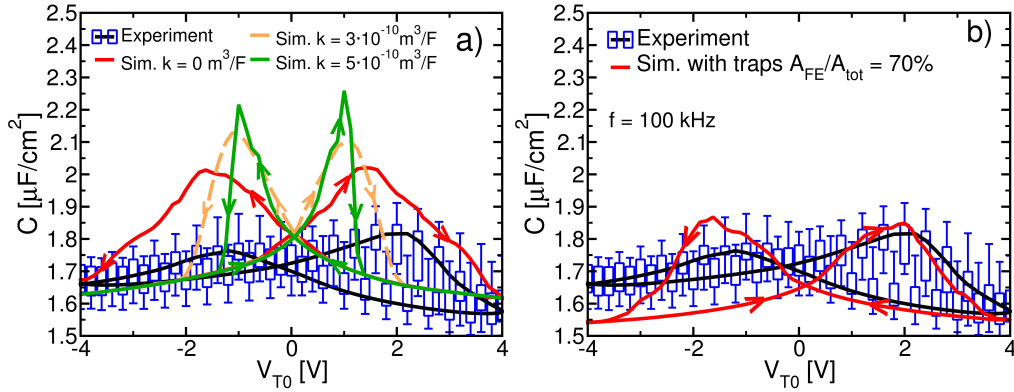
Figure 3.16: Measured and simulated capacitance as in Fig. 3.14 but for: (a) different values of the domain wall coupling k; (b) 70% fraction of ferroelectric over total area. The AC frequency is f=100 kHz. For higher k values the behaviour of the curves is closer to a single domain ferroelectric.

wall motion. Aside from being in contrast with first principle calculations [93], larger k values exacerbate the discrepancy with experiments in the peak capacitance region. Furthermore, an increase of k also degrades the agreement with the experimental P–V curves. Recalling that in HZO films the fraction of orthorhombic ferroelectric phase can reasonably vary between 50% to 70% [105], in Figs. 3.13a and 3.13b it is revealed that simulations with 70% ferroelectric area (i.e. $A_{FE}/A_{tot} = 70\%$) can still reproduce well the experimental LSPV and LSCV curves by adjusting the trap densities (see caption of Fig. 3.13).

 Moreover Fig. 3.16b shows that, by accounting for a non–ferroelectric area in the HZO film, the simulated peak capacitance in SSCV curves is reduced (for fixed values of the LGD anisotropy constants), thus improving the agreement with experiments, particularly for the positive V_T values.

59

3.5 Chapter conclusions

The theory and application of the PUND measurement technique in MFDM structures has been revisited by employing analytical derivations and numerical simulations. The interplay between the depolarization field and charge trapping in an MFDM stack makes it difficult to obtain from the terminal currents alone an accurate estimate of the spontaneous polarization switched in the P or in the N pulse.

The discrepancies between Q_{PU} and $P_{AV}^{(P)}$ were systematically analyzed for various dielectric layer thicknesses t_D and trap densities at the FE-DE interface, thus exploring a wide range of different configuration for the compensation of the ferroelectric polarization and the resulting depolarization field. Simulations allow the inspection of all the physical quantities at play, especially those not usually observable in experiments, therefore the present analysis provided an insight on the main sources of inaccuracy for the PUND measurement applied to MFDM structures.

Aside from the discrepancies between Q_{PU} and $P_{AV}^{(P)}$ that can be identified as an error of the PUND technique, it should be understood that neither the Q_{PU} nor the $P_{AV}^{(P)}$ of an MFDM structure represent a good estimate of the $2P_r$ of the underlying ferroelectric. The depolarization field can be large at zero external bias, therefore the MFDM structure at $V_T = 0$ V is not a good representation of the ferroelectric material at zero ferroelectric field. More precisely the Q_{PU} of the PUND technique underestimates the non-reversible switched polarization $P_{AV}^{(P)}$ during the P pulse, which in turn underestimates the $2P_r$ of the ferroelectric. The differences between these quantities depend on t_D and on the density of traps, which may lead to artifacts possibly hindering the characterization of the t_D dependence of the MFDM ferroelectric properties. Of course, it would be extremely useful to suggest corrections to the PUND technique or to propose a novel technique designed for MFDM structures that can account for the depolarization field, and maybe even separates the switched polarization from the trapped charge. Presently, however, there is no straightforward way of achieving such targets in an MFDM structure, and by relying exclusively on quantities accessible in experiments. In this respect, the only possible conclusion prompts the necessity of more work to improve the electrical probing of spontaneous polarization in ferroelectric-dielectric hetero-structures.

Along with an extensive analysis on large–signal behaviour of FTJs, the experimental characterization and numerical modelling of their small-signal behaviour was carried out. In particular, small–signal simulations were performed with the linearization of the same model used to simulate large–signal quantities, allowing to establish a direct link between large and small–signal

simulated results. The AC response of spontaneous polarization is not necessarily due to domain wall motion as previously reported in literature, in fact the domain wall coupling k was set to zero in simulations and its increase seems to impair the agreement with experiments. By duly accounting for a fraction of non-ferroelectric domains in the HZO film, the agreement with experiments of simulated SSCV curves is improved.

Chapter 4

Modeling of $P-V$ urves and Negative Capacitance Experiments for Antiferroelectric ZrO$_2$

4.1 Introduction to Antiferroelectricity

Antiferroelectricity is a material property that was observed in perovskites materials [106] and more recently also in hafnium-zirconium-based oxides, in particular ZrO$_2$, which exhibit also ferroelectricity and are of great interest due to their scalability and CMOS process compatibility. Antiferroelectric materials are already employed in a wide range of applications such as energy storage capacitors, electrical actuators and non-volatile memories [107]. Antiferroelectric materials display a double hysteresis in their polarization versus electric field characteristic (see Fig. 4.1) and, contrary to their ferroelectric counterpart, possess no memory state. It has been demonstrated, however, that by introducing a built-in electric field in the device the hysteresis can be shifted and thus obtaining a non-volatile memory [108]. In fact, antiferroelectric materials promise a few advantages over ferroelectric materials for memory applications. For example, ferroelectric hafnium oxides have a high coercive field that tends to reduce the cycling endurance [108]–[111]. Antiferroelectric materials, instead, have shown better endurance properties [112], that have been attributed to a smaller electrical stress due to the fact that one of the two memory states is non-polar [108], to a lower charge injection [113], as well as to different switching mechanisms [113], [114].

In most perovskites, such as PbZrO$_3$, antiferroelectricity has been ascribed

4. Modeling of $P-V$ urves and Negative Capacitance Experiments for Antiferroelectric ZrO_2
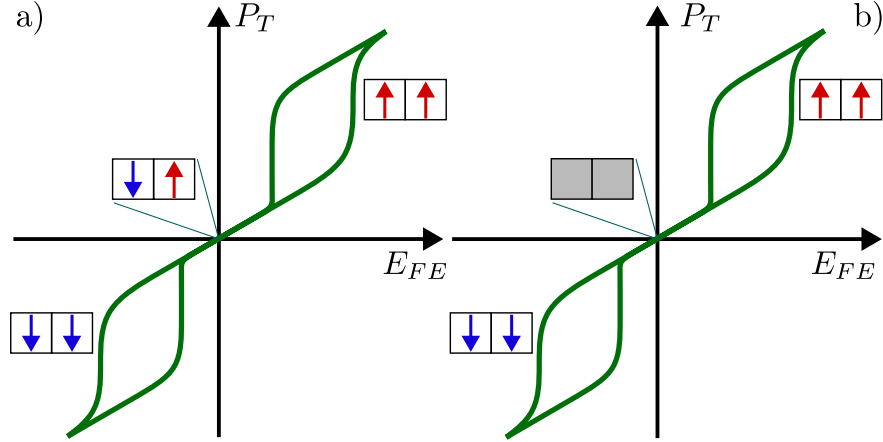
Figure 4.1: Total polarization versus applied electric field characteristic of antiferroelectric materials. a) In perovskites, the macroscopic zero polarization for zero applied electric field is the result of two sub-lattices having anti-parallel polarizations (blue and red arrows) leading to a net zero polarization. The sub-lattices can be aligned with the applied field, displaying the characteristic double hysteresis of antiferroelectric materials. Kittel's model is used to describe this physical picture. b) In zirconium oxides (i.e. ZrO_2) the zero polarization at zero applied electric field is due to the microscopic non-polar nature of the material, which undergoes a phase transition (from tetragonal to orthorhombic [115]) with the application of a large enough electric field, thus displaying polar properties and the characteristic double hysteresis. In this case Kittel's model may not be the most accurate choice for the description of the material [116].

to a macroscopically non-polar ground state stemming from the anti-polar alignment of polar domains [117], [118], which can be re-aligned by the application of an electric field, as depicted in Fig. 4.1a. This is the physical picture behind the phenomenological Kittel's model of antiferroelectricity [106], where two sub-lattices that constitute the unit cell are described with anti-parallel polarization and concur to define the free energy of the antiferroelectric material. A more pragmatic compact model for antiferroelectric capacitors can be also based on the nucleation limited switching approach [119], or on the Preisach's model [120].

In hafnium and zirconium-based materials [121], however, the microscopic picture behind antiferroelectricity (especially for ZrO_2) is fundamentally different compared to $PbZrO_3$ and similar perovskites. In fact, *ab-initio* calculations have revealed that the energy ground state of thin ZrO_2 films is tetragonal [115], which has been also confirmed by GIXRD measurements [108], [116], [121], so that at zero applied field the material is microscopically non-polar [115], [122]. By applying an electric field to the ZrO_2, a phase transition is induced from the non-polar tetragonal phase to a polar orthorhombic phase,

which is the phase also responsible for ferroelectricity in Hafnium-Zirconium Oxides (HZOs). This behaviour is qualitatively illustrated in Fig. 4.1b.

While Kittel's model gives an adequate description for antiferroelectric materials having an anti-polar alignment of the domains, it may not be the most appropriate choice to describe the physical picture governing the antiferroelectricity in ZrO$_2$, which, as stated before, is quite different from the one observed in perovskites. Therefore, in this chapter the LGD model is used to describe antiferroelectricity in ZrO$_2$ and an analytical procedure to extract the material parameters of the antiferroelectric ZrO$_2$ is proposed. Such procedure is developed within the framework of the multi–domain Landau, Ginzburg, Devonshire (LGD) model described in Section 3.2, whose applicability to antiferroelectric materials with microscopically non-polar ground state will be discussed in this chapter.

One advantage deriving from the employment of an LGD-based model to describe antiferroelectric properties of ZrO$_2$ is its ability to describe Negative Capacitance (NC) behaviour of ferroelectric materials [40], [76]. Negative Capacitance refers to the negative slope in the theoretical spontaneous polarization P versus applied electric field E_F characteristic of ferroelectric materials that stems from the Landau polynomial used to describe the total energy of the system and leads to a negative value of the differential capacitance defined as $\partial P_T/\partial E_F$ (see Fig. 4.2). NC operation is unstable Metal-Ferroelectric-Metal (MFM) stacks, and therefore cannot be observed in MFM structures. To this purpose, different device architectures have been proposed to display NC behaviour, such as stacks with one or two dielectrics to prevent charge injection and the stabilization of the ferroelectric spontaneous polarization [52], [55].

With the LGD parametrization proposed in this chapter, it is possible to obtain a negative slope also in the P-E_F characteristic of antiferroelectric materials, and the model can reproduce fairly well both quasi-static and transient NC behaviour reported in [116]. Moreover, there are interesting links between the NC operation in antiferroelectric stacks and the behaviour of a ferroelectric layer sandwiched between two dielectrics experimentally reported in [52].

4.2   Extraction of anisotropy coefficients for antiferroelectric ZrO$_2$

In this context, let us recall the expression of the Gibbs' free energy for a capacitor with metal electrodes and a ferroelectric (FE) or anti-ferroelectric

## 4. Modeling of $P - V$ urves and Negative Capacitance Experiments for Antiferroelectric ZrO_2
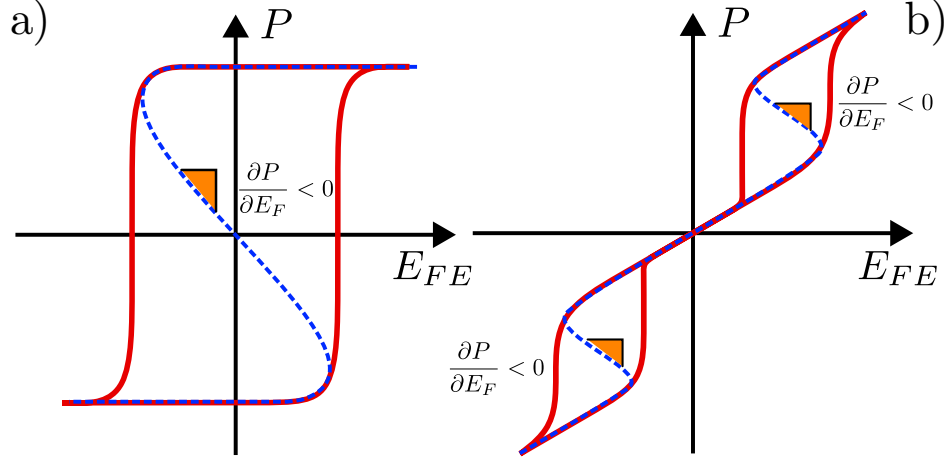
Figure 4.2: Spontaneous polarization versus Electric Field characteristic sketch for ferroelectric and antiferroelectric materials. a) Ferroelectric materials hysteresis is described by an LGD polynomial having the characteristic S-shape. b) Antiferroelectric materials hysteresis is described instead by an LGD polynomial possessing a double S-shape. In a) the point $P = E_F = 0$ is not stable.

(AFE) dielectric already introduced in Chapter 2. For a simple homogeneous polarization picture, the Gibbs' free energy of the system consisting of the capacitor and the external battery can be written as [53]

$$G = \alpha P^2 + \beta P^4 + \gamma P^6 - E_{FE} P - \frac{\varepsilon_0 \varepsilon_F E_{FE}^2}{2} \qquad (4.1)$$

where ε_0 is the vacuum permittivity, P, ε_F, E_{FE} are the spontaneous polarization, background permittivity and electric field of the FE or AFE material, while α, β and γ are the anisotropy coefficients. The quasi-static P-E_{FE} trajectories are identified by the conditions $(dG/dP)=0$ and $(d^2G/dP^2)>0$, [123], namely

$$2\alpha P + 4\beta P^3 + 6\gamma P^5 = E_{FE} \qquad (4.2a)$$

$$\frac{\partial E_{FE}}{\partial P} = 2\alpha + 12\beta P^2 + 30\gamma P^4 \geq 0 \qquad (4.2b)$$

Quasi-static experiments in a metal-FE-metal or metal-AFE-metal stack probe the overall charge in the system, usually denoted as total polarization $P_T \approx Q = P + \varepsilon_0 \varepsilon_F E_{FE}$.

Figure 4.3a shows an example of the free energy landscape for a metal-AFE-metal (M-AFE-M) system, and Eq. (4.2) prescribes that α be positive in order to have a microscopically non-polar stable state at $E_{FE} \approx 0$ and $P \approx 0$. Figure 4.3b displays the experimental P_T versus E_{FE} curve recently
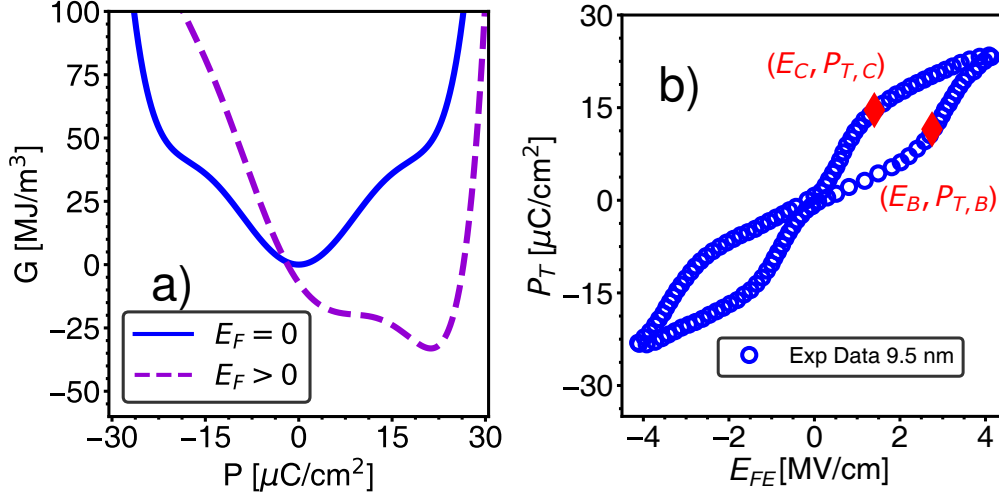
Figure 4.3: a) Gibbs' free energy landscapes calculated from Eq. (4.1) with the anisotropy coefficients in Table 4.1, and for either a zero or a positive applied field E_{FE}. At zero field (blue curve) the point $E_{FE} = P = 0$ is a free energy minimum and thus it is a stable steady-state point for the system. The application of a positive E_{FE} (purple curve) shifts the energy minimum to a positive P. b) Measured total polarization versus applied electric field in a TiN/ZrO$_2$(9.5 nm)/TiN stack [124]. The meaning of points B and C is discussed in the following sections. (©2023 IEEE)

reported for a ZrO$_2$ capacitor [124]. In Fig. 4.3b, E_B, E_C denote the coercive fields corresponding respectively to the non-polar to positive and positive to non-polar transition in the $P_T - E_{FE}$ curve. In practice, the points $(E_B, P_{T,B})$ and $(E_C, P_{T,C})$ can be identified as the points where the P_T versus E_{FE} curve exhibits a clear change in the slope. In order to define an analytical procedure for the extraction of material parameters in antiferroelectric ZrO$_2$, points B and C are assumed to correspond respectively to a maximum and a minimum of the static $E_{FE} - P_T$ relation implied by the LGD polynomial. In Appendix C, the extrema of the $E_{FE} - P_T$ relation are shown to coincide also with those of the $E_{FE} - P$ relation, which in turn are readily identified by the condition $(\partial E_{FE}/\partial P) = 0$ in Eq. (4.2b). Hence, the conditions ensuring that the quasi-static P_T-E_{FE} trajectories include points B and C become

$$2\alpha \quad + 12\beta\, P_C^2 + 30\gamma\, P_C^4 = 0 \tag{4.3a}$$

$$2\alpha\, P_C + 4\beta\, P_C^3 \quad + 6\gamma\, P_C^5 \quad = E_C \tag{4.3b}$$

$$2\alpha \quad + 12\beta\, P_B^2 + 30\gamma\, P_B^4 = 0 \tag{4.3c}$$

$$2\alpha\, P_B + 4\beta\, P_B^3 \quad + 6\gamma\, P_B^5 \quad = E_B \tag{4.3d}$$

4. Modeling of $P-V$urves and Negative Capacitance Experiments for Antiferroelectric ZrO_2

From Eqs. (4.3a) to (4.3c) α, β, γ can be readily expressed as

$$\alpha = \frac{3}{4}\frac{E_C}{P_C} + \frac{3}{4}\frac{E_C P_C}{5P_B^2 - P_C^2} \tag{4.4a}$$

$$\beta = -\frac{E_C}{8P_C^3} - \frac{3}{4}\frac{E_C}{P_C\left(5P_B^2 - P_C^2\right)} \tag{4.4b}$$

$$\gamma = \frac{E_C}{4P_C^3\left(5P_B^2 - P_C^2\right)} \tag{4.4c}$$

Eq. (4.4) provides the anisotropy coefficients in terms of E_C, P_C, P_B. However, the spontaneous polarizations P_C, P_B cannot be directly identified in the experimental curves of Figure 4.3b, but they must be calculated by using the relation $P = P_T - \varepsilon_F \varepsilon_0 E_{FE}$. This implies that the α, β, γ in Eq. (4.4) are given in terms of E_C, $P_{T,C}$, $P_{T,B}$ and of the remaining parameter ε_F. In this latter respect, it has been theoretically argued that ε_F should be considered an adjustable parameter rather than a true material constant [125], and in practice it is difficult to extract ε_F independently of α, β, γ. Therefore, by substituting α, β, γ from Eq. (4.4) into Eq. (4.3d), it can be rearranged as

$$\frac{P_C^3(5P_B^2 - P_C^2)}{P_B^3(5P_C^2 - P_B^2)} = \frac{E_C}{E_B} \tag{4.5}$$

By recalling $P_C = P_{T,C} - \varepsilon_0\varepsilon_F E_C$ and $P_B = P_{T,B} - \varepsilon_0\varepsilon_F E_B$, Eq. (4.5) can now be solved for ε_F. Namely ε_F can be used as the fourth adjustable parameter determined by Eq. (4.3), so as to ensure that the quasi-static P_T-E_{FE} trajectories include the points B and C in Fig. 4.3b.

As it can be seen, Eq. (4.5) implies also $(5P_B^2 - P_C^2) > 0$ (because $5P_C^2$ is by definition larger than P_B^2), which in turn results in positive α, γ values and in a negative β value (see Eq. (4.4)). As already mentioned, the positive α value is consistent with the microscopically non-polar nature of thin ZrO_2 films at a zero applied field and it is also consistent with previous literature for antiferroelectric ZrO_2 [126], [127]. Moreover, a positive α value is the only possible choice in order to obtain no remanent polarization at zero applied field.

In summary, the procedure to extract the anisotropy coefficients from experiments requires to firstly identify the points B and C in the measured P_T-E_{FE} curves (see Fig. 4.3b). Then Eq. (4.5) can be solved numerically to determine ε_F and, once ε_F is known, Eq. (4.4) provides expressions for α, β, γ.

4.3 Framework for numerical modelling

4.3.1 Single dielectric layer stacks
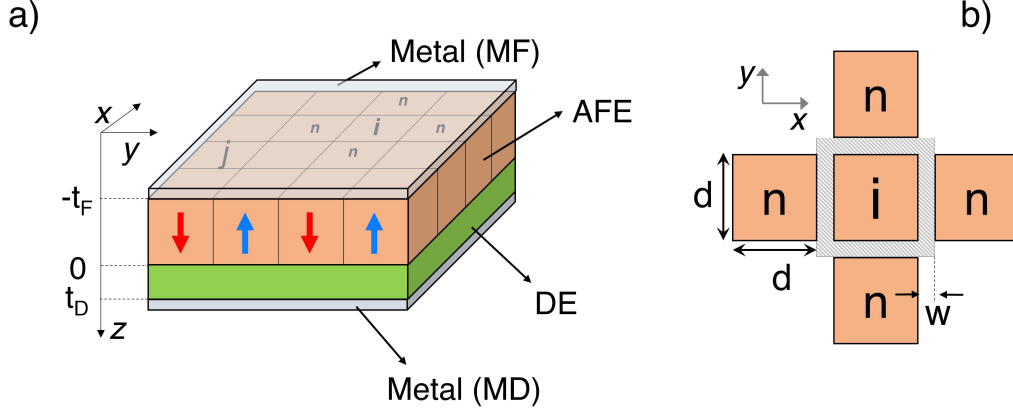
Figure 4.4: Sketch of a device structure corresponding to a metal-AFE-dielectric-metal stack. a) sketch showing thickness t_F of the AFE layer, the thickness t_D of the dielectric (DE), and the partition of the AFE layer in n_D domains. b) focus on the nearest neighbour domains included in the sum over n in Eq. (4.6), and describing the domain wall energy contribution. d and w denote respectively the domain size and the width of the domain wall region [53].

In Section 4.4 several comparisons between simulations and experiments are reported and aim to validate the extraction procedure for the anisotropy coefficients of ZrO_2. All simulations were carried out by using the solver for the multi-domain LGD equations that has been already discussed in [53], [76], [128], as well as in Section 3.2. In this section, only a few aspects of the simulation framework will be recalled because they are relevant for the cases at study in this chapter. For an AFE or a ferroelectric material consisting of n_D domains as shown in Fig. 4.4, the dynamics of the polarization P_i in each domain is described by Eq. (3.1), where the term $Q_{S,j}$ is not present because in this analysis charge trapping was not considered.

$$
t_F \, \rho \frac{\partial P_i}{\partial t} = - \left(2\alpha_i \, P_i + 4\beta_i \, P_i^3 + 6\gamma_i \, P_i^5 \right) t_F +
$$
$$
- t_F \frac{k}{w} \frac{d}{(d+w)^2} \sum_n \left(P_i - P_n \right) - \sum_{j=1}^{n_D} \left(P_j + Q_{S,j} \right) / C_{i,j}^{(dep)} + \frac{C_D}{C_0} V_T
$$
$$
(4.6)
$$

with $1/C_{i,j}^{(dep)} = 1/2(1/C_{j,i} + 1/C_{i,j})$ and the terms $C_{i,j}$ are the capacitive couplings between domains, while the other parameters have already been

69

4. Modeling of $P - V$ urves and Negative Capacitance Experiments for Antiferroelectric ZrO$_2$

described in Section 3.2. Given the similarity between the crystal chemistry of ZrO$_2$ and HfO$_2$ [37], in simulations k was set to ≈ 0, as suggested by recent first principle calculations for HfO$_2$[129], similarly to simulations performed in Sections 3.3 and 3.4. For each domain, the α_i, β_i, γ_i values were calculated by using a Gaussian distribution of the coercive fields with the mean E_C, E_B values used to extract the parameters in Table 4.1, and with a ratio $\sigma_{EC} = \sigma_{EB}$ between the standard deviation and mean value; ε_F is the same in all domains. It is relevant to mention that, aside from charge trapping, the dynamic equation is the same as the one used in the description of ferroelectricity and the introduction of the antiferroelectricity is only due to the values (and signs) of the anisotropy coefficients α_i, β_i and γ_i as discussed in Section 4.1. All simulations were performed using $n_D = 400$ domains with a domain area of 25 nm^2. The number of domains n_D mainly influences the number of terms $1/C_{i,j}^{(dep)}$ which, as stated before, describe the capacitive coupling between the $i-$th and $j-$th domain. However, such a capacitive coupling decreases quite steeply with the distance between domains, so that simulations become insensitive to n_D for large enough n_D values. Moreover, for a M-AFE-M stack (without the DE layer in Fig. 4.4) the terms $1/C_{i,j}^{(dep)}$ tend to zero because there is no electrostatic coupling between the domains through the dielectric layer, which further reduces the sensitivity to n_D of the simulations results. The experimental P_T versus E_{FE} curves for AFE ZrO$_2$ sometimes exhibit a non–negligible polarization at zero field, that is ascribed to the presence of ferroelectric domains. Therefore, in simulations, a small fraction of ferroelectric domains can be accounted for in the model by setting appropriate values of the anisotropy coefficients for such domains. More precisely, for the LGD parametrization of ferroelectric domains in ZrO$_2$, educated guesses were used for the remanent polarization $P_r \simeq 25$ μC/cm^2 and coercive field $E_{C,FE} \simeq 1.2$ MV/cm consistent with [130], [131], resulting in the following LGD parametrization: $\alpha_{FE} = -5.94 \cdot 10^8$ m^3/F, $\beta_{FE} = 4.28 \cdot 10^9$ m^5/(FC^2) and $\gamma_{FE} = 1.16 \cdot 10^9$ m^9/(FC^4), with every other simulation parameter kept fixed.

For ferroelectric domains, the coercive field was randomly distributed using a Gaussian distribution having the same σ_{EC} value used for antiferroelectric domains. The domain dependent anisotropy coefficients have a spatially random distribution across the domain grid, and their spatial distribution does not practically affect the simulation results. This is not unexpected especially for M-AFE-M stacks. In order to improve the agreement with experimental data, in simulations it is also possible to include a small built-in electric field in the ferroelectric material, possibly arising from a slight workfunction difference at the two electrodes or from fixed charges in the dielectric stack.

4.3.2 Double dielectric layer stacks
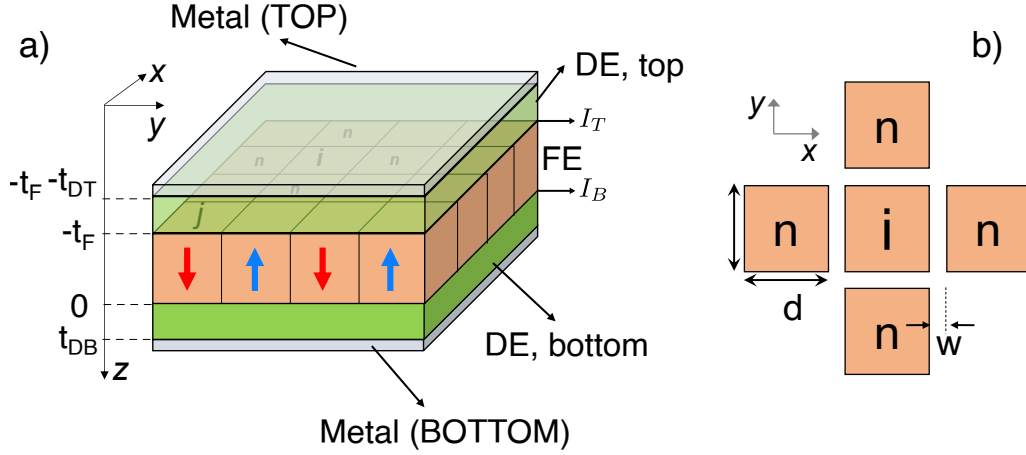
Figure 4.5: Sketch of the MDFDM device structure. a) 3D sketch where the thicknesses of the three layers are highlighted. The capacitance of each dielectric layer is defined as $C_{D-} = \varepsilon_0 \varepsilon_{D-}/t_{D-}$ for either the top (T) or bottom (B) dielectric. The background capacitance of the ferroelectric layer is defined as $C_F = \varepsilon_0 \varepsilon_F/t_F$. b) neighbours of the $i-$th domain which enter in the calculation of the domain wall energy components of Eq. (4.7). d is the domain size, w is the domain wall width.

For the simulation of MDFDM device stacks which will be later analyzed in this chapter, the framework and the dynamics equation are essentially the same as Eq. (3.1), the only variations present are due to the different electrostatics energy terms (as shown in Section 2.5) resulting from the presence of two dielectric layers instead of only one.

$$
\begin{aligned}
t_F \rho \frac{\partial P_i}{\partial t} = &- \left(2\alpha P_i + 4\beta P_i^3 - 6\gamma P_i^5\right) t_F + \\
&- \left[t_F \frac{k}{w} \frac{d}{(d+w)^2} \sum_n (P_i - P_n)\right] + \\
&- \left[\sum_{j=1}^{n_D} (P_j + Q_{S,j})/C_{ij}^{(dep)} - \frac{V_T}{2}\left(1 + B_i - \frac{C_S}{C_{DS}}\right)\right]
\end{aligned}
\tag{4.7}
$$

where $1/C_{i,j}^{(dep)} = 1/2(1/C_{j,i} + 1/C_{i,j})$ and in this case $C_{i,j}$ is defined as the contribution of the electrostatic coupling through the top and bottom dielectric $C_{i,j} = C_{i,j}^{(top)} + C_{i,j}^{(bottom)}$. The overall series capacitance C_S is defined as $1/C_S = (1/C_{DT} + 1/C_F + 1/C_{DB})$ while the series capacitance of only the dielectric layer C_{DS} is defined as $1/C_{DS} = (1/C_{DT} + 1/C_{DB})$. The term B_i is defined in Section 2.5. The equation considers ferroelectric domains having a fixed domain wall width.

4.4 Comparison with experimental results

	α [m/F]	β [m⁵/(FC²)]	γ [m⁹/(FC⁴)]	ε_F [-]	t_{ZrO_2} [nm]	E_{BI} [kV/cm]
[124]	$3.37 \cdot 10^9$	$-1.57 \cdot 10^{11}$	$3.24 \cdot 10^{12}$	23.76	5.3	0
[124]	$3.56 \cdot 10^9$	$-2.01 \cdot 10^{11}$	$4.50 \cdot 10^{12}$	22.09	9.5	-50
[116]	$2.95 \cdot 10^9$	$-8.97 \cdot 10^{10}$	$1.09 \cdot 10^{12}$	13.36	10	50

Table 4.1: Nominal values of the parameters extracted from Eqs. (4.4) and (4.5) for experiments from [124] and [116]. E_{BI} denotes a built-in electric field; the switching resistivity $\rho \sim 400$ Ωm was used in all simulations.

Figure 4.6: Comparison between simulations and experiments for quasi-static P_T versus E_{FE} curves of the TiN/ZrO₂/TiN capacitors from [124]. The triangular voltage waveforms at a 10 kHz frequency are shown in the insets. a) Thickness of the ZrO₂ layer $t_{\text{ZrO}_2} = 9.5$ nm, points used for parameters extraction: $(E_B, P_{T,B}) = (2.7$ MV/cm, 9.5 μC/cm²$)$; $(E_C, P_{T,C}) = (1.1$ MV/cm, 14.5 μC/cm²$)$. b) $t_{\text{ZrO}_2} = 5.3$ nm, $(E_B, P_{T,B}) = (2.9$ MV/cm, 14 μC/cm²$)$; $(E_C, P_{T,C}) = (2.4$ MV/cm, 16 μC/cm²$)$.

Table 4.1 reports the material parameters extracted with the methodology of this work from two experimental data sets, namely the P_T-E_{FE} curves recently reported in [124] and [116]. Quite interestingly, from the parameters in Table 4.1 one can calculate the zero field permittivity of ZrO₂, which is defined as $1/\varepsilon_0(\partial P_T/\partial E_{FE})$ at $E_{FE} = P_T = 0$. By recalling $P_T = P + \varepsilon_0\varepsilon_F E_{FE}$ and using Eq. (4.2a) for $(\partial P/\partial E_{FE})$, the zero-field permittivity is readily expressed as $(\varepsilon_F + 1/(2\alpha\varepsilon_0))$.

The zero field permittivity obtained from the parameters in Table 4.1 ranges between 30 and 40, which is in good agreement with experimental values in [132], [133]. The anisotropy coefficients in Table 4.1 provide the mean values of the domain dependent α_i, β_i, γ_i parameters used in the numerical simulations.

Figure 4.6 shows a comparison between simulations and experiments for the $P_T - E_{FE}$ curves of the M-AFE-M stacks reported in [124], and for the materials parameters in Table 4.1. In Figure 4.6a, the 3% of the overall domains were considered to be ferroelectric, with the parameters discussed in Section 4.3, while for Fig. 4.6b no ferroelectric domains were included, as it can be inferred from the fact that the hysteresis of the $P_T - E_{FE}$ curve is completely closed at zero applied electric field. In the model, the timescale for the polarization dynamics is set by $t_\rho = \rho/(2\langle \alpha \rangle)$ [76]. For $\rho \approx 400$ Ωm (see Table 4.1) the resulting t_ρ is ≈ 70 ns, which is consistent with the literature for large area devices [134], and ensures that simulations in Fig. 4.6 are quasi-static. While it could be argued that each stack could have its own ρ value, it is important to mention that there is no direct measurement to extract ρ which is usually inferred from polarization switching measurements [94]. Given the lack of a direct information about the value of ρ, its value was kept fixed for all stacks. The agreement between simulations and experiments is fairly good for both t_{ZrO_2} values, thanks to a good symmetry of the experiments along both the P_T and E_{FE} axis.

Fig. 4.7 reports a similar comparison for the experimental data set in [116], where it was assumed that the 4% of the total domains is ferroelectric. The agreement between simulations and experiments is still fairly good, but a discrepancy in the negative E_{FE} hysteresis can be noted. This is mainly due to an asymmetry in the measured P_T values for positive and negative E_{FE} at large $|E_{FE}|$, possibly due to a non-negligible influence of leakage. In this latter respect, while in the experimental dataset in [124] the leakage effects were compensated using the procedure described in [135], this is not the case in [116], resulting in asymmetries in the measured P_T. In fact, while an asymmetry along the E_{FE} axis can be included in the model through a built-in field E_{BI} (see Table 4.1), the LGD model is instead inherently symmetric in the P_T values, and this could be the reason for the lower quality of the agreement between simulations and experimental data in Fig. 4.7.

The authors of [116] also reported transient negative capacitance (NC) experiments, that are here analyzed by using the LGD model, as previously reported for the NC behaviour in ferroelectric devices [52], [76], [136], [137]. In the $TiN/ZrO_2/Al_2O_3/HfO_2/TiN$ stack the undoped HfO_2 layer is paraelectric and the thicknesses are: $t_{ZrO_2} = 10$ nm, $t_{Al_2O_3} \approx 1$ nm and $t_{HfO_2} = 8$ nm. The timescale of the voltage pulses in these experiments (now comparable to the t_ρ),

4. Modeling of $P - V$ urves and Negative Capacitance Experiments for Antiferroelectric ZrO_2
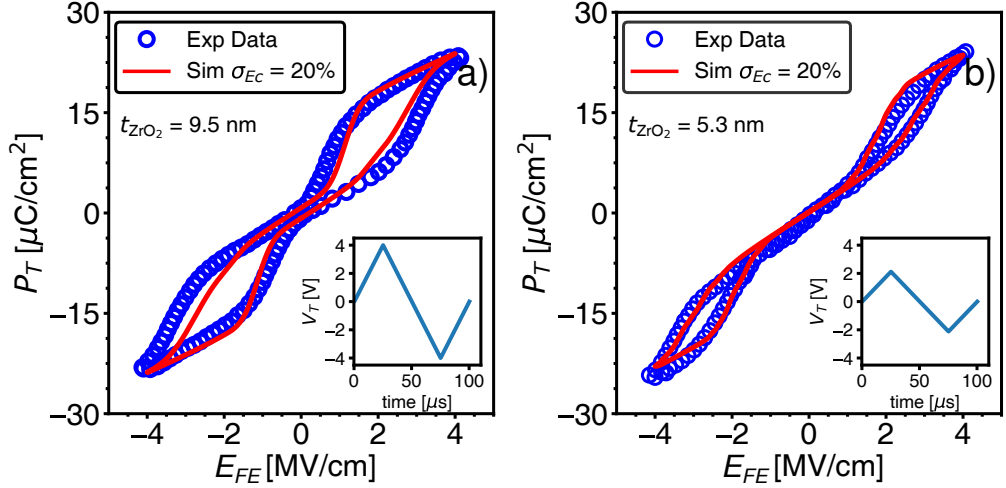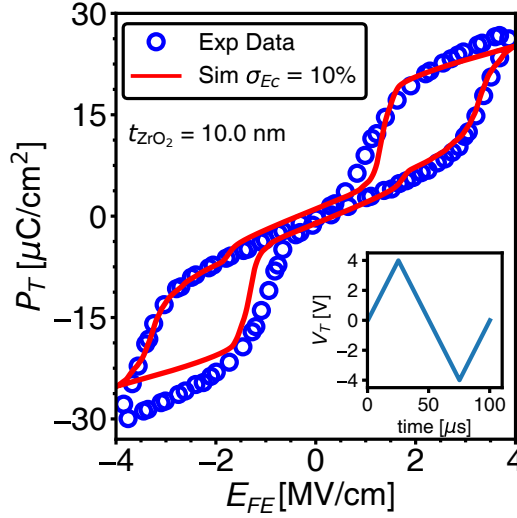

Figure 4.7: Comparison between simulations and experiments for quasi-static P_T versus E_{FE} curves of a TiN/ZrO$_2$/TiN capacitor from [116]. The triangular voltage waveforms at a 10 kHz frequency are shown in the inset. $(E_B, P_{T,B}) = (3.1$ MV/cm, 12 μC/cm^2); $(E_C, P_{T,C}) = (1.6$ MV/cm, 18 μC/cm^2). (©2023 IEEE)

and the relatively thick dielectrics were purposely chosen to minimize the role of charge injection and trapping [116]. Therefore, the simulations in transient regime neglect trapping, which has been shown to be instead important in quasi-static measurements for MFDM stacks with a thin dielectric layer.

Figure 4.8a and 4.8c compare the simulated and experimental $P_T - V_{max}$ curves for a pulse width of respectively of 275 ns and 1 μs, where V_{max} is the amplitude of the voltage pulse and the simulated P_T values have been extracted following the definition in [116], where the polarization values were obtained by subtracting the total polarization at the peak (either positive or negative) and at the end of the voltage pulse for each applied V_{max}. Figure 4.8b and 4.8d display the corresponding plots for the P_T versus an effective electric field, E_{EFF}, across the ZrO$_2$ layer. In experiments the E_{EFF} cannot be directly probed, hence it was estimated as $E_{EFF} \approx (V_{max} - P_T/C_D)/t_{ZrO_2}$, where $C_D \approx 1.78$ μF/cm^2 is the effective capacitance of the Al$_2$O$_3$-HfO$_2$ series [116]. In the simulations of Fig. 4.8b and 4.8d, the E_{EFF} was calculated according to the same definition given in [116]. Figure 4.8 shows that the same ZrO$_2$ parameters already employed in Fig. 4.7 (Table 4.1), both LGD mean values and their statistical distribution, can provide a fairly good agreement also for transient NC experiments, with a matching between simulations and experiments that is similarly good for the two different pulse widths.

Figure 4.9 reports a similar comparison between simulations and experi-
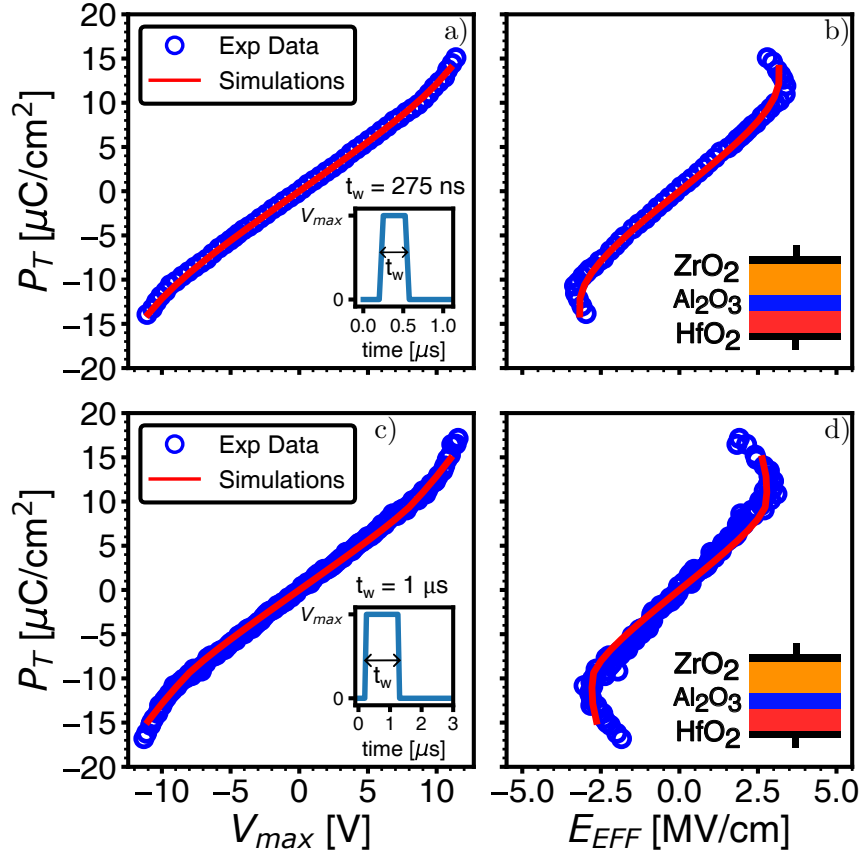
Figure 4.8: Comparison between simulations and experiments for transient negative capacitance measurements in a TiN/ZrO$_2$/Al$_2$O$_3$/HfO$_2$/TiN capacitor [116]. (a, c) P_T versus V_{max} curve for pulsed measurements with pulse width of 275 ns and 1 μs, respectively. (b, d) Corresponding P_T versus effective field, E_{EFF}, curve. (©2023 IEEE)

mental data for an HZO-based ferroelectric material stacked in two different configurations. An asymmetric structure, which resembles the device architecture of FTJs, but where the dielectric layer is relatively thick in order to prevent charge injection. A second structure that is instead symmetric, where the ferroelectric material is sandwiched between two thinner dielectric layers. In these device configurations, the dielectric is Al$_2$O$_3$. The measurement setup behind these experiments is conceptually the same as for the measurements in Fig. 4.8, where fast voltage waveforms are used to prevent charge injection and polarization screening, and the P_T values are also extracted with the same procedure reported in [116].

All simulation parameters are reported in the caption of Fig. 4.9. Figures 4.9a and 4.9b show the NC operation for the asymmetric structure and show

4. Modeling of $P - V$ urves and Negative Capacitance Experiments for Antiferroelectric ZrO$_2$
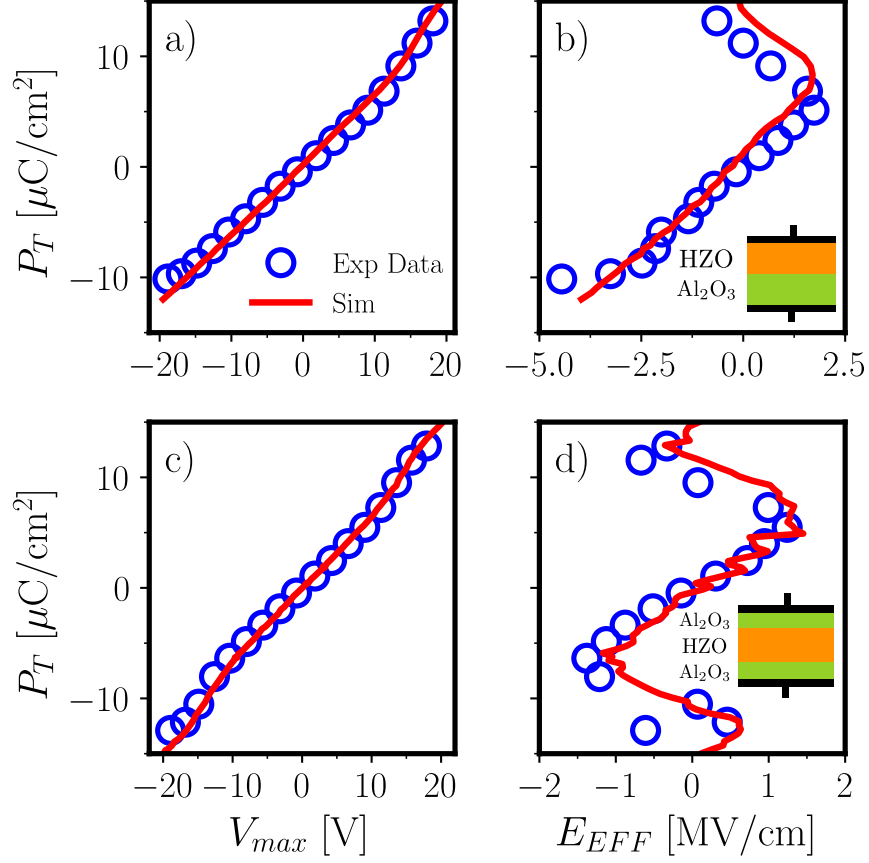
Figure 4.9: Comparison between simulations for $n_D = 400$ domains and experiment for NC operation in asymmetric and symmetric stack. The ferroelectric layer is 10 nm thick with the background dielectric constant $\varepsilon_F = 31$ in both structures and the total thickness of the dielectric layer is 10.8 nm with dielectric constant $\varepsilon_D = 9.08$. α, β and γ used in these simulations were set to $-8.22 \cdot 10^8$ m/F, $-1.26 \cdot 10^{10}$ m^5/(FC^2) and $7.46 \cdot 10^{11}$ m^9/(FC^4), respectively. a, b) report the P_T-V_{max} and the P_T-E_{app} characteristics for the asymmetric stack. c, d) report the same information but for the symmetric stack.

that the transient NC can be observed only for positive applied voltages, in fact in Fig. 4.9a only one change in the slope can be identified. This was ascribed to the presence of a fixed charge at the interface between the two layers that stabilizes only one polarity of the polarization [52]. On the other hand, Figures 4.9c and 4.9d show that NC behaviour can be observed for both voltage polarities and the same ferroelectric LGD parameters in the symmetric stack, as it can be seen by the two slope changes in Fig. 4.9c. In fact, in Section 2.5.1 it is shown that, if the two interfaces have the same

interfacial fixed charge and the dielectric layers have the same capacitance, the electric field in the ferroelectric layer is null for a zero external bias and both polarities of the polarization can be stabilized. Consequently, a positive and a negative external voltage can induce a polarization reversal. It is interesting to notice that these latter results closely resemble the ones illustrated in Fig. 4.8. This similarity can be attributed to the non-polar ground state of the ZrO_2, which results in a negligible interfacial trapped charge during the fabrication process [116], which is different from ferroelectric-dielectric hetero-structures where the ferroelectric tends to be always in a polar state. The results in this section support the validity of the extraction procedure for the material parameters of antiferroelectric ZrO_2 and, moreover, highlights the versatility of the simulation framework in the analysis of quasi-static and transient NC regimes for both antiferroelectric and ferroelectric materials.

4.5   Chapter conclusions

In this chapter, a procedure to extract the material parameters for the LGD model of antiferroelectric ZrO_2 films has been proposed, which is consistent with the microscopically non-polar nature of the zero field state in antiferroelectric ZrO_2 [116]. The points $(E_B, P_{T,B})$ and $(E_C, P_{T,C})$ necessary to extract the anisotropy coefficients for the LGD model can be reliably identified by a distinct change in the slope of the $P_T - E_{FE}$ curves (see Fig. 4.3b), provided that the curves are not significantly distorted by leakage and that they display a full hysteresis loop (as opposed to minor loops). The extraction methodology was successfully validated by analyzing quasi-static $P_T - E_{FE}$ curves of different M-AFE-M stacks, where a small percentage of simulated domains was considered to be ferroelectric in order to explain and reproduce the residual polarization at zero field observed in some of the ZrO_2 films [124]. Moreover, both the methodology and simulation framework were further validated by analyzing recent antiferroelectric experimental data of $P_T - E_F$ in both quasi-static and transient NC regime. Interesting links between NC operation in antiferroelectric materials and ferroelectric materials were also emphasized.

The analytical procedure for the extraction of the material parameters of antiferroelectric ZrO_2 has a clear physical background and it is easy to implement. The overall fitting results, however, can be less accurate than those obtained with more phenomenological approaches [119], [120], whose parameters are extracted by employing numerical optimization procedures. The analysis of antiferroelectric ZrO_2 layers can has possible applications in ferroelectric non-volatile memories and memristors, as well as in devices

exploiting the negative capacitance operation.

Chapter 5

Switching Propagation with LGD Model

5.1   Introduction

Thanks to the discovery of ferroelectricity in CMOS processing compatible fluorite-type $Hf_{0.5}Zr_{0.5}O_2$ [138], and wurtzite-type $Al_{1-x}Sc_xN$ materials [139], many perspective applications of ferroelectrics in electronic devices have emerged, including memories, transistors and memristors [1], [140].

Crucial to all applications is the understanding of the Polarization Reversal (PR) measurements. These measurements aim to understand the switching dynamics of ferroelectric materials and they are usually carried out by pre-setting the ferroelectric material in a known polarization state, then applying an electric field pulse with fixed magnitude and variable duration of the pulse. The duration of the pulse can go from hundreds of nanoseconds to tens of milliseconds, depending on the intensity of the applied electric field. After such a pulse, the device is reset by using a resetting waveform during which it is also measured the polarization that had been switched during the polarization reversal pulse. With this procedure, it is possible to extract the fraction of switched spontaneous polarization over time for different magnitudes of applied electric fields.

By analyzing ferroelectric samples with Piezoresponse Force Microscopy (PFM) measurements, it has been clearly established that Polarization Reversal in ferroelectric materials occurs as a non-uniform process [49], where the reversal starts from only a few sites, called nucleation sites, and then expands from the sites in larger regions. It is also usually assumed that virtually all nucleation events are caused by extrinsic causes, and occur at lattice defects or grain boundaries [40]. Moreover, grain boundaries are usually

responsible for the stop of the reversal process [47] and this is very relevant for poly-crystalline materials, which naturally have a remarkably high number of grain boundaries.

As stated in Section 2.2, the polarization reversal in epitaxial materials is usually described with the phenomenological Kolmogorov-Avrami-Ishibashi (KAI) model [44]

$$P(t) = 2P_r \cdot \left\{ 1 - \exp\left[\left(-\frac{t}{\tau} \right)^n \right] \right\} \tag{5.1}$$

where n is the dimension of the domain growth (usually $n = 2$) and τ is the characteristic switching time, that is known to depend on the nucleation rate and the domain wall velocity [141]. Normally, τ is extracted from measurements and in particular is assumed as the time when the polarization reversal reaches the 63% threshold. The dependence of τ on the applied electric field E_{app} is usually expressed in terms of the Merz' Law [142]

$$\tau = t_0 \cdot \exp\left(\frac{E_a}{E_{app}} \right) \tag{5.2}$$

where E_a is the so-called activation field, which can be extracted as the slope of the experimental $\log_{10}(\tau)$ versus $1/E_{app}$ characteristic, and t_0 is a fitting prefactor [141]. The idea behind the KAI model is the unrestricted propagation of a nucleation in a crystal with infinite size [44], and it is applicable to single-crystal or epitaxial materials having very large grain sizes [143]. This model, however, proves to be ineffective in the description of poly-crystalline ferroelectric materials, especially at very low applied electric fields. In more general terms, the model is not suitable to describe experimental datasets where the polarization reversal characteristic displays a polarization switching over a broad range of times [47].

To overcome the limitations of the KAI model a reformulation has been introduced where a statistical distribution of the characteristic switching time is introduced, in order to better describe the polarization reversal experiments in ferroelectric thin films that are usually poly-crystalline [47], [48]. The poly-crystalline nature of the material results in a large number of grain boundaries that stop the propagation of the nucleation and unther these circumstances the dominating mechanism behind polarization reversal becomes the rate of nucleation events. In this framework, also called Nucleation-Limited Switching (NLS), the propagation of a nucleation occurring in a grain is almost instantaneous considering the size of the latter. The equation of the

NLS model is the following

$$P(t) = 2P_r \cdot \int\limits_{-\infty}^{+\infty} \left\{ 1 - \exp\left[\left(-\frac{t}{t_N}\right)\right] \right\} F(\log_{10}(t_N)) \, d(\log_{10}(t_N)) \qquad (5.3)$$

where now the KAI-like term between brackets is weighed with a probability density function $F(-)$ for the nucleation times with t_N being the nucleation time. Usually, F is taken as a Lorentzian probability density function [48], [144]

$$L(\log_{10}(t_N)) = \frac{A \, w}{\pi \left[(\log_{10}(t_N) - \log_{10}(t_M))^2 + w^2 \right]} \qquad (5.4)$$

where t_N is again the nucleation time, A is a normalization constant, w is defined as the half-width-at-half-maximum of the Lorentizan and t_M is the mean time of the nucleations. Examples of this function will be reported later in this chapter.

Figure 5.1 reports a useful comparison of switching times that highlights the difference between KAI and NLS behaviour in polarization reversal measurements. By defining t_{inc} as the time needed for the polarization reversal to reach the 20% of the overall switching dynamics and t_{sw} as the additional time (after t_{inc}) to reach the 80% of the switching. Figure 5.1 clearly shows that a KAI-like behaviour is characterized by a fairly constant ratio t_{sw}/t_{inc} (cross and hexagonal markers) for different applied electric fields, while for the NLS-like behaviour this ratio steeply increases at lower applied fields (remaining markers).

KAI and NLS models provide a phenomenological description of the Polarization Reversal in ferroelectric materials, however, in the context of the more physics-based Landau, Ginzburg, Devonshire (LGD) framework, Polarization Reversal measurements have received less attention than other types of measurements [145], such as quasi-static large–signal P-V, small–signal C-V and transient Negative Capacitance [52], [53], [146], [147]. Moreover, the LGD framework has been universally employed assuming an intrinsic nucleation scenario, where the ferroelectric material parameters are calibrated so as to have the field for intrinsic nucleations similar to the coercive field extracted from $P - V$ measurements, namely to have $E_{IN} \approx E_{C,exp}$. However, it has been repeatedly reported in *ab-initio* studies that the calculated coercive field, E_{IN}, for an intrinsic nucleation is much larger than the coercive field, $E_{C,exp}$, observed in $P - V$ experiments [148], [149], which is consistent with the extrinsic nature of nucleations.

Summarizing, the LGD model is used to describe intrinsic nucleation events with the extrinsic ones simply being neglected. In this chapter, the LGD
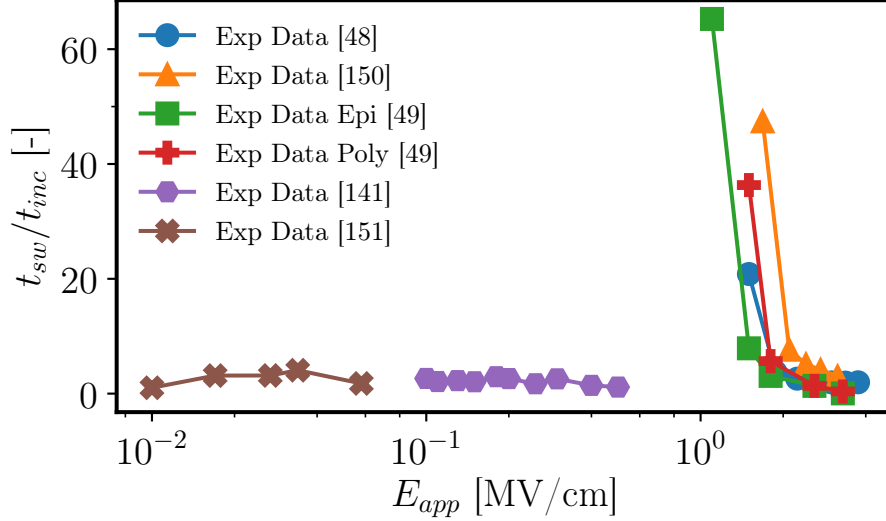
Figure 5.1: Switching times ratio versus applied electric field for different experimental datasets. Switching times ratio is constant for materials exhibiting KAI-like behaviour while it greatly increases at lower applied electric fields for materials exhibiting NLS-like behaviour.

model based on intrinsic nucleations and calibrated against $P - V$ measurements will be proven to be quite ineffective in reproducing PR experiments, exhibiting large discrepancies between simulations and experimental data. The discrepancies can be reconciled by implementing a revised version of the model, in which the LGD framework is not used to describe intrinsic nucleations but rather to enable the propagation of the polarization switching triggered by extrinsic nucleations, with a coercive field for propagation, E_{SP}, much smaller than E_{IN}. The results show that the revised model can improve the agreement with $P - V$ and polarization reversal experiments for different data sets, and also help elucidate the differences between PR in poly-crystalline and epitaxial ferroelectrics.

5.2 Nucleation and propagation in LGD model

We here start by recalling the thermodynamic potential employed in the LGD model for the description of a ferroelectric material reported in Section 2.3

$$U(P, \nabla P) = \int_V \underbrace{\left[\alpha P^2 + \beta P^4 + \gamma P^6 - \frac{\varepsilon_0 \varepsilon_F}{2} E_{app}^2 - E_{app} \cdot P + k \left| \nabla P \right|^2 \right]}_{=g(P, \nabla P)} d\boldsymbol{r} dz$$

(5.5)

This thermodynamic potential is a functional of the polarization and it is used to write the dynamic equation for the spontaneous polarization P (assumed to be aligned along the axis z) according to the Landau-Khalatnikov equation, (already discussed in Chapter 2)

$$\rho \frac{\partial P}{\partial t} = -\frac{\delta U(P, \nabla P)}{\delta P}$$

(5.6)

where E_{app} denotes the z component of the electric field in the ferroelectric, α, β, γ are the anisotropy coefficients, ρ is a resistivity setting the time scale $t_\rho = \rho/(2|\alpha|)$ of the dynamics, and k is the domain wall coupling factor [53], [128]. All these parameters were already introduced in Chapter 2 and Section 3.2.

The notation $\delta U(P, \nabla P)/\delta P$ indicates the variational derivative of the LGD energy functional, which can be evaluated as [152]:

$$\frac{\delta U}{\delta P} = \frac{\partial g}{\partial P} - \nabla \cdot \left(\frac{\partial g}{\partial (\nabla P)} \right)$$

(5.7)

In previous chapters, the starting point of the derivations has always been the discretized version of the Gibbs' energy functional g, where the domain-wise polarization P_i becomes an algebraic unknown, and the ferroelectric material is divided in n_D domains having a fixed domain size d and domain wall width w. Under these approximations, the Gibbs' free energy becomes a function of the polarizations P_i in each domain. In this chapter, instead, for the moment we continue with the continuous formulation in Eq. (5.5) and then evaluate the functional derivative in Eq. (5.7) as

$$\frac{\delta U}{\delta P} = 2\alpha P + 4\beta P^3 + 6\gamma P^5 - E_{app} - 2k\nabla^2 P$$

(5.8)

According to Eq. (5.6), the dynamic equation for the spontaneous polarization is:

$$\rho \frac{\partial P}{\partial t} = -2\,\alpha P - 4\,\beta P^3 - 6\,\gamma P^5 + E_{app} - 2k\,\nabla^2 P$$

(5.9)

This approach results in some differences with the previous implementations that we will get back to and clarify in Section 5.3.

Equation (5.9) entails two possible switching mechanisms triggered by a large enough E_{app}.

The first is the Intrinsic Nucleation (**IntNucl**), which is mainly governed by α, β and γ, that in the LGD framework set the coercive field of the ferroelectric material, and describes the flipping of the elementary dipole. By setting to zero the value of the domain wall coupling k in Eq. (5.9) it is possible to calculate the energy barrier for the intrinsic nucleation of a single polarization site. In particular, the energy required for a uniform switching U_{IN} can be expressed by $U_{IN} = (3\sqrt{3}/8)P_r/E_{IN}$ (energy per switched volume), where P_r is the remanent polarization and E_{IN} is the coercive field for the intrinsic nucleation (see Fig. 5.2a).

The second mechanism is the propagation of an extrinsic nucleation, which is mainly governed by k. In fact, as it can be seen in Fig. 5.2b, while the energy barrier U_{IN} for an intrinsic nucleation can be quite large, by employing a non-negligible value of the domain wall coupling factor k the energy required to propagate the nucleation, U_{SP}, can be quite lower than U_{IN}.

While in the conventional LGD model based on the **IntNucl** scenario the anisotropy coefficients are calibrated to reproduce the remanent polarization, in the Extrinsic Nucleation (**ExtNucl**) scenario discussed in this chapter, instead, the LGD model describes the switching propagation triggered by extrinsic nucleations.

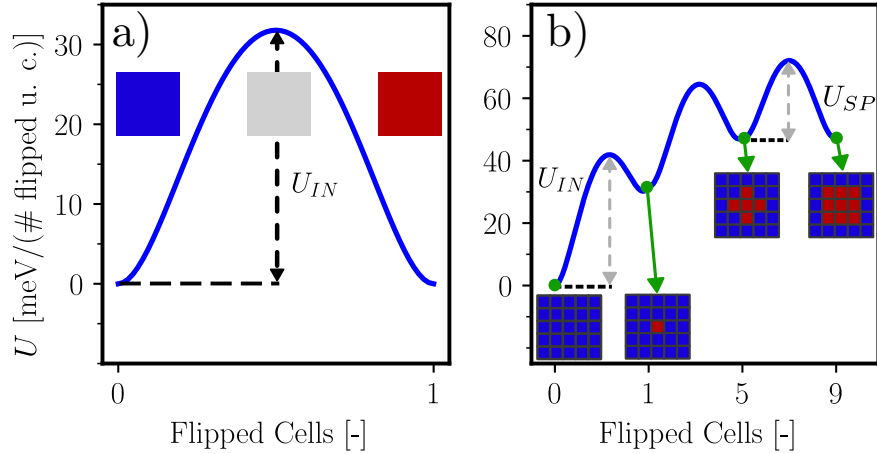**Figure 5.2:** a) Energy landscape for the homogeneous switching. b) Energy landscapes at $E_{app} = 0$ for the polarization transitions shown in the sketches. U_{IN} is the energy barrier for the intrinsic nucleation and U_{SP} is the barrier for the propagation of nucleations obtained with a non–negligible k value.

By assuming that an extrinsic nucleation occurred at a given site, then the

energy barrier U_{SP} for switching propagation can be much smaller than the barrier U_{IN} for intrinsic nucleation (see Fig. 5.2b). The corresponding coercive field, E_{SP}, that triggers propagation is also much smaller than E_{IN}. Therefore, a novel formulation of the LGD model based on the Extrinsic Nucleation (**ExtNucl**) scenario is explored, where now the anisotropy coefficients are calibrated to reproduce P_r but result in an E_{IN}, much larger than $E_{C,exp}$. $E_{C,exp}$ is instead reproduced by tuning the domain wall coupling factor k so as to obtain $E_{SP} \approx E_{C,exp}$. In this scenario, large site-to-site variations of E_{IN} become unnecessary, but a field-dependent rate of extrinsic nucleation events is introduced, which is further discussed in the next sections.

5.3 Simulations and Comparison to Experiments
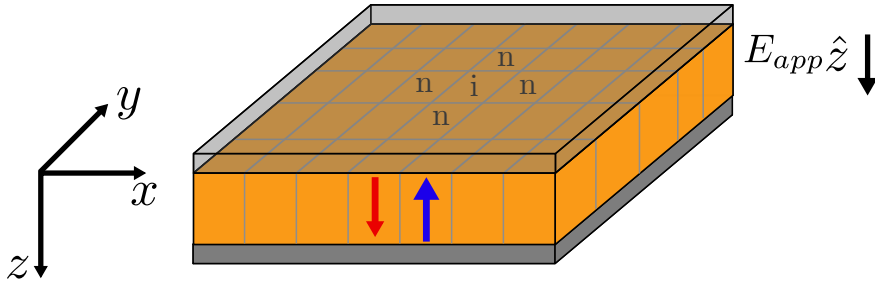
Figure 5.3: Sketch of a ferroelectric capacitor. The polarization is considered positive (red arrow) when aligned with the versor z, otherwise it is considered negative. Elementary sites obtained by discretization are labeled with the letter i. The neighboring sites used in the discretized version of the Laplacian operator are labeled with the letter n and are used in Eq. (5.10).

In this section, the **IntNucl** and **ExtNucl** version of the LGD model are compared with experimental data, chosen among measurement sets reporting both $P-V$ and polarization reversal data for the same samples. Equation (5.9) is numerically solved by using real-space discretization so as to obtain

$$\rho \frac{\partial P_i}{\partial t} = -2\alpha_i P_i - 4\beta_i P_i - 6\gamma_i P_i + E_{app} - \frac{2k}{d^2} \sum_{ni} (P_i - P_{ni}) \qquad (5.10)$$

where d is the size of the elementary polarization site, and α_i, β_i, γ_i depend on the site i and $-\sum_{ni}(P_i - P_{ni})$ is the discretized version of the Laplacian

operator obtained by expressing the derivatives according to a central finite difference representation.

Differently from previous implementations of the LGD model which assumed uniform polarization inside each ferroelectric domain (or grain) and a fixed size for the domain and domain wall region [53], [79], [153] (see also Chapters 3 and 4), here Eq. (5.10) describes the elementary polarization sites inside a ferroelectric domain (or grain), and in all calculations the size d of the discretization step is set to 0.5 nm, namely approximately the unit cell size of actual ferroelectric materials [154], [155].

In the simulation of poly-crystalline ferroelectric materials (e.g. doped HfO_2) square domains with a 5.5 nm side (i.e. 11×11 elementary sites) are used, and the grain boundaries that stop the propagation of the polarization switching are emulated by setting to zero the domain wall coupling k of the elementary sites surrounding each domain (see Fig. 5.4a). In epitaxial materials (e.g.

a) Poly-crystalline ferroelectric   b) Epitaxial ferroelectric
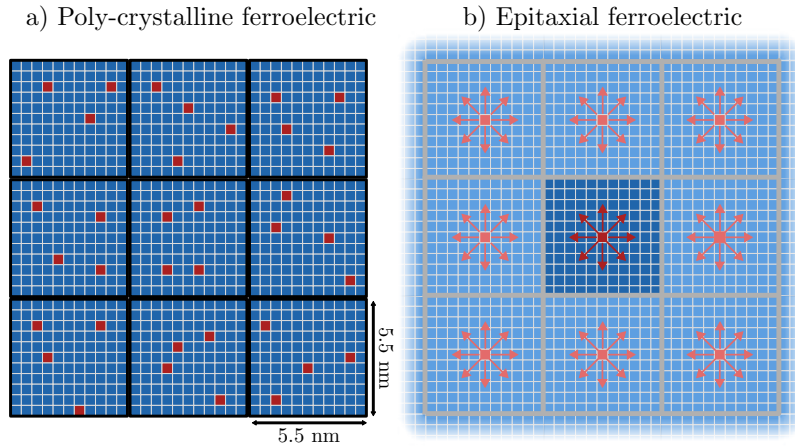
Figure 5.4: Sketch of the simulation arrangement for a poly-crystalline or an epitaxial material. Red squares indicate nucleated sites. (a) In poly-crystalline ferroelectrics, domains having a 5.5 nm side are separated by a dielectric border (solid black line) where the switching propagation is blocked. b) Epitaxial materials have much larger grains which would require a great computational effort and so, to reduce the computational burden periodic boundary conditions were used: the simulated area (darker square) is replicated indefinitely by periodization essentially emulating the behaviour of much larger areas.

PZT samples from [141]), given the relatively large grain size with respect to poly-crystalline materials, periodic boundary conditions were used in order to emulate larger device areas with a tolerable computational effort. Periodic boundary conditions replicate the simulated domain indefinitely, thus effectively emulating the switching propagation that occurs in large domains (see Fig. 5.4b).

Differently from previous chapters, here a field-dependent resistivity $\rho = \rho(E_{app})$ was used. The dependence is based on the Merz' Law already introduced in Section 5.1 [142]

$$\rho = \rho_0 \cdot \exp\left(\frac{E_a}{E_{app}}\right) \qquad (5.11)$$

where E_{app} is the applied electric field and E_a being the activation field that can be extracted by polarization reversal measurements [48], [141].

5.3.1 Intrinsic Nucleation LGD Model
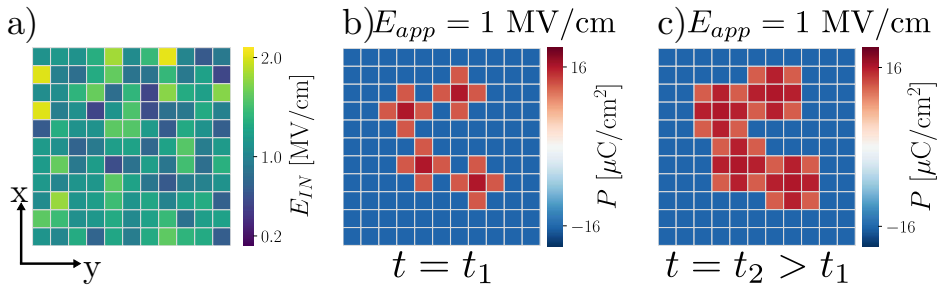
Figure 5.5: IntNucl scenario showing: (a) site to site variations of E_{IN}, (b) intrinsic nucleation at sites with smallest E_{IN} and time t_1, (c) switching propagation at time $t_2 > t_1$.

Figure 5.5 represents the **IntNucl** scenario. In particular, Fig. 5.5a shows the statistical distribution of the switching elements in the **IntNucl** scenario, and Figs. 5.5b and 5.5c show that only sites having $E_{IN} \leq E_{app}$ produce a polarization switching (Fig. 5.5b), which then propagates to the adjacent sites (Fig. 5.5c) depending on the value of k. In this scenario, the LGD model is calibrated to have $E_{IN} \approx E_{C,exp}$, and then site to site variations of E_{IN} are typically introduced to reproduce the tilted Large–Signal $P - V$ measurements.

Figure 5.6a reports a comparison between simulations obtained with the **IntNucl** LGD framework and experiments for the poly-crystalline, Si-Doped HfO$_2$ samples in [48], where the total polarization is defined as $P_T = P + \varepsilon_0(\varepsilon_F - 1)E_{app}$, with ε_F being the background polarization constant for the ferroelectric material. The corresponding values for E_{IN} and P_r are reported in Table 5.1. Consistently with [48], [129], in Fig. 5.6 a null domain wall coupling factor k was assumed resulting in a negligible domain wall propagation. Table 5.1 and Fig. 5.6a show that the mean value for E_{IN} is close to $E_{C,exp}$ (as anticipated in Section 5.2), and it is much smaller than the *ab-initio* predicted values larger than 5 MV/cm [148], [149]. Moreover, a quite
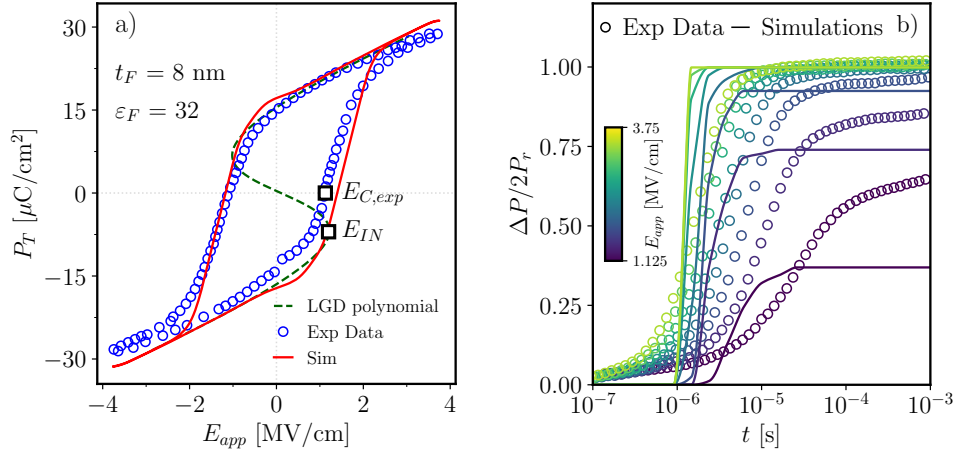
Figure 5.6: Comparison between **IntNucl** LGD simulations and experiments for poly-crystalline, Si-doped HfO_2 capacitors [48]. (a) Total polarization P_T versus applied field E_{app}. The dashed line is the plot of the corresponding 6-th grade Landau polynomial. (b) Corresponding polarization reversal simulations with E_{app} ranging from 1.125 to 3.75 MV/cm. All simulation parameters are reported in **Tab. 5.1**.

large E_{IN} dispersion, $\sigma_{E_{IN}}$, is necessary to reproduce the tilted transition in the experimental $P - V$ curves (see Table 5.1). Figure 5.6b shows the analysis of the corresponding polarization reversal experiments from [48]. For the same parameters as in Fig. 5.6a, simulations exhibit quite large discrepancies with polarization reversal experiments. In the **IntNucl** LGD model, in fact, polarization reversal is governed by a single time constant for each E_{app}, whereas the extrinsic nucleation times in poly-crystalline materials vary in a broad range [47].

Moving now to an epitaxial material, Figure 5.7 reports a similar analysis for the $P - V$ and polarization reversal experiments of the epitaxial PZT samples in [141]. Even in this case, the extracted E_{IN} for the **IntNucl** model is close to $E_{C,exp}$ and much smaller than the one predicted by *ab-initio* calculations [156]. Here the k value used was estimated in [157], which results in a quite steep transition in $P - V$ curves in spite of the site-to-site dispersion $\sigma_{E_{IN}}$ of the E_{IN} values. With the same parameters used for $P - V$ curves, the agreement with polarization reversal experiments in Fig. 5.7b is again poor, particularly at small E_{app}. In fact, the influence of k results in much steeper and faster transitions compared to the experimental polarization reversal curves. The datasets in Fig. 5.6 and Fig. 5.7 are representative of respectively an NLS and a KAI scenario for polarization reversal [48], [141]. In both cases, the **IntNucl** LGD model calibrated against $P - V$ curves fails to reproduce the polarization reversal data and results in E_{IN} values much smaller than *ab-initio* predictions. In the next section it will be shown how
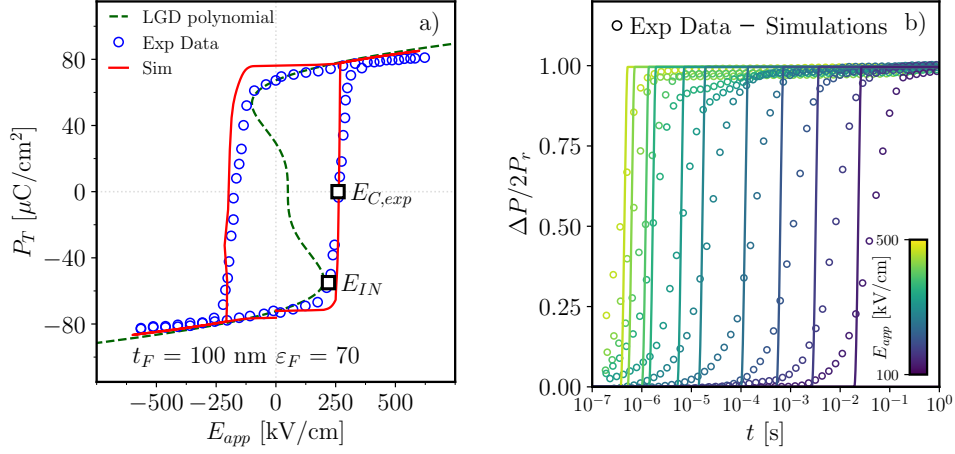
Figure 5.7: Same comparison as in Fig. 5.6 for **IntNucl** simulations, but here for epitaxial $Pb(Zr_{0.4}Ti_{0.6})O_3$ thin films [141]. a) Total polarization P_T versus applied field E_{app}. The dashed line is the plot of the corresponding 6-th grade Landau polynomial. b) Corresponding polarization reversal simulations with E_{app} ranging from 100 to 500 kV/cm. All simulation parameters are reported in Table 5.1.

the **ExtNucl** formulation for the LGD model can improve this situation for both polarization reversal scenarios.

	IntNucl: LGD parameters data from Fig. 5.6	IntNucl: LGD parameters data from Fig. 5.7
E_{IN} [MV/cm]	1.12	0.15
$\sigma_{E_{IN}}$ [%]	30	30
P_r [μC/cm^2]	16	70
E_a [MV/cm]	1.9	0.9 @ $E_{app} < 0.25$ MV/cm 2.8 @ $E_{app} \geq 0.25$ MV/cm
ρ_0 [Ωm]	1500	0.012 @ $E_{app} < 0.25$ MV/cm 12 @ $E_{app} \geq 0.25$ MV/cm
k [m^3/F]	0	$4.55 \cdot 10^{-11}$
α [m/F], β [m^5/(FC^2)], γ [m^9/(FC^4)]	$-7.89 \cdot 10^8$, $8.94 \cdot 10^9$, $1.69 \cdot 10^{11}$	$-8.45 \cdot 10^3$, $-5.88 \cdot 10^7$, $7.99 \cdot 10^7$

Table 5.1: E_{IN} is the mean value of the coercive field for intrinsic nucleation and $\sigma_{E_{IN}}$ is the corresponding standard deviation (normalized to E_{IN}) for a site-to-site Gaussian distribution of the E_{IN} values. P_r and k are defined in the text, while ρ_0 and E_a describe the ρ dependence on E_{app} according to Merz' law in Eq. (5.11).

5.3.2 Extrinsic Nucleation LGD Model
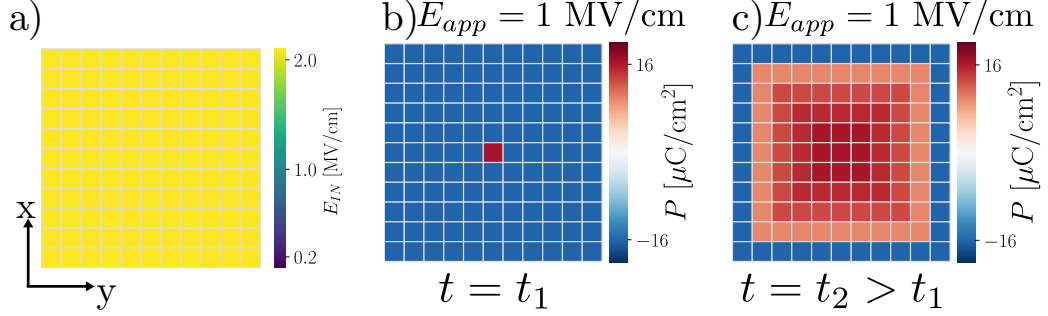
Figure 5.8: ExtNucl scenario showing: (a) negligible site to site variations of E_{IN}, (b) extrinsic nucleation at time t_1, (c) switching propagation at time $t_2 > t_1$.

The **ExtNucl** scenario is illustrated in Fig. 5.8, where a negligible site-to-site variation of the coercive fields is considered (Fig. 5.8a). In this scenario, a nucleation site at the center of the grain is used as a starting condition for the simulation, see Fig. 5.8b. Then, the evolution of the system is simulated under the influence of a fixed E_{app} (Fig. 5.8c); results depend on the value of the domain wall coupling factor k. In the simulation procedure for the **ExtNucl** scenario, the time evolution described by the LGD model is periodically stopped and new extrinsic nucleation sites are generated according to Eq. (5.4). Such new sites are then used as initial conditions when the time
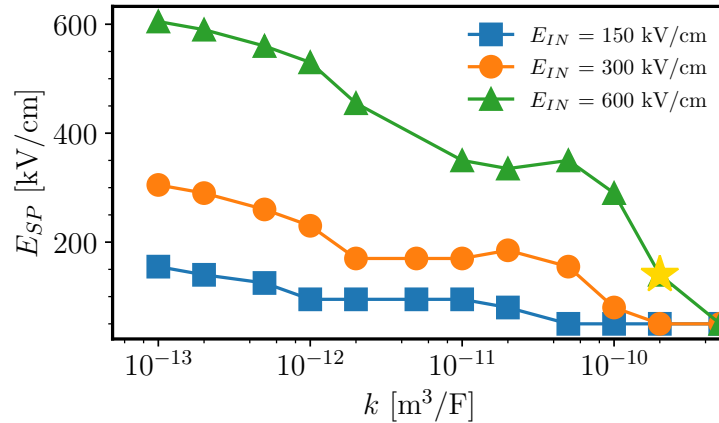
Figure 5.9: Coercive field E_{SP} for switching propagation versus the domain wall coupling constant k, and for different E_{IN} values. E_{SP} is smaller than E_{IN}. The yellow star indicates the k value used in simulations of Fig. 5.10 that for $E_{IN} = 600$ kV/cm results in $E_{SP} = 150$ kV/cm and is consistent with $E_{C,exp}$ estimated from experiments.

evolution is restarted. Figure 5.2b shows some zero field energy landscapes calculated by varying the sites' polarization in the discretized version of Eq. (5.5), and corresponding to either the intrinsic nucleation of a new site (first branch, energy barrier U_{IN}), or the propagation of a nucleation to adjacent sites (second and third branch). The barrier U_{SP} for the switching propagation is here substantially lower than U_{IN}, so that the corresponding coercive field E_{SP} is smaller than E_{IN}. Thus, the coercive field E_{SP} for switching propagation is also smaller than E_{IN}. In this latter respect, Fig. 5.9 reports the numerically calculated E_{SP} versus k, defined as the minimum E_{app} required to obtain the switching of all the simulated polarization sites after extrinsic nucleations have occurred. Such a difference between E_{SP} and E_{IN} is in qualitative agreement with recent findings for HfO_2 [149]. Hence, in the **ExtNucl** model, the anisotropy coefficients can be calibrated to reproduce P_r and have $E_{SP} \approx E_{C,exp}$ (with $E_{IN} > E_{C,exp}$). Moreover, site-to-site variations of E_{SP} (or E_{IN}) become unnecessary and were set to negligible values in the **ExtNucl** simulations. The density, D_N, of extrinsic nucleation sites is a parameter of the **ExtNucl** model and is defined as the number of sites per ferroelectric area. Table 5.2 reports the D_N values, here expressed as the

	ExtNucl: LGD parameters data from [48], Fig. 5.11a	ExtNucl: LGD parameters data from [141], Fig. 5.10a	ExtNucl: LGD parameters data from [158], Fig. 5.11b
E_{IN} [MV/cm]	4	0.6	0.25
σ_{EIN} [%]	1	1	1
P_r [μC/cm^2]	16	70	75
E_a [MV/cm]	1.9	0.6 @ $E_{app} < 0.2$ MV/cm 2.65 @ $E_{app} \geq 0.25$ MV/cm	0.29@$E_{app} < 0.18$ MV/cm 0.74@$E_{app} \geq 0.18$ MV/cm
ρ_0 [Ωm]	10	0.01@$E_{app} < 0.25$ MV/cm 5@$E_{app} \geq 0.25$ MV/cm	0.01
k [m^3/F]	$3.25 \cdot 10^{-10}$	$1.95 \cdot 10^{-10}$	$6.5 \cdot 10^{-11}$
Nucleation Density D_N [%]	0.86	3.3	0.86
α [m/F], β [m^5/(FC^2)], γ [m^9/(FC^4)]	$-2.82 \cdot 10^8$, $3.19 \cdot 10^9$, $6.03 \cdot 10^{10}$	$-3.38 \cdot 10^4$, $-2.35 \cdot 10^8$, $3.19 \cdot 10^8$	$-9.39 \cdot 10^3$, $-2.90 \cdot 10^7$, $1.76 \cdot 10^7$

Table 5.2: In [48] the ferroelectric material examined is Si:HfO$_2$, in [141] the ferroelectric material is Pb(Zr$_{0.4}$Ti$_{0.6}$)O$_3$ and in [158] the material is BFO grown on SrRuO$_3$/SrTiO$_3$. E_{IN} is the mean value of the coercive field for intrinsic nucleation and $\sigma_{E_{IN}}$ is the corresponding standard deviation (normalized to E_{IN}) for a site-to-site Gaussian distribution of the E_{IN} values. P_r and k are defined in the text, while ρ_0 and E_a describe the ρ dependence on E_{app} according to Merz' law in Eq. (5.2).

ratio of the area of nucleated sites to the total simulated area. In this respect, the propagation of a larger nucleated area requires lower values of the domain wall coupling factor k at the same value of applied electric field E_{app}. Given

the lack in the literature of dependable values of the size of the nucleation sites, in this chapter the value of D_N was adjusted to obtain a k value in agreement with previously reported values for perovskite ferroelectrics [157].
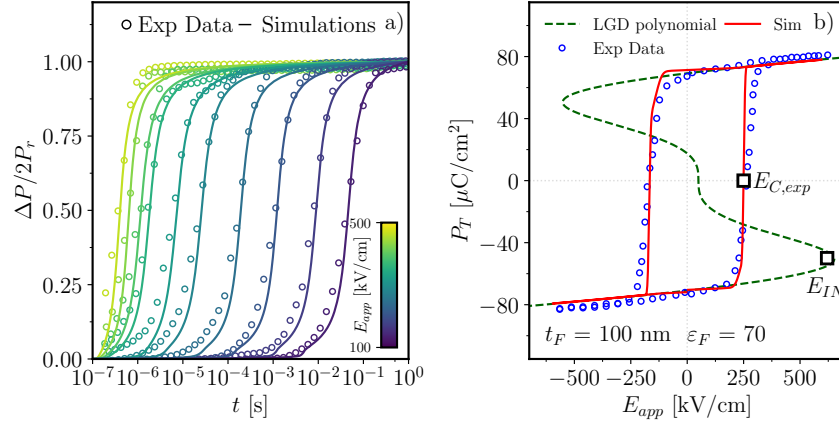
Figure 5.10: Same comparison as in Fig. 5.7, but here by using the **ExtNucl** model. a) polarization reversal analysis with E_{app} ranging from 100 to 500 kV/cm. b) Total polarization P_T versus E_{app}. The dashed line is the plot of the corresponding 6-th degree Landau polynomial, showing an E_{IN} much larger than $E_{C,exp}$ (see also the yellow star in Fig. 5.9). All simulation parameters are reported in Table 5.2.

Figure 5.10a shows that the **ExtNucl** model can achieve a better agreement, compared to Fig. 5.7b, with the polarization reversal experiments in [141]. The parameters of the Lorentzian function for the nucleation times are displayed in Fig. 5.12. Figure 5.10b shows that the same parameters can reproduce well also the $P - V$ curves. As it can be seen in Fig. 5.10b, E_{IN} of this scenario is larger than the E_{app} values spanned in [141] and closer to *ab-initio* calculations [148], which is consistent with an **ExtNucl** scenario, where nucleations are extrinsic and LGD equations govern the propagation of such extrinsic nucleations. The corresponding E_{SP} is ≈ 150 kV/cm (see the star in Fig. 5.9).

Figure 5.11a shows that, even for the data set in [48], the **ExtNucl** LGD model can reproduce experiments better than the **IntNucl** counterpart in Fig. 5.6b. Table 5.2 shows that, for the **ExtNucl** results, a non-null k value between sites is necessary to propagate extrinsic nucleations. This is consistent with a recent analysis based on *ab-initio* calculations [149], demonstrating that polarization switching based on nucleation and growth is indeed feasible in HfO_2 and doped HfO_2. Figure 5.11b reports further tests with the **ExtNucl** LGD model against the polarization reversal experiments for epitaxial $BiFeO_3$ thin films in [158], and Fig. 5.12 displays the field dependent parameters
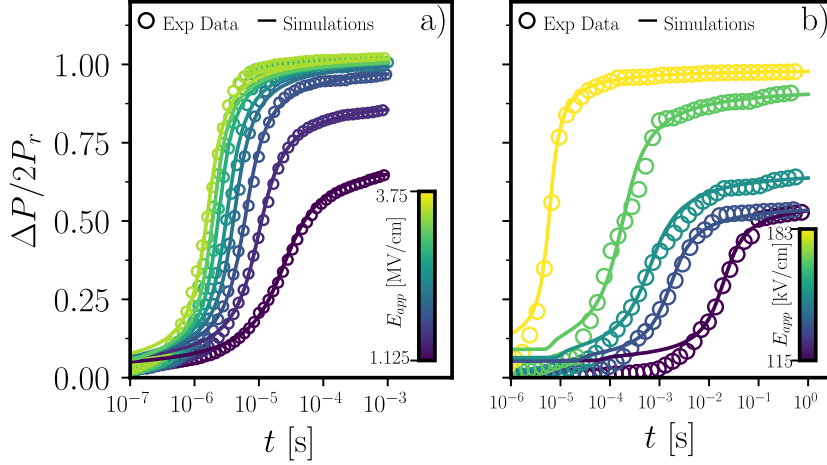
Figure 5.11: Comparison between **ExtNucl** LGD simulations and experiments for: (a) poly-crystalline, Si-doped HfO$_2$ capacitors from [48]; (b) Epitaxial BiFeO$_3$ capacitors from [158]. All simulation parameters are reported in Table 5.2.

$\log_{10}(t_M/s)$ and w of the Lorentzian function (see Eq. (5.4)) extracted from comparison to experiments. For the data in [141], Fig. 5.12b reveals that the w is fairly independent of E_{app}, and Fig. 5.12c shows that the corresponding nucleation times, t_N, have a small dispersion around the mean value t_M. This behavior is representative of a KAI scenario dominated by a single time constant [44], namely the propagation time constant that in the model is governed by the LGD equation. Figure 5.12b also shows that for the data in [48] and [158], instead, the w steeply increases at small E_{app}, corresponding to a large dispersion of nucleation times in Fig. 5.12d. This is representative of the NLS scenario for polarization reversal [47], in which a broad dispersion of nucleation times plays an important role in the shaping of the polarization reversal curves. A similar Lorentzian parametrization can be also extracted for the data in [158]. The present analysis suggests that even epitaxial materials can exhibit an NLS behavior in polarization reversal experiments at small E_{app}, which is consistent with the conclusions in [158]. Moreover, it is here demonstrated that an LGD equation based on the **ExtNucl** formulation can describe equally well both the KAI and the NLS scenarios, upon appropriate calibration of the model.
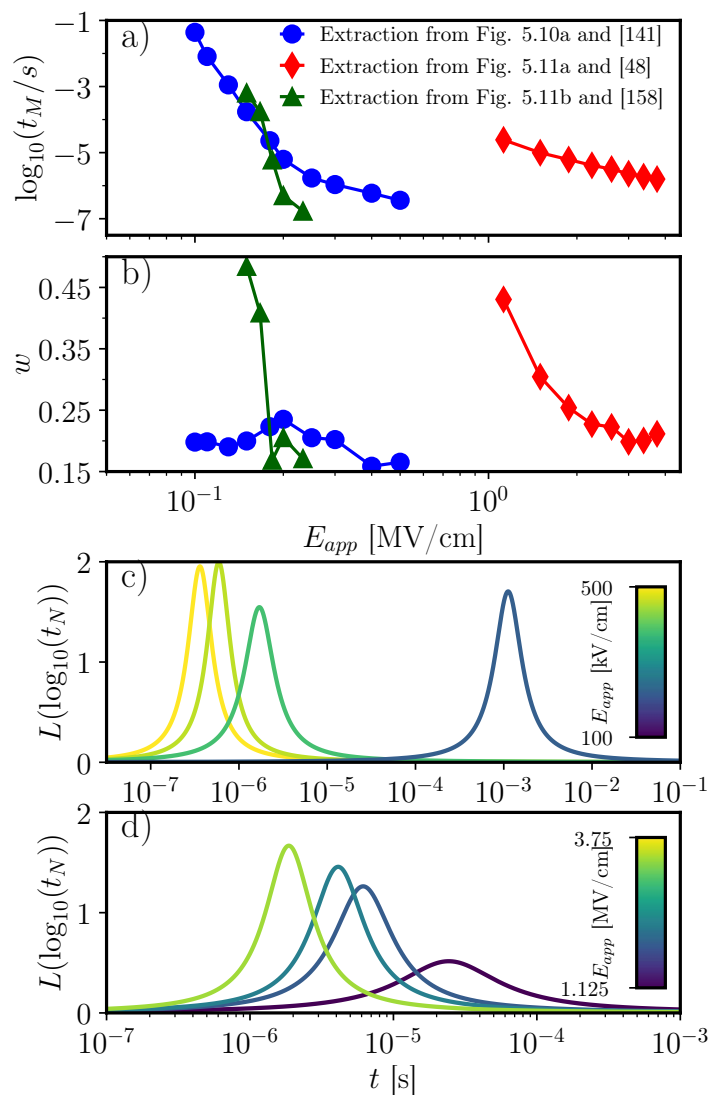
Figure 5.12: Parameters of Lorentzian distributions for the nucleation time t_N , as extracted from the calibration of the **ExtNucl** LGD model to experiments. a) $\log_{10}(t_M/s)$ versus E_{app}. b) The half width at half-maximum w of the Lorentzian distribution versus E_{app}. Corresponding Lorentzian distributions for nucleation times at different E_{app} for: c) epitaxial PZT thin-films [141] (see also Fig. 5.10a); d) poly-crystalline Si-doped HfO$_2$ [48] (see also Fig. 5.11a).

5.4   Chapter conclusions

Based on a systematic comparison between numerical simulations and $P - V$ and polarization reversal experiments for both poly-crystalline and epitaxial ferroelectrics, an updated version of the LGD model based on extrinsic nucleations has been proposed and implemented. The model shows an improved agreement with experiments compared to the conventional LGD model relying on intrinsic nucleations, and it can help put the device level modelling of ferroelectric materials and devices on a sounder physical basis. Considering that this analysis was aimed at studying the applicability of this new interpretation of the LGD framework, initially we deemed it reasonable to place the nucleation seed in the center of the simulated area, knowing that a possible future development in this respect may be precisely the effect of the location of the nucleation seed on the switching propagation.

Chapter 6

Conclusions and Future Outlooks

6.1 Summary of the PhD research

This thesis has dealt with several aspects related to the numerical modelling based on the Landau-Ginzburg-Devonshire framework for ferroelectric materials and devices, with perspective applications in neuromorphic computing. In particular, the theory and application of the PUND measurement technique in MFDM structures were revisited employing both analytical derivations and numerical simulations. In fact, the interplay between the depolarization field and charge trapping in MFDM stacks implies serious challenges for an accurate estimate of the polarization switched during the P or N pulse based on the measurement of terminal currents. By using numerical simulations, we explained and analyzed the discrepancies between the total switched charge in PUND measurements, Q_{PU}, and the switched polarization $P_{AV}^{(P)}$. We performed an analysis for various dielectric layer thicknesses t_D and trap densities at the FE-DE interface, thus offering insights into the compensation of ferroelectric polarization due to trapped charges and resulting depolarization field.

Within the limits of the proposed models, we analyzed the behaviour of physical quantities that are not directly detectable in experiments. While discrepancies between Q_{PU} and $P_{AV}^{(P)}$ could be attributed to errors in the PUND technique, it became evident that neither Q_{PU} nor $P_{AV}^{(P)}$ can provide an accurate estimate of the remanent polarization $2P_r$ of the underlying ferroelectric material, due to the depolarization field present even at zero external bias. The differences between these quantities were found to depend on the dielectric thickness t_D and trap density, which might introduce artifacts when characterizing the t_D dependence of ferroelectric properties in MFDM structures, thus sparking the interest for further research to enhance the

electrical probing of spontaneous polarization in ferroelectric-dielectric hetero-structures.

In addition to the extensive analysis of large–signal behavior in FTJs, our study included experimental characterization and numerical modeling of small–signal behavior. By linearizing the model used for large–signal simulations, a direct link was established between large and small-signal quantities in the simulation model.

This thesis also proposed a procedure for extracting material parameters for the Landau-Ginzburg-Devonshire model of antiferroelectric ZrO_2 films. Our approach is consistent with the microscopically non-polar nature of the zero–field state in antiferroelectric ZrO_2. By identifying specific points $(E_B, P_{T,B})$ and $(E_C, P_{T,C})$ in the $P_T - E_F$ curves, we proposed a simple procedure to extract the anisotropy coefficients used for the modeling of such materials. The methodology was demonstrated and validated through the analysis of quasi-static $P_T - E_F$ curves in various Metal-Antiferroelectric-Metal stacks. Moreover, the overall simulation framework was validated using antiferroelectric experimental data of $P_T - E_F$ in both quasi-static and transient NC regimes, revealing intriguing connections between NC operation in antiferroelectric and ferroelectric materials.

Lastly, based on a systematic comparison between numerical simulations and experiments involving $P - V$ and polarization reversal characteristics for both poly-crystalline and epitaxial ferroelectrics, a revised version of the Landau-Ginzburg-Devonshire model was introduced, incorporating extrinsic nucleations events into the simulation framework. This revised model could improve the agreement with experimental data compared to the conventional usage, which relies instead on intrinsic nucleation events.

6.2   Future Outlooks

The research conducted in this thesis has shed light on some aspects of ferroelectric and antiferroelectric materials and related electron devices, but new research directions could be explored.

One possible avenue for future research is the utilization of inelastic tunneling as a tool to describe charge trapping in ferroelectric and antiferroelectric materials. In fact, in this thesis only elastic tunneling processes have been explored as a mechanism for charge trapping. However, the physical picture behind tunneling and trapping is more comprehensive [159], and therefore the inclusion of inelastic tunneling mechanisms could bring an added value to the comparison with experiments. Moreover, while in this thesis the trans-

port through ferroelectric–dielectric stacks has been described in terms of tunneling, it is important to recognize the possible role played by alternative charge transport mechanisms in ferroelectric materials. Future research could explore the role of these mechanisms, such as the Poole-Frenkel effect [96], which describes an exponential increase in charge carrier mobility with the applied electric field and it is often observed in insulating materials with a relatively large density of defects. Investigating the Poole-Frenkel effect in ferroelectric materials can provide valuable insights into the role of defects in charge transport. Charge transport in ferroelectric materials may also occur as hopping mechanism [96], where carriers move between localized sites through discrete jumps.

The research developments outlined above can contribute to a better understanding of ferroelectric-based devices, which have several perspective applications, including memories as well as highly energy efficient artificial synapses and neurons for neuromorphic computing.

6. Conclusions and Future Outlooks

Appendix A

Non-homogenous polarization in MFDM stacks

The expression for the Gibbs' energy functional employed to describe the dynamics of the spontaneous polarization in an MFDM stack is derived by discretizing the ferroelectric material into n_D square domains that possess a fixed size d and are separated by a fixed domain wall width w [53]. The energy functional is composed by the electrostatic energy term, the domain wall energy term and the Landau free energy term.

The electrostatic energy U_{EL} for a non-homogeneous MFDM stack is expressed with the superposition of the effects produced by the domain-wise polarizations P_i as [53], [60]:

$$U_{EL} = \sum_{i=1}^{n_D} \left[\frac{1}{2} \int_{A_D} P_i V_D(\boldsymbol{r}) \, d\boldsymbol{r} \right] + \frac{V_T}{2} \int_A \varepsilon_0 \varepsilon_F E_{F,z}(\boldsymbol{r}, -t_F) d\boldsymbol{r} \ \ [\text{J}] \qquad (\text{A.1})$$

where $V_D(\boldsymbol{r})$ is the point potential in the ferroelectric-dielectric interface (i.e. $z = 0$, see Fig. 2.9 in the main text), ε_F is the background dielectric permittivity of the ferroelectric (see caption of Fig. 2.9 in the main text), $E_{F,z}(\boldsymbol{r}, -t_F)$ is the electric field component along the axis z at the interface between the ferroelectric material and the metal contact, n_D is the total number of domains and $A = n_D \cdot A_D$ is the total area of the device having n_D domains with area $A_D = d^2$. The battery energy term U_B is finally expressed as

$$U_B = -V_T \left[\sum_{i=1}^{n_D} [P_i \, A_D] + \int_A \varepsilon_0 \varepsilon_F E_{F,z}(\boldsymbol{r}) \, d\boldsymbol{r} \right] \ \ [\text{J}]. \qquad (\text{A.2})$$

The volume energy density related to the electrostatic and the battery term u_{ET} is obtained by summing the normalized quantities of Eq. (A.1) and

A. Non-homogenous polarization in MFDM stacks

Eq. (A.2):

$$\mathcal{U}_{ET} = \frac{1}{A} \left(\sum_{i=1}^{n_D} \left[\frac{P_i}{2} \int_{A_D} V_D(\boldsymbol{r}) \, d\boldsymbol{r} - A_D V_T P_i \right] - \frac{V_T}{2} \int_A \varepsilon_0 \varepsilon_F E_{F,z}(\boldsymbol{r}) \, d\boldsymbol{r} \right) \quad [\text{J/m}^2]$$

(A.3)

where in general, both $V_D(\boldsymbol{r})$ and $E_{F,z}(\boldsymbol{r})$ are the result of the superposition of the effects induced by the spontaneous polarizations P_i, the domain-wise trapped charge $Q_{S,j}$ and the external bias V_T. Moreover, $V_D(\boldsymbol{r})$ and $E_{F,z}(\boldsymbol{r})$ can be expressed in terms of appropriate Green's functions of the generic spontaneous polarization P_h and trapped charge $Q_{S,h}$ for the ferroelectric and dielectric materials, similarly to the derivations for the MFDM structure reported in Chapter 3.

Equation (A.3) can thus be rewritten as [53], [60]:

$$\mathcal{U}_{ET} = \frac{1}{2} \sum_{j,h} \frac{\widetilde{P}_j \widetilde{P}_h}{C_{j,h}} + \frac{C_F}{2 C_0} V_T \sum_j \widetilde{P}_j - V_T \sum_j P_j - \frac{V_T}{2} \sum_j \widetilde{P}_j B_j - \frac{n_D C_S V_T^2}{2}$$

(A.4)

where $\widetilde{P}_j = P_j + Q_{S,j}$ and the terms $C_{i,j}$ and B_j can be evaluated using the aforementioned Green's functions of the spontaneous polarization and trapped charge. In particular, the terms $C_{i,j}$ represent the capacitive coupling of the ferroelectric domains through the dielectric layer and are responsible for the depolarization energy [53].

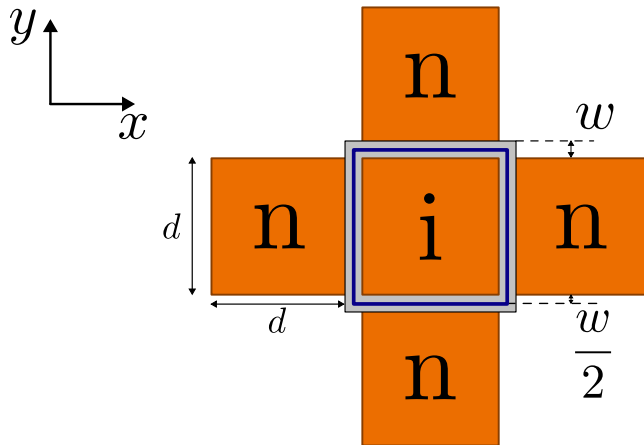The expression of the discretized domain wall energy term u_{DW} is

Figure A.1: Sketch of ferroelectric domains separated by a domain wall of fixed length w. Each domain is surrounded by a shell of size $w/2$; d is the domain size.

$$u_{DW} = k \sum_{i=1}^{n_D} \sum_{ni} \left(\frac{P_i - P_{ni}}{w} \right)^2 \qquad [\mathrm{J/m^3}] \qquad (A.5)$$

which will then be integrated over half the domain wall width $w/2$, the side d of the domain and the ferroelectric thickness t_F. The integrated expression can be then normalized by the area comprised by the square domain and its shell $(d+w)^2$ (see Fig. A.1), resulting in

$$\mathcal{U}_{DW} = \frac{1}{2} \frac{k}{w} \frac{d}{(d+w)^2} \sum_{i=1}^{n_D} \sum_{ni} (P_i - P_{ni})^2 \qquad [\mathrm{J/m^2}] \qquad (A.6)$$

The total Gibbs' free energy of the stack is therefore the sum of the Landau free energy term already discussed in Chapter 2, the electrostatic term in Eq. (A.3) and the domain wall energy term in Eq. (A.6)

$$\mathcal{U}_T = t_F \sum_{i=1}^{n_D} \left(\alpha_i P_i^2 + \beta_i P_i^4 + \gamma_i P_i^6 \right) + \mathcal{U}_{ET} + \mathcal{U}_{DW} \qquad [\mathrm{J/m^2}] \qquad (A.7)$$

In the context of the Landau-Khalatnikov equation (see Chapter 2), the dynamic equations for the domain-wise polarization in presence of trapped charge become [53], [160]:

$$t_F \rho \frac{\partial P_i}{\partial t} = - \frac{\partial \mathcal{U}_T}{\partial P_i} =$$

$$- \left(2\alpha_i P_i + 4\beta_i P_i^3 + 6\gamma_i P_i^5 \right) t_F +$$

$$- \left[t_F \frac{k}{w} \frac{d}{(d+w)^2} \sum_{ni} (P_i - P_{ni}) \right] +$$

$$- \left[\frac{1}{2} \sum_{j=1}^{n_D} \left[\frac{1}{C_{i,j}} + \frac{1}{C_{j,i}} \right] (P_j + Q_{S,j}) - \frac{V_T}{2} \left(B_i + 1 + \frac{C_D}{C_0} \right) \right]$$

(A.8)

which is reported in Section 2.4 of the main text.

A. Non-homogenous polarization in MFDM stacks

Appendix B

Green's function of a point charge in the MFDM stack
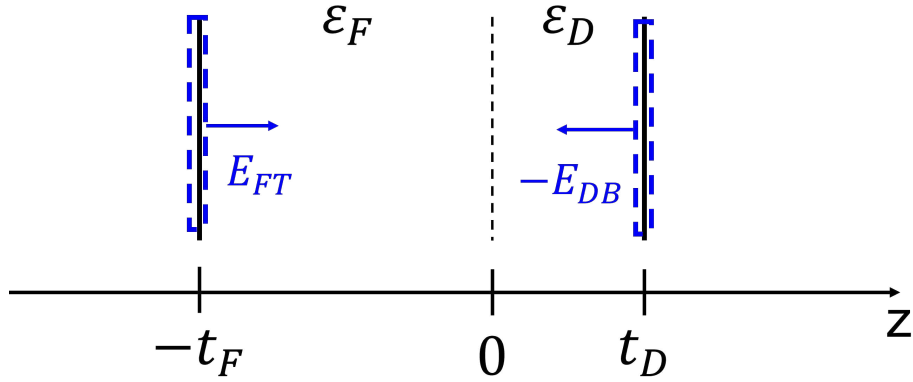
Figure B.1: Sketch of the MFDM stack, where E_{FT} and E_{DB} denote the z component of the electric field respectively at MF-FE interface and at MD-DE interface. (©2021 IEEE)

Here the analytical expression for the Green's function of the point charge defined in Eq. (3.9) are discussed. The potential $\psi(\mathbf{r}, z)$ produced by a point charge located in $(\mathbf{r}_0, z_0)$ in a dielectric material having a relative dielectric constant ε_r can be obtained by solving the Poisson equation [161]

$$\nabla^2 \psi(\mathbf{r}, z) = -\frac{e}{\varepsilon_0 \varepsilon_r} \delta(\mathbf{r} - \mathbf{r}_0)\delta(z - z_0). \tag{B.1}$$

where e is the elementary charge. By introducing the 2D Fourier transform of $\psi(\mathbf{r}, z)$ with respect to the coordinates $\boldsymbol{r}=(x,y)$, and defining the Fourier

B. Green's function of a point charge in the MFDM stack

pair it is possible to write

$$\psi(\mathbf{r}, z) \approx \int_{\mathbf{q}} \psi(\mathbf{q}, z) \exp\left(-i\,\mathbf{q}\cdot\mathbf{r}\right) d\mathbf{q}$$

$$\psi(\mathbf{q}, z) \approx \frac{1}{(2\pi)^2} \int_A \psi(\mathbf{r}, z) \exp\left(i\,\mathbf{q}\cdot\mathbf{r}\right) d\mathbf{r} \;. \tag{B.2}$$

Equation (B.2) assumes that the device area A is large enough that the integral over A is a good approximation of the indefinite integral over the entire (x,y) plane. [1].

Recalling the identity

$$\delta(\mathbf{r} - \mathbf{r}_0) \approx \frac{1}{(2\pi)^2} \int_{\mathbf{q}} \exp\left[-i\,\mathbf{q}\cdot(\mathbf{r} - \mathbf{r}_0)\right] d\mathbf{q} \tag{B.3}$$

and substituting Equations (B.2) and (B.3) into Eq. (B.1), it is readily evident that the unknown potential $\Psi(\mathbf{q}, z)$ takes the form [161]

$$\psi(\mathbf{q}, z) = \frac{\exp\left(i\,\mathbf{q}\cdot\mathbf{r}_0\right)}{(2\pi)^2} \phi(q, z) \tag{B.4}$$

where $\phi(q, z)$ must satisfy the differential equation

$$\left[\frac{\partial^2}{\partial z^2} - q^2\right]\phi = -\frac{e}{\varepsilon_0\varepsilon_r}\,\delta(z - z_0) \tag{B.5}$$

Assuming that the point charge is located at $z_0 = 0$, namely at the FE-DE interface (see Figure B.1), the potential $\phi_F(q, z)$ in the ferroelectric and $\phi_D(q, z)$ in the dielectric region can be written as

$$\phi_F(z) = C_1 \exp\left(q\,z\right) + C_2 \exp\left(-q\,z\right) \qquad z < 0 \tag{B.6a}$$

$$\phi_D(z) = C_3 \exp\left(q\,z\right) + C_4 \exp\left(-q\,z\right) \qquad z > 0 \tag{B.6b}$$

where the four q dependent constants C_1, C_2, C_3 and C_4 can be determined by using appropriate boundary conditions. At the interface with metal electrodes it was assumed $\phi_F(-t_F) = 0$, $\phi_D(t_D) = 0$, whereas at the FE-DE interface the conditions $\phi_F(0) = \phi_D(0)$ and $[\varepsilon_0\varepsilon_F(\partial\phi_F(0)/\partial z) - \varepsilon_0\varepsilon_D(\partial\phi_D(0)/\partial z)] = e$ were imposed. This results in

$$\phi_F(z) = C_{Fe}\left\{\exp\left(q\,z\right) - \exp\left[-q\left(z + 2\,t_F\right)\right]\right\} \quad z < 0 \tag{B.7a}$$

$$\phi_D(z) = C_{De}\left\{\exp\left(q\,z\right) - \exp\left[-q\left(z - 2\,t_D\right)\right]\right\} \quad z > 0 \tag{B.7b}$$

---

[1]The formalism may be rephrased in terms of a Fourier series by assuming periodic boundary conditions for $\psi(\mathbf{r}, z)$ at the edges of the area A, that would however lead to identical results [161]

with

$$C_F = \frac{1 - e_D}{\varepsilon_F \left(1 + e_F\right)\left(1 - e_D\right) - \varepsilon_D \left(1 - e_F\right)\left(1 + e_D\right)} \cdot \frac{e}{q} \qquad \text{(B.8a)}$$

$$C_D = \frac{1 - e_F}{1 - e_D} \cdot C_F \qquad \text{(B.8b)}$$

where the more compact notation $e_F = \exp\left(-2\,q\,t_F\right)$ and $e_D = \exp\left(2\,q\,t_D\right)$ is introduced. The Green's function $G_{MF}(\mathbf{r}_0, z_0)$ to determine is defined as

$$G_{MF}(\mathbf{r}_0, z_0) = \frac{\varepsilon_0 \varepsilon_F}{e} \int\limits_A E_{FT}(\mathbf{r})\, d\mathbf{r} \qquad \text{(B.9)}$$

where $E_{FT}(\mathbf{r})$ denotes the z component of the electric field at the MF-FE interface (i.e. at $z=-t_F$) produced by a point charge e located at $(\mathbf{r}_0, z_0)$. Recalling the definition of the Fourier transform pairs in Eq. (B.2) and then using Eq. (B.4)

$$\int\limits_A E_{FT}(\mathbf{r})\, d\mathbf{r} = (2\pi)^2 \lim_{q \to 0} E_{FT}(\mathbf{q}) =$$

$$= -\,(2\pi)^2 \lim_{q \to 0} \frac{\partial \psi(\mathbf{q}, z_0)}{\partial z} = \qquad \text{(B.10)}$$

$$= -\lim_{q \to 0} \frac{\partial \phi_F(\mathbf{q}, z_0)}{\partial z}$$

then Eqs. (B.9) and (B.10) finally provide

$$G_{MF}(\mathbf{r}_0, z_0) = -\frac{\varepsilon_0 \varepsilon_F}{e} \lim_{q \to 0} \frac{\partial \phi_F(\mathbf{q}, z_0)}{\partial z} \ . \qquad \text{(B.11)}$$

For $z_0 = -t_F$ the limit in Eq. (B.11) can be readily calculated by using Eqs. (B.7a) and (B.8a), so as to obtain

$$G_{MF}(\mathbf{r}_0, 0) = -\frac{C_F}{C_F + C_D} \qquad \text{(B.12)}$$

The corresponding Green's function G_{MD} at the MD electrode, defined in Eq. (B.20), can be derived with an entirely similar procedure. The result is

$$G_{MD}(\mathbf{r}_0, 0) = -\frac{\varepsilon_0 \varepsilon_D}{e} \lim_{q \to 0} \frac{\partial \phi_D(\mathbf{q}, t_D)}{\partial z} = -\frac{C_D}{C_F + C_D} \qquad \text{(B.13)}$$

so that $(G_{MF}(\mathbf{r}_0, 0) + G_{MD}(\mathbf{r}_0, 0)) = -1$.

B. Green's function of a point charge in the MFDM stack

Similar derivations apply to the case of a point charge located in the ferroelectric (i.e. for $-t_F < z_0 < 0$) or in the dielectric (i.e. for $0 < z_0 < t_d$). In the former case the result is

$$G_{MF}(\mathbf{r}_0, z_0) = -\frac{C_F + C_D\dfrac{|z_0|}{t_F}}{C_F + C_D} \tag{B.14}$$

$$G_{MD}(\mathbf{r}_0, z_0) = -\frac{C_D\left(1 - \dfrac{|z_0|}{t_F}\right)}{C_F + C_D} \tag{B.15}$$

whereas for the latter case

$$G_{MF}(\mathbf{r}_0, z_0) = -\frac{C_F\left(1 - \dfrac{z_0}{t_D}\right)}{C_F + C_D} \tag{B.16}$$

$$G_{MD}(\mathbf{r}_0, z_0) = -\frac{C_D + C_F\dfrac{z_0}{t_D}}{C_F + C_D}. \tag{B.17}$$

As it can be seen, even for an $z_0 \neq 0$ the result $[G_{MF}(\mathbf{r}_0, z_0) + G_{MD}(\mathbf{r}_0, z_0)] = -1$ still holds.

B.1 Charge and current at the MD electrode

The analysis of PUND measurements presented in the main paper is based on the current I_{MF} at the MF electrode. According to the I_{MF}, I_{MD} definitions sketched in Figure 3.1, it is evident that I_{MD} must be equal to I_{MF}. For the completeness of definitions and derivations, here is reported a concise analysis about the charge Q_{MD} and current I_{MD} at the MD electrode. Starting with Q_{MD} written as (see Fig. B.1)

$$Q_{MD}(t) = \frac{1}{A}\int_A -\varepsilon_0\varepsilon_D E_{DB}(\mathbf{r}, t)\, d\mathbf{r} = -\varepsilon_0\varepsilon_D E_{DB,AV}(t) \tag{B.18}$$

where $E_{DB}(\mathbf{r}, t)$ is the z component of the field at the DE-MD interface at $z = t_D$, the term $\varepsilon_0\varepsilon_D E_{DB}(\mathbf{r})$ can be expressed as

$$\varepsilon_0\varepsilon_D E_{DB}(\mathbf{r}) = C_S V_T + \varepsilon_0\varepsilon_D E_{DI}(\mathbf{r}) \tag{B.19}$$

where $E_{DI}(\mathbf{r})$ is the contribution to the field due to the total charge $[P(\mathbf{r}_0) + Q_S(\mathbf{r}_0)]$ at the FE-DE interface. As already discussed in Section 3.3.1 of the main text, here trapping is assumed to be dominated by interface traps at the FE-DE interface.

The Green's function $G_{MD}(\mathbf{r}_0, z_0)$ at the MD electrode can be defined as

$$G_{MD}(\mathbf{r}_0, z_0) = \frac{\varepsilon_0 \varepsilon_D}{e} \int_A -E_{DB}(\mathbf{r}, \mathbf{r}_0 z_0) \, d\mathbf{r} \qquad (B.20)$$

that allows to write the average $E_{DI,AV}$ as

$$\varepsilon_0 \varepsilon_D E_{DI,AV} = -\frac{1}{A} \int_A [P(\mathbf{r}_0) + Q_S(\mathbf{r}_0)] \, G_{MD}(\mathbf{r}_0, z_0) \, d\mathbf{r}_0 \qquad (B.21)$$

For a charge at the FE-DE interface $G_{MD}(\mathbf{r}_0, 0) \simeq -C_D/C_0$ and thus

$$\varepsilon_0 \varepsilon_D E_{DI,AV} \simeq \frac{C_D}{C_0} (P_{AV} + Q_{S,AV}) \qquad (B.22)$$

so that $Q_{MD}(t)$ in Eq. (B.18) becomes

$$Q_{MD}(t) = -C_S V_T(t) - \varepsilon_0 \varepsilon_D E_{DI,AV}(t). \qquad (B.23)$$

By using similar assumptions as those embraced in Section 3.3.1, I_{MD} can be written as

$$\begin{aligned}
I_{MD} &= -\frac{\partial Q_{MD}}{\partial t} + I_{QS,MD} + I_{lkg} = \\[6pt]
&= C_S \frac{\partial V_T}{\partial t} + \varepsilon_0 \varepsilon_D \frac{\partial E_{DI,AV}}{\partial t} + \\[6pt]
&\quad + I_{QS,MD} + I_{lkg} = \\[6pt]
&= C_S \frac{\partial V_T}{\partial t} + \frac{C_D}{C_0} \frac{\partial P_{AV}}{\partial t} + \frac{C_D}{C_0} \frac{\partial Q_{S,AV}}{\partial t} + \\[6pt]
&\quad + I_{QS,MD} + I_{lkg}
\end{aligned} \qquad (B.24)$$

where in the last equality we have used Eq. (B.22). By recalling the I_{MF} expression in Eq. (3.11) and the relation $[I_{QS,MF} - I_{QS,MD}] = \partial Q_{S,AV}/\partial t$, it is immediate to obtain $(I_{MF} - I_{MD}) = 0$, thus confirming that I_{MD} is equal to I_{MF}.

B. Green's function of a point charge in the MFDM stack

Appendix C

Maximum and minimum of the static $E_{FE} - P_T$ relation for the antiferroelectric ZrO$_2$

To show that the maximum and minimum of the static $E_{FE} - P_T$ curve coincide with those of the $E_{FE} - P$ curve, it is possible to substitute $P = P_T - \varepsilon_0\varepsilon_F E_{FE}$ in Eq. (4.2a) and obtain

$$E_{FE} = 2\alpha\left(P_T - \varepsilon_0\varepsilon_F E_{FE}\right) + +4\beta\left(P_T - \varepsilon_0\varepsilon_F E_{FE}\right)^3 + $$
$$+6\gamma\left(P_T - \varepsilon_0\varepsilon_F E_{FE}\right)^5 \tag{C.1}$$

Then, deriving both sides of Eq. (C.1) with respect to P_T results in

$$\frac{\partial E_{FE}}{\partial P_T} = 2\alpha\left(1 - \varepsilon_0\varepsilon_F E_{FE}\frac{\partial E_{FE}}{\partial P_T}\right) + $$
$$+12\beta\underbrace{\left(P_T - \varepsilon_0\varepsilon_F E_{FE}\right)^2}_{P^2}\left(1 - \varepsilon_0\varepsilon_F E_{FE}\frac{\partial E_{FE}}{\partial P_T}\right) \tag{C.2}$$
$$+30\gamma\underbrace{\left(P_T - \varepsilon_0\varepsilon_F E_{FE}\right)^4}_{P^4}\left(1 - \varepsilon_0\varepsilon_F E_{FE}\frac{\partial E_{FE}}{\partial P_T}\right)$$

which can be refactored in

$$\frac{\partial E_{FE}}{\partial P_T}\left[1 + \varepsilon_0\varepsilon_F(2\alpha + 12\beta P^2 + 30\gamma P^4)\right] = $$
$$= 2\alpha + 12\beta P^2 + 30\gamma P^4 \tag{C.3}$$

C. Maximum and minimum of the static $E_{FE} - P_T$ relation for the antiferroelectric ZrO₂

Equation (C.3) clearly shows that the condition

$$\frac{\partial E_{FE}}{\partial P} = 2\alpha + 12\beta P^2 + 30\gamma P^4 = 0 \tag{C.4}$$

implies also $(\partial E_{FE}/\partial P_T) = 0$.

List of Publications

Journal Articles

- R. Fontanini, **M. Segatto**, M. Massarotto, R. Specogna, F. Driussi, M. Loghi, and D. Esseni, "Modeling and design of ftjs as multi-level low energy memristors for neuromorphic computing," *IEEE Journal of the Electron Devices Society*, vol. 9, pp. 1202–1209, 2021. DOI: `10.1109/JEDS.2021.3120200`.

- R. Fontanini, J. Barbot, **M. Segatto**, *et al.*, "Interplay between charge trapping and polarization switching in beol-compatible bilayer ferroelectric tunnel junctions," *IEEE Journal of the Electron Devices Society*, vol. 10, pp. 593–599, 2022. DOI: `10.1109/JEDS.2022.3171217`.

- R. Fontanini, **M. Segatto**, K. S. Nair, M. Holzer, F. Driussi, I. Häusler, C. T. Koch, C. Dubourdieu, V. Deshpande, and D. Esseni, "Charge-Trapping-Induced Compensation of the Ferroelectric Polarization in FTJs: Optimal Conditions for a Synaptic Device Operation," *IEEE Transactions on Electron Devices*, vol. 69, no. 7, pp. 3694–3699, 2022. DOI: `10.1109/TED.2022.3175684`.

- M. Hoffmann, M. Gui, S. Slesazeck, R. Fontanini, **M. Segatto**, D. Esseni, and T. Mikolajick, "Intrinsic nature of negative capacitance in multidomain $Hf_{0.5}Zr_{0.5}O_2$-based ferroelectric/dielectric heterostructures," *Advanced Functional Materials*, vol. 32, no. 2, p. 2 108 494, 2022. DOI: `https://doi.org/10.1002/adfm.202108494`.

- **M. Segatto**, R. Fontanini, F. Driussi, D. Lizzit, and D. Esseni, "Limitations to Electrical Probing of Spontaneous Polarization in Ferroelectric-Dielectric Heterostructures," *IEEE Journal of the Electron Devices Society*, vol. 10, pp. 324–333, 2022. DOI: `10.1109/JEDS.2022.3164652`.

- **M. Segatto**, F. Rupil, and D. Esseni, "Analytical procedure for the extraction of material parameters in antiferroelectric zro2," *IEEE Transactions on Electron Devices*, vol. 70, no. 6, pp. 3037–3042, 2023. DOI: `10.1109/TED.2023.3265626`.

Conference Proceedings

- R. Fontanini, J. Barbot, **M. Segatto**, *et al.*, "Polarization switching and interface charges in beol compatible ferroelectric tunnel junctions," in *ESSDERC 2021 - IEEE 51st European Solid-State Device Research Conference (ESSDERC)*, 2021, pp. 255–258. DOI: 10.1109/ESSDERC53440.2021.9631812.

- **M. Segatto**, M. Massarotto, S. Lancaster, *et al.*, "Polarization switching and ac small-signal capacitance in ferroelectric tunnel junctions," in *ESSDERC 2022 - IEEE 52nd European Solid-State Device Research Conference (ESSDERC)*, 2022, pp. 340–343. DOI: 10.1109/ESSDERC55479.2022.9947185.

- S. Lancaster, **M. Segatto**, C. Silva, B. Max, T. Mikolajick, D. Esseni, F. Driussi, and S. Slesazeck, "Reducing the tunneling barrier thickness of bilayer ferroelectric tunnel junctions with metallic electrodes," in *2023 Device Research Conference (DRC)*, 2023, pp. 1–2. DOI: 10.1109/DRC58590.2023.10187018.

- M. Massarotto, **M. Segatto**, F. Driussi, A. Affanni, S. Lancaster, S. Slesazeck, T. Mikolajick, and D. Esseni, "Bridging large-signal and small-signal responses of hafnium-based ferroelectric tunnel junctions," in *2023 35th International Conference on Microelectronic Test Structure (ICMTS)*, 2023, pp. 1–6. DOI: 10.1109/ICMTS55420.2023.10094178.

Bibliography

1 S. Slesazeck and T. Mikolajick, "Nanoscale resistive switching memory devices: A review," *Nanotechnology*, vol. 30, no. 35, p. 352 003, 2019. DOI: `10.1088/1361-6528/ab2084`.

2 F. Emmert-Streib, Z. Yang, H. Feng, S. Tripathi, and M. Dehmer, "An introductory review of deep learning for prediction models with big data," *Frontiers in Artificial Intelligence*, vol. 3, 2020. DOI: `10.3389/frai.2020.00004`.

3 M. Horowitz, "1.1 computing's energy problem (and what we can do about it)," in *2014 IEEE International Solid-State Circuits Conference Digest of Technical Papers (ISSCC)*, 2014, pp. 10–14. DOI: `10.1109/ISSCC.2014.6757323`.

4 H. Bao, H. Zhou, J. Li, *et al.*, "Toward memristive in-memory computing: Principles and applications," *Frontiers of Optoelectronics*, vol. 15, no. 1, p. 23, May 2022. DOI: `10.1007/s12200-022-00025-4`.

5 W. Wang, W. Song, P. Yao, Y. Li, J. Van Nostrand, Q. Qiu, D. Ielmini, and J. J. Yang, "Integration and co-design of memristive devices and algorithms for artificial intelligence," *iScience*, vol. 23, no. 12, p. 101 809, 2020. DOI: `https://doi.org/10.1016/j.isci.2020.101809`.

6 J. Hutchby, "The nanoelectronics roadmap," in *Emerging Nanoelectronic Devices*. John Wiley & Sons, Ltd, 2014, ch. 1, pp. 1–14. DOI: `https://doi.org/10.1002/9781118958254.ch01`.

7 L. Chua, "Memristor-the missing circuit element," *IEEE Transactions on Circuit Theory*, vol. 18, no. 5, pp. 507–519, 1971. DOI: `10.1109/TCT.1971.1083337`.

8 D. B. Strukov, G. S. Snider, D. R. Stewart, and R. S. Williams, "The missing memristor found," *Nature*, vol. 453, no. 7191, pp. 80–83, May 2008. DOI: `10.1038/nature06932`.

9   G. Lee, J.-H. Baek, F. Ren, S. J. Pearton, G.-H. Lee, and J. Kim, "Artificial neuron and synapse devices based on 2d materials," *Small*, vol. 17, no. 20, p. 2 100 640, 2021. DOI: `https://doi.org/10.1002/smll.202100640`.

10   L. F. Abbott and S. B. Nelson, "Synaptic plasticity: Taming the beast," *Nature Neuroscience*, vol. 3, no. 11, pp. 1178–1183, Nov. 2000. DOI: `10.1038/81453`.

11   R. A. Nicoll, "A brief history of long-term potentiation," *Neuron*, vol. 93, no. 2, pp. 281–290, 2017. DOI: `https://doi.org/10.1016/j.neuron.2016.12.015`.

12   N. Deperrois and M. Graupner, "Short-term depression and long-term plasticity together tune sensitive range of synaptic plasticity," en, *PLoS Comput Biol*, vol. 16, no. 9, e1008265, Sep. 2020.

13   W. Chen, L. Song, S. Wang, Z. Zhang, G. Wang, G. Hu, and S. Gao, "Essential characteristics of memristors for neuromorphic computing," *Advanced Electronic Materials*, vol. 9, no. 2, p. 2 200 833, 2023. DOI: `https://doi.org/10.1002/aelm.202200833`.

14   K. Kinoshita, T. Tamura, M. Aoki, Y. Sugiyama, and H. Tanaka, "Bias polarity dependent data retention of resistive random access memory consisting of binary transition metal oxide," *Applied Physics Letters*, vol. 89, no. 10, p. 103 509, Sep. 2006. DOI: `10.1063/1.2339032`.

15   D. V. Christensen, R. Dittmann, B. Linares-Barranco, *et al.*, "2022 roadmap on neuromorphic computing and engineering," *Neuromorphic Computing and Engineering*, vol. 2, no. 2, p. 022 501, May 2022. DOI: `10.1088/2634-4386/ac4a83`.

16   M. Zhao, B. Gao, J. Tang, H. Qian, and H. Wu, "Reliability of analog resistive switching memory for neuromorphic computing," *Applied Physics Reviews*, vol. 7, no. 1, p. 011 301, Jan. 2020. DOI: `10.1063/1.5124915`.

17   C. Bengel, A. Siemon, F. Cüppers, S. Hoffmann-Eifert, A. Hardtdegen, M. von Witzleben, L. Hellmich, R. Waser, and S. Menzel, "Variability-aware modeling of filamentary oxide-based bipolar resistive switching cells using spice level compact models," *IEEE Transactions on Circuits and Systems I: Regular Papers*, vol. 67, no. 12, pp. 4618–4630, 2020. DOI: `10.1109/TCSI.2020.3018502`.

18   R. Matos and N. Pala, "A review of phase-change materials and their potential for reconfigurable intelligent surfaces," *Micromachines*, vol. 14, no. 6, 2023. DOI: `10.3390/mi14061259`.

19 V. Joshi, M. Le Gallo, S. Haefeli, I. Boybat, S. R. Nandakumar, C. Piveteau, M. Dazzi, B. Rajendran, A. Sebastian, and E. Eleftheriou, "Accurate deep neural network inference using computational phase-change memory," *Nature Communications*, vol. 11, no. 1, p. 2473, May 2020. DOI: `10.1038/s41467-020-16108-9`.

20 M. Boniardi, D. Ielmini, S. Lavizzari, A. L. Lacaita, A. Redaelli, and A. Pirovano, "Statistics of resistance drift due to structural relaxation in phase-change memory arrays," *IEEE Transactions on Electron Devices*, vol. 57, no. 10, pp. 2690–2696, 2010. DOI: `10.1109/TED.2010.2058771`.

21 S. R. Nandakumar, M. Le Gallo, C. Piveteau, *et al.*, "Mixed-precision deep learning based on computational memory," *Frontiers in Neuroscience*, vol. 14, 2020. DOI: `10.3389/fnins.2020.00406`.

22 a. L. Esaki, R. Laibowitz, and P. Stiles, "Polar switch," *IBM Tech. Discl. Bull*, vol. 13, no. 2161, p. 114, 1971.

23 T. Shimizu, K. Katayama, T. Kiguchi, A. Akama, T. J. Konno, O. Sakata, and H. Funakubo, "The demonstration of significant ferroelectricity in epitaxial Y-doped HfO_2 film," *Nature, Scientific Reports*, vol. 6, no. 32931, Sep. 2016. DOI: `10.1038/srep32931`.

24 S. S. Cheema, D. Kwon, N. Shanker, *et al.*, "Enhanced ferroelectricity in ultrathin films grown directly on silicon," *Nature*, vol. 580, no. 7804, pp. 478–482, Apr. 2020. DOI: `10.1038/s41586-020-2208-x`.

25 K. Hagiwara, K. N. Byun, S. Morita, E. Yamamoto, M. Kobayashi, X. Liu, and M. Osada, "Molecularly thin batio3 nanosheets with stable ferroelectric response," *Advanced Electronic Materials*, vol. 9, no. 4, p. 2 201 239, 2023. DOI: `https://doi.org/10.1002/aelm.202201239`.

26 M. Kobayashi, Y. Tagawa, F. Mo, T. Saraya, and T. Hiramoto, "Ferroelectric hfo2 tunnel junction memory with high ter and multi-level operation featuring metal replacement process," *IEEE Journal of the Electron Devices Society*, vol. 7, pp. 134–139, 2019. DOI: `10.1109/JEDS.2018.2885932`.

27 Y.-C. Luo, J. Hur, P. Wang, A. I. Khan, and S. Yu, "Modeling multistates in ferroelectric tunnel junction," in *2020 Device Research Conference (DRC)*, 2020, pp. 1–2. DOI: `10.1109/DRC50226.2020.9135154`.

28 N. Feng, H. Li, L. Zhang, *et al.*, "A physics-based dynamic compact model of ferroelectric tunnel junctions," *IEEE Electron Device Letters*, vol. 44, no. 2, pp. 261–264, 2023. DOI: `10.1109/LED.2022.3233456`.

29   S. Beyer, S. Dünkel, M. Trentzsch, *et al.*, "Fefet: A versatile cmos compatible device with game-changing potential," in *2020 IEEE International Memory Workshop (IMW)*, 2020, pp. 1–4. DOI: `10.1109/IMW48823.2020.9108150`.

30   S. Yu, *Semiconductor Memory Devices and Circuits*. CRC Press, Apr. 2022.

31   B. I. Kidyarov and V. V. Atuchin, "Universal crystal classification system "point symmetry–physical property"," *Ferroelectrics*, vol. 360, no. 1, pp. 96–99, 2007. DOI: `10.1080/00150190701516244`.

32   J. Valasek, "Piezo-electric activity of rochelle salt under various conditions," *Phys. Rev.*, vol. 19, pp. 478–491, 5 May 1922. DOI: `10.1103/PhysRev.19.478`.

33   V. Ginzburg, "On the dielectric properties of ferroelectric (seignetteelectric) crystals and barium titanate," *Zh. eksp. teor. Fiz*, vol. 15, p. 739, 1945.

34   A. Devonshire, "Theory of ferroelectrics," *Advances in Physics*, vol. 3, no. 10, pp. 85–130, 1954. DOI: `10.1080/00018735400101173`.

35   L. E. Cross, "Vii. a thermodynamic treatment of ferroelectricity and antiferroelectricity in pseudo-cubic dielectrics," *The Philosophical Magazine: A Journal of Theoretical Experimental and Applied Physics*, vol. 1, no. 1, pp. 76–92, 1956. DOI: `10.1080/14786435608238078`.

36   J. F. Ihlefeld, "Chapter 1 - fundamentals of ferroelectric and piezoelectric properties," in *Ferroelectricity in Doped Hafnium Oxide: Materials, Properties and Devices*, ser. Woodhead Publishing Series in Electronic and Optical Materials, U. Schroeder, C. S. Hwang, and H. Funakubo, Eds., Woodhead Publishing, 2019, pp. 1–24. DOI: `https://doi.org/10.1016/B978-0-08-102430-0.00001-2`.

37   T. S. Böscke, J. Müller, D. Bräuhaus, U. Schröder, and U. Böttger, "Ferroelectricity in hafnium oxide thin films," *Applied Physics Letters*, vol. 99, no. 10, p. 102 903, 2011. DOI: `10.1063/1.3634052`.

38   K. M. Rabe, M. Dawber, C. Lichtensteiger, C. Ahn, and J. Triscone, *Physiscs of Ferroelectrics, a Modern Perspective*. Springer, 2007.

39   D. Meier and S. M. Selbach, "Ferroelectric domain walls for nanotechnology," *Nature Reviews Materials*, vol. 7, no. 3, pp. 157–173, Mar. 2022. DOI: `10.1038/s41578-021-00375-z`.

40 A. K. Saha, K. Ni, S. Dutta, S. Datta, and S. Gupta, "Phase field modeling of domain dynamics and polarization accumulation in ferroelectric hzo," *Applied Physics Letters*, vol. 114, no. 20, p. 202 903, 2019. DOI: `10.1063/1.5092707`.

41 C. T. Black, C. Farrell, and T. J. Licata, "Suppression of ferroelectric polarization by an adjustable depolarization field," *Applied Physics Letters*, vol. 71, no. 14, pp. 2041–2043, Oct. 1997. DOI: `10.1063/1.119781`.

42 N. W. Ashcroft and N. D. Mermin, *Solid state physics.* New York, NY: Holt, Rinehart and Winston, 1976.

43 M. Materano, P. D. Lomenzo, H. Mulaosmanovic, M. Hoffmann, A. Toriumi, T. Mikolajick, and U. Schroeder, "Polarization switching in thin doped HfO2 ferroelectric layers," *Applied Physics Letters*, vol. 117, no. 26, p. 262 904, Dec. 2020. DOI: `10.1063/5.0035100`.

44 Y. Ishibashi and Y. Takagi, "Note on ferroelectric domain switching," *Journal of the Physical Society of Japan*, vol. 31, no. 2, pp. 506–510, 1971. DOI: `10.1143/JPSJ.31.506`.

45 P. Buragohain, C. Richter, T. Schenk, H. Lu, T. Mikolajick, U. Schroeder, and A. Gruverman, "Nanoscopic studies of domain structure dynamics in ferroelectric La:HfO2 capacitors," *Applied Physics Letters*, vol. 112, no. 22, p. 222 901, May 2018. DOI: `10.1063/1.5030562`.

46 T.-H. Ryu, D.-H. Min, and S.-M. Yoon, "Comparative studies on ferroelectric switching kinetics of sputtered Hf0.5Zr0.5O2 thin films with variations in film thickness and crystallinity," *Journal of Applied Physics*, vol. 128, no. 7, p. 074 102, Aug. 2020. DOI: `10.1063/5.0013487`.

47 A. K. Tagantsev, I. Stolichnov, N. Setter, J. S. Cross, and M. Tsukada, "Non-kolmogorov-avrami switching kinetics in ferroelectric thin films," *Phys. Rev. B*, vol. 66, p. 214 109, 21 2002. DOI: `10.1103/PhysRevB.66.214109`.

48 K. Lee, H.-J. Lee, T. Y. Lee, *et al.*, "Stable subloop behavior in ferroelectric si-doped hfo2," *ACS Applied Materials & Interfaces*, vol. 11, no. 42, pp. 38 929–38 936, 2019, PMID: 31576734. DOI: `10.1021/acsami.9b12878`.

49 P. Buragohain, A. Erickson, T. Mimura, T. Shimizu, H. Funakubo, and A. Gruverman, "Effect of film microstructure on domain nucleation and intrinsic switching in ferroelectric y:hfo2 thin film capacitors," *Advanced Functional Materials*, vol. 32, no. 9, p. 2 108 876, 2022. DOI: `https://doi.org/10.1002/adfm.202108876`.

50 L. D. Landau and I. Khalatnikov, "On the anomalous absorption of sound near a second order phase transition point," *Dokl. Akad. Nauk*, vol. 96, pp. 469–472, 1954.

51 A. K. Saha, M. Si, P. D. Ye, and S. K. Gupta, "Polarization switching in hf0.5zr0.5o2-dielectric stack: The role of dielectric layer thickness," *Applied Physics Letters*, vol. 119, no. 12, p. 122 903, 2021. DOI: `10.1063/5.0056448`.

52 M. Hoffmann, M. Gui, S. Slesazeck, R. Fontanini, M. Segatto, D. Esseni, and T. Mikolajick, "Intrinsic nature of negative capacitance in multidomain $Hf_{0.5}Zr_{0.5}O_2$-based ferroelectric/dielectric heterostructures," *Advanced Functional Materials*, vol. 32, no. 2, p. 2 108 494, 2022. DOI: `https://doi.org/10.1002/adfm.202108494`.

53 T. Rollo, F. Blanchini, G. Giordano, R. Specogna, and D. Esseni, "Stabilization of negative capacitance in ferroelectric capacitors with and without a metal interlayer," *Nanoscale*, vol. 12, pp. 6121–6129, 23 2020. DOI: `10.1039/c9nr09470a`.

54 M. Hoffmann, B. Max, T. Mittmann, U. Schroeder, S. Slesazeck, and T. Mikolajick, "Demonstration of High-speed Hysteresis-free Negative Capacitance in Ferroelectric $Hf_{0.5}Zr_{0.5}O_2$," in *2018 IEEE International Electron Devices Meeting (IEDM)*, Dec. 2018, pp. 31.6.1–31.6.4. DOI: `10.1109/IEDM.2018.8614677`.

55 M. Hoffmann, F. P. G. Fengler, M. Herzig, T. Mittmann, B. Max, U. Schroeder, R. Negrea, P. Lucian, S. Slesazeck, and T. Mikolajick, "Unveiling the double-well energy landscape in a ferroelectric layer," *Nature*, vol. 565, pp. 464–467, 2019. DOI: `10.1038/s41586-018-0854-z`.

56 "Front matter," in *Advanced Engineering Thermodynamics*. John Wiley and Sons, Ltd, 2016, pp. i–xxxviii. DOI: `https://doi.org/10.1002/9781119245964.fmatter`.

57 M. J. Moran and H. N. Shapiro, *Fundamentals of engineering thermodynamics*, 6th ed. John Wiley and Sons Inc., New York, NY, 2009.

58 K. Majumdar, S. Datta, and S. P. Rao, "Revisiting the Theory of Ferroelectric Negative Capacitance," *IEEE Transactions on Electron Devices*, vol. 63, no. 5, pp. 2043–2049, May 2016. DOI: `10.1109/TED.2016.2544813`.

59 Y. Kim, Y. Cho, S. Hong, S. Bühlmann, H. Park, D.-K. Min, S.-H. Kim, and K. No, "Correlation between grain size and domain size distributions in ferroelectric media for probe storage applications," *Applied Physics Letters*, vol. 89, no. 16, p. 162 907, Oct. 2006. DOI: `10.1063/1.2363942`.

60 R. Fontanini, "Spiking neural networks and ferroelectric based synapses for neuromorphic computing," PhD thesis, University of Udine, Jan. 2023.

61 H. W. Park, J. Roh, Y. B. Lee, and C. S. Hwang, "Modeling of negative capacitance in ferroelectric thin films," *Advanced Materials*, vol. 31, no. 32, p. 1 805 266, 2019. DOI: `https://doi.org/10.1002/adma.201805266`.

62 H. W. Park, M. Oh, I. S. Lee, *et al.*, "Double s-shaped polarization – voltage curve and negative capacitance from al2o3-hf0.5zr0.5o2-al2o3 triple-layer structure," *Advanced Functional Materials*, vol. 33, no. 9, p. 2 206 637, 2023. DOI: `https://doi.org/10.1002/adfm.202206637`.

63 L. D. Landau and I. Khalatnikov, "On the anomalous absorption of sound near a second order phase transition point," *Dokl. Akad. Nauk*, vol. 96, pp. 469–472, 1954.

64 S. Salahuddin and S. Datta, "Use of Negative Capacitance to Provide Voltage Amplification for Low Power Nanoscale Devices," *Nano Letters*, vol. 8, no. 2, 2008. DOI: `10.1021/nl071804g`.

65 A. Jain and M. A. Alam, "Stability constraints define the minimum subthreshold swing of a negative capacitance field-effect transistor," *IEEE Transactions on Electron Devices*, vol. 61, no. 7, pp. 2235–2242, 2014. DOI: `10.1109/TED.2013.2286997`.

66 A. I. Khan, U. Radhakrishna, K. Chatterjee, S. Salahuddin, and D. A. Antoniadis, "Negative capacitance behavior in a leaky ferroelectric," *IEEE Transactions on Electron Devices*, vol. 63, no. 11, pp. 4416–4422, 2016.

67 T. Rollo and D. Esseni, "New Design Perspective for Ferroelectric NC-FETs," *IEEE Electron Device Letters*, vol. 39, no. 4, pp. 603–606, 2018. DOI: `10.1109/LED.2018.2795026`.

68 T. Rollo and D. Esseni, "Influence of Interface Traps on Ferroelectric NC-FETs," *IEEE Electron Device Letters*, vol. 39, no. 7, pp. 1100–1103, 2018. DOI: `10.1109/LED.2018.2842087`.

69 S. Pentapati, R. Perumal, S. Khandelwal, M. Hoffmann, S. K. Lim, and A. I. Khan, "Cross-domain optimization of ferroelectric parameters for negative capacitance transistors—part i: Constant supply voltage," *IEEE Transactions on Electron Devices*, vol. 67, no. 1, pp. 365–370, 2020. DOI: `10.1109/TED.2013.2286997`.

70 B. Max, M. Hoffmann, S. Slesazeck, and T. Mikolajick, "Direct correlation of ferroelectric properties and memory characteristics in ferroelectric tunnel junctions," *IEEE Journal of the Electron Devices Society*, vol. 7, pp. 1175–1181, 2019. DOI: `10.1109/JEDS.2019.2932138`.

71 R.Fontanini, J.Barbot, M.Segatto, *et al.*, "Polarization switching and interface charges in BEOL compatible ferroelectric tunnel junctions," in *2021 IEEE 51st European Solid-State Device Research Conference (ESSDERC)*, 2021.

72 H. Mulaosmanovic, S. Dünkel, J. Müller, M. Trentzsch, S. Beyer, E. T. Breyer, T. Mikolajick, and S. Slesazeck, "Impact of read operation on the performance of HfO_2-based ferroelectric fets," *IEEE Electron Device Letters*, vol. 41, no. 9, pp. 1420–1423, 2020. DOI: `10.1109/LED.2020.3007220`.

73 D. Lizzit and D. Esseni, "Operation and design of ferroelectric fets for a beol compatible device implementation," in *ESSDERC 2021 - IEEE 51st European Solid-State Device Research Conference (ESSDERC)*, 2021, pp. 215–218. DOI: `10.1109/ESSDERC53440.2021.9631764`.

74 M. Hoffmann, M. Pešić, S. Slesazeck, U. Schroeder, and T. Mikolajick, "On the stabilization of ferroelectric negative capacitance in nanoscale devices," *Nanoscale*, vol. 10, pp. 10 891–10 899, 23 2018. DOI: `10.1039/C8NR02752H`.

75 P. Lenarczyk and M. Luisier, "Physical modeling of ferroelectric field-effect transistors in the negative capacitance regime," in *2016 International Conference on Simulation of Semiconductor Processes and Devices (SISPAD)*, 2016, pp. 311–314. DOI: `10.1109/SISPAD.2016.7605209`.

76 D. Esseni and R. Fontanini, "Macroscopic and microscopic picture of negative capacitance operation in ferroelectric capacitors," *Nanoscale*, vol. 13, pp. 9641–9650, 21 2021. DOI: `10.1039/D0NR06886A`.

77 Z. Zhou, L. Jiao, J. Zhou, *et al.*, "Time-dependent landau-ginzburg equation-based ferroelectric tunnel junction modeling with dynamic response and multi-domain characteristics," *IEEE Electron Device Letters*, vol. 43, no. 1, pp. 158–161, 2022. DOI: `10.1109/LED.2021.3128998`.

78 Y. Liu, S. Clima, G. Hiblot, P. Matagne, M. L. Popovici, B. Kaczer, D. Velenis, and I. De Wolf, "Investigation of the impact of externally applied out-of-plane stress on ferroelectric fet," *IEEE Electron Device Letters*, vol. 42, no. 2, pp. 264–267, 2021. DOI: `10.1109/LED.2020.3049093`.

79 R. Fontanini, M. Segatto, M. Massarotto, R. Specogna, F. Driussi, M. Loghi, and D. Esseni, "Modeling and design of ftjs as multi-level low energy memristors for neuromorphic computing," *IEEE Journal of the Electron Devices Society*, vol. 9, pp. 1202–1209, 2021. DOI: `10.1109/ JEDS.2021.3120200`.

80 D. J. Griffiths, *Introduction to Quantum Mechanics (2nd Edition)*, 2nd. Pearson Prentice Hall, 2004.

81 S. Takagi, N. Yasuda, and A. Toriumi, "Experimental evidence of inelastic tunneling in stress-induced leakage current," *IEEE Transactions on Electron Devices*, vol. 46, no. 2, pp. 335–341, 1999. DOI: `10.1109/16.740899`.

82 F. Driussi, P. Palestri, and L. Selmi, "Modeling, simulation and design of the vertical graphene base transistor," *Microelectronic Engineering*, vol. 109, pp. 338–341, 2013, Insulating Films on Semiconductors 2013. DOI: `https://doi.org/10.1016/j.mee.2013.03.134`.

83 M. Fukunaga and Y. Noda, "New technique for measuring ferroelectric and antiferroelectric hysteresis loops," *Journal of the Physical Society of Japan*, vol. 77, no. 6, p. 064 706, 2008. DOI: `10.1143/JPSJ.77.064706`.

84 P. D. Lomenzo, P. Zhao, Q. Takmeel, *et al.*, "Ferroelectric phenomena in Si-doped HfO_2 thin films with TiN and Ir electrodes," *Journal of Vacuum Science & Technology B*, vol. 32, no. 3, p. 03D123, 2014. DOI: `10.1116/1.4873323`.

85 V. Mikheev, A. Chouprik, Y. Lebedinskii, S. Zarubin, Y. Matveyev, E. Kondratyuk, M. G. Kozodaev, A. M. Markeev, A. Zenkevich, and D. Negrov, "Ferroelectric second-order memristor," *ACS Applied Materials & Interfaces*, vol. 11, no. 35, pp. 32 108–32 114, 2019, PMID: 31402643. DOI: `10.1021/acsami.9b08189`.

86 H. Ryu, H. Wu, F. Rao, and W. Zhu, "Ferroelectric tunneling junctions based on aluminum oxide/ zirconium-doped hafnium oxide for neuromorphic computing," *Scientific Reports*, vol. 9, no. 1, p. 20 383, 2019. DOI: `10.1038/s41598-019-56816-x`.

87 V. Deshpande, K. S. Nair, M. Holzer, S. Banerjee, and C. Dubourdieu, "Cmos back-end-of-line compatible ferroelectric tunnel junction devices," *Solid-State Electronics*, vol. 186, p. 108 054, 2021. DOI: `https://doi.org/10.1016/j.sse.2021.108054`.

123

88 R. Fontanini, M. Segatto, K. S. Nair, M. Holzer, F. Driussi, I. Häusler, C. T. Koch, C. Dubourdieu, V. Deshpande, and D. Esseni, "Charge-Trapping-Induced Compensation of the Ferroelectric Polarization in FTJs: Optimal Conditions for a Synaptic Device Operation," *IEEE Transactions on Electron Devices*, vol. 69, no. 7, pp. 3694–3699, 2022. DOI: 10.1109/TED.2022.3175684.

89 T. Schenk, U. Schroeder, and T. Mikolajick, "Correspondence - dynamic leakage current compensation revisited," *IEEE Transactions on Ultrasonics, Ferroelectrics, and Frequency Control*, vol. 62, no. 3, pp. 596–599, 2015. DOI: 10.1109/TUFFC.2014.006774.

90 S. K. Arya, B. Kaur, G. Kaur, and K. Singh, "Optical and thermal properties of (70-x) SiO2-xNa2o-15CaO-10Al2O3-5TiO2 (10 ≤ x ≤ 25) glasses," *Journal of Thermal Analysis and Calorimetry*, vol. 120, no. 2, pp. 1163–1171, 2015. DOI: 10.1007/s10973-015-4392-8.

91 W. Zheng, K. H. Bowen, J. Li, I. Dabkowska, and M. Gutowski, "Electronic structure differences in ZrO2 vs HfO2," *The Journal of Physical Chemistry A*, vol. 109, no. 50, pp. 11 521–11 525, 2005. DOI: 10.1021/jp053593e.

92 S. A. Vitale, J. Kedzierski, P. Healey, P. W. Wyatt, and C. L. Keast, "Work-function-tuned tin metal gate fdsoi transistors for subthreshold operation," *IEEE Transactions on Electron Devices*, vol. 58, no. 2, pp. 419–426, 2011. DOI: 10.1109/TED.2010.2092779.

93 H.-J. Lee, M. Lee, K. Lee, J. Jo, H. Yang, Y. Kim, S. C. Chae, U. Waghmare, and J. H. Lee, "Scale-free ferroelectricity induced by flat phonon bands in HfO$_2$," *Science*, vol. 369, no. 6509, pp. 1343–1347, 2020. DOI: 10.1126/science.aba0067.

94 M. Kobayashi, N. Ueyama, K. Jang, and T. Hiramoto, "Experimental Study on Polarization-Limited Operation Speed of Negative Capacitance FET with Ferroelectric HfO$_2$," in *2016 IEEE International Electron Devices Meeting (IEDM)*, 2016, pp. 314–317.

95 J. A. T. Kim and D. A. Antoniadis, "Dynamics of HfZrO$_2$ Ferroelectric Structures: Experiments and Models," in *2020 IEEE International Electron Devices Meeting (IEDM)*, 2020, pp. 441–444.

96 H. Schroeder, "Poole-Frenkel-effect as dominating current mechanism in thin oxide films—An illusion?!" *Journal of Applied Physics*, vol. 117, no. 21, p. 215 103, 2015. DOI: 10.1063/1.4921949.

97 H. W. Park, S. D. Hyun, I. S. Lee, S. H. Lee, Y. B. Lee, M. Oh, B. Y. Kim, S. G. Ryoo, and C. S. Hwang, "Polarizing and depolarizing charge injection through a thin dielectric layer in a ferroelectric–dielectric bilayer," *Nanoscale*, vol. 13, pp. 2556–2572, 4 2021. DOI: `10.1039/D0NR07597C`.

98 J. Li, Y. Qu, M. Si, X. Lyu, and P. D. Ye, "Multi-Probe characterization of ferroelectric/dielectric interface by C-V, P-V and conductance methods," in *2020 IEEE Symposium on VLSI Technology*, 2020, pp. 1–2. DOI: `10.1109/VLSITechnology18217.2020.9265069`.

99 Y. Qu, J. Li, M. Si, X. Lyu, and P. D. Ye, "Quantitative characterization of interface traps in ferroelectric/dielectric stack using conductance method," *IEEE Transactions on Electron Devices*, vol. 67, no. 12, pp. 5315–5321, 2020. DOI: `10.1109/TED.2020.3034564`.

100 S. Deng, Z. Jiang, S. Dutta, H. Ye, W. Chakraborty, S. Kurinec, S. Datta, and K. Ni, "Examination of the Interplay Between Polarization Switching and Charge Trapping in Ferroelectric FET," in *2020 IEEE International Electron Devices Meeting (IEDM)*, 2020, pp. 4.4.1–4.4.4. DOI: `10.1109/IEDM13553.2020.9371999`.

101 M. Massarotto, F. Driussi, A. Affanni, S. Lancaster, S. Slesazeck, T. Mikolajick, and D. Esseni, "Versatile experimental setup for ftj characterization," *Solid-State Electronics*, vol. 194, p. 108 364, 2022. DOI: `https://doi.org/10.1016/j.sse.2022.108364`.

102 K. Toprasertpong, M. Takenaka, and S. Takagi, "Direct observation of interface charge behaviors in FeFET by quasi-static split C-V and hall techniques: Revealing FeFET operation," in *2019 IEEE International Electron Devices Meeting (IEDM)*, 2019, pp. 23.7.1–23.7.4. DOI: `10.1109/IEDM19573.2019.8993664`.

103 P. Marton, I. Rychetsky, and J. Hlinka, "Domain walls of ferroelectric $BaTiO_3$ within the ginzburg-landau-devonshire phenomenological model," *Phys. Rev. B*, vol. 81, p. 144 125, 14 2010. DOI: `10.1103/PhysRevB.81.144125`.

104 S. Zhao, F. Tian, H. Xu, *et al.*, "Experimental extraction and simulation of charge trapping during endurance of fefet with tin/hfzro/sio2/si (mfis) gate structure," *IEEE Transactions on Electron Devices*, vol. 69, no. 3, pp. 1561–1567, 2022. DOI: `10.1109/TED.2021.3139285`.

105 U. Schroeder, M. Materano, T. Mittmann, P. D. Lomenzo, T. Mikolajick, and A. Toriumi, "Recent progress for obtaining the ferroelectric phase in hafnium oxide based films: Impact of oxygen and zirconium," *Japanese Journal of Applied Physics*, vol. 58, no. SL, SL0801, 2019. DOI: `10.7567/1347-4065/ab45e3`.

106 C. Kittel, "Theory of Antiferroelectric Crystals," *Phys. Rev.*, vol. 82, pp. 729–732, 5 1951. DOI: `10.1103/PhysRev.82.729`.

107 C. A. Randall, Z. Fan, I. Reaney, L.-Q. Chen, and S. Trolier-McKinstry, "Antiferroelectrics: History, fundamentals, crystal chemistry, crystal structures, size effects, and applications," *Journal of the American Ceramic Society*, vol. 104, no. 8, pp. 3775–3810, 2021. DOI: `https://doi.org/10.1111/jace.17834`.

108 M. Pešić, M. Hoffmann, C. Richter, T. Mikolajick, and U. Schroeder, "Nonvolatile Random Access Memory and Energy Storage Based on Antiferroelectric Like Hysteresis in ZrO_2," *Advanced Functional Materials*, vol. 26, no. 41, pp. 7486–7494, 2016. DOI: `https://doi.org/10.1002/adfm.201603182`.

109 E. Yurchuk, S. Mueller, D. Martin, *et al.*, "Origin of the endurance degradation in the novel HfO_2-based 1T ferroelectric non-volatile memories," in *2014 IEEE International Reliability Physics Symposium*, 2014, 2E.5.1–2E.5.5. DOI: `10.1109/IRPS.2014.6860603`.

110 M. Pesic, F. P. G. Fengler, S. Slesazeck, U. Schroeder, T. Mikolajick, L. Larcher, and A. Padovani, "Root cause of degradation in novel HfO_2-based ferroelectric memories," in *2016 IEEE International Reliability Physics Symposium (IRPS)*, 2016, MY-3-1-MY-3–5. DOI: `10.1109/IRPS.2016.7574619`.

111 M. Pešić, F. P. G. Fengler, L. Larcher, *et al.*, "Physical Mechanisms behind the Field-Cycling Behavior of HfO_2-Based Ferroelectric Capacitors," *Advanced Functional Materials*, vol. 26, no. 25, pp. 4601–4612, 2016. DOI: `10.1002/adfm.201600590`.

112 M. H. Park, H. J. Kim, Y. J. Kim, T. Moon, K. D. Kim, and C. S. Hwang, "Thin $Hf_xZr_{1-x}O_2$ Films: A New Lead-Free System for Electrostatic Supercapacitors with Large Energy Storage Density and Robust Thermal Stability," *Advanced Energy Materials*, vol. 4, no. 16, p. 1 400 610, 2014. DOI: `https://doi.org/10.1002/aenm.201400610`.

113 X. J. Lou, "Why do antiferroelectrics show higher fatigue resistance than ferroelectrics under bipolar electrical cycling?" *Applied Physics Letters*, vol. 94, no. 7, p. 072 901, 2009. DOI: `10.1063/1.3082375`.

114 L. Zhou, R. Z. Zuo, G. Rixecker, A. Zimmermann, T. Utschig, and F. Aldinger, "Electric fatigue in antiferroelectric ceramics induced by bipolar electric cycling," *Journal of Applied Physics*, vol. 99, no. 4, p. 044 102, 2006. DOI: `10.1063/1.2172725`.

115 S. E. Reyes-Lillo, K. F. Garrity, and K. M. Rabe, "Antiferroelectricity in thin-film ZrO_2 from first principles," *Phys. Rev. B*, vol. 90, p. 140 103, 14 2014. DOI: `10.1103/PhysRevB.90.140103`.

116 M. Hoffmann, Z. Wang, N. Tasneem, *et al.*, "Antiferroelectric negative capacitance from a structural phase transition in zirconia," *Nature Communications*, vol. 13, no. 1, p. 1228, 2022. DOI: `10.1038/s41467-022-28860-1`.

117 E. Sawaguchi, H. Maniwa, and S. Hoshino, "Antiferroelectric Structure of Lead Zirconate," *Phys. Rev.*, vol. 83, pp. 1078–1078, 5 1951. DOI: `10.1103/PhysRev.83.1078`.

118 A. N. Morozovska, E. A. Eliseev, A. Biswas, N. V. Morozovsky, and S. V. Kalinin, "Effect of Surface Ionic Screening on Polarization Reversal and Phase Diagrams in Thin Antiferroelectric Films for Information and Energy Storage," *Phys. Rev. Applied*, vol. 16, p. 044 053, 4 2021. DOI: `10.1103/PhysRevApplied.16.044053`.

119 C.-T. Tung, S. Salahuddin, and C. Hu, "A Compact Model of Antiferroelectric Capacitor," *IEEE Electron Device Letters*, vol. 43, no. 2, pp. 316–318, 2022. DOI: `10.1109/LED.2021.3135001`.

120 Z. Wang, J. Hur, N. Tasneem, W. Chern, S. Yu, and A. Khan, "Extraction of preisach model parameters for fluorite-structure ferroelectrics and antiferroelectrics," *Scientific Reports*, vol. 11, no. 1, p. 12 474, 2021. DOI: `10.1038/s41598-021-91492-w`.

121 J. Müller, T. S. Böscke, U. Schröder, S. Mueller, D. Bräuhaus, U. Böttger, L. Frey, and T. Mikolajick, "Ferroelectricity in Simple Binary ZrO_2 and HfO_2," *Nano Letters*, vol. 12, no. 8, pp. 4318–4323, 2012, PMID: 22812909. DOI: `10.1021/nl302049k`.

122 S. Lombardo, C. Nelson, K. Chae, *et al.*, "Atomic-Scale Imaging of Polarization Switching in an (Anti-)Ferroelectric Memory Material: Zirconia (ZrO_2)," in *2020 IEEE Symposium on VLSI Technology*, 2020, pp. 1–2. DOI: `10.1109/VLSITechnology18217.2020.9265091`.

123 T. Rollo and D. Esseni, "Energy Minimization and Kirchhoff's Laws in Negative Capacitance Ferroelectric Capacitors and MOSFETs," *IEEE Electron Device Letters*, vol. 38, no. 6, pp. 814–817, 2017. DOI: `10.1109/LED.2017.2691002`.

124 X. Luo, K. Toprasertpong, M. Takenaka, and S. Takagi, "Antiferroelectric properties of ZrO_2 ultra-thin films prepared by atomic layer deposition," *Applied Physics Letters*, vol. 118, no. 23, p. 232 904, 2021. DOI: 10.1063/5.0051068.

125 A. P. Levanyuk, B. A. Strukov, and A. Cano, "Background dielectric permittivity: Material constant or fitting parameter?" *Ferroelectrics*, vol. 503, no. 1, pp. 94–103, 2016. DOI: 10.1080/00150193.2016.1218245.

126 P. D. Lomenzo, M. Materano, C. Richter, R. Alcala, T. Mikolajick, and U. Schroeder, "A Gibbs energy view of double hysteresis in ZrO_2 and Si-doped HfO_2," *Applied Physics Letters*, vol. 117, no. 14, p. 142 904, 2020. DOI: 10.1063/5.0018199.

127 Y. Xu, Y. Yang, S. Zhao, *et al.*, "Improved multibit storage reliability by design of ferroelectric modulated antiferroelectric memory," *IEEE Transactions on Electron Devices*, vol. 69, no. 4, pp. 2145–2150, 2022. DOI: 10.1109/TED.2021.3139054.

128 M. Segatto, R. Fontanini, F. Driussi, D. Lizzit, and D. Esseni, "Limitations to Electrical Probing of Spontaneous Polarization in Ferroelectric-Dielectric Heterostructures," *IEEE Journal of the Electron Devices Society*, vol. 10, pp. 324–333, 2022. DOI: 10.1109/JEDS.2022.3164652.

129 H.-J. Lee, M. Lee, K. Lee, J. Jo, H. Yang, Y. Kim, S. C. Chae, U. Waghmare, and J. H. Lee, "Scale-free ferroelectricity induced by flat phonon bands in HfO_2," *Science*, vol. 369, no. 6509, pp. 1343–1347, 2020. DOI: 10.1126/science.aba0067.

130 R. Cao, Y. Wang, S. Zhao, Y. Yang, X. Zhao, W. Wang, X. Zhang, H. Lv, Q. Liu, and M. Liu, "Effects of capping electrode on ferroelectric properties of $Hf_{0.5}Zr_{0.5}O_2$ thin films," *IEEE Electron Device Letters*, vol. 39, no. 8, pp. 1207–1210, 2018. DOI: 10.1109/LED.2018.2846570.

131 B. S. Kim, S. D. Hyun, T. Moon, *et al.*, "A Comparative Study on the Ferroelectric Performances in Atomic Layer Deposited $Hf_{0.5}Zr_{0.5}O_2$ Thin Films Using Tetrakis(ethylmethylamino) and Tetrakis(dimethylamino) Precursors," *Nanoscale Research Letters*, vol. 15, no. 1, p. 72, 2020. DOI: 10.1186/s11671-020-03301-4.

132 K. Kato, T. Saito, S. Shibayama, M. Sakashita, W. Takeuchi, N. Taoka, O. Nakatsuka, and S. Zaima, "Stabilized formation of tetragonal ZrO_2 thin film with high permittivity," *Thin Solid Films*, vol. 557, pp. 192–196, 2014, The 8th International Conference on Silicon Epitaxy and Heterostructures (ICSI-8) and the 6th International Symposium on

Control of Semiconductor Interfaces (ISCSI-VI). DOI: `https://doi.org/10.1016/j.tsf.2014.01.031`.

133 J. Liu, J. Li, J. Wu, and J. Sun, "Structure and Dielectric Property of High-k ZrO_2 Films Grown by Atomic Layer Deposition Using Tetrakis(Dimethylamido)Zirconium and Ozone," *Nanoscale Research Letters*, vol. 14, no. 1, p. 154, 2019. DOI: `10.1186/s11671-019-2989-8`.

134 M. Si, X. Lyu, P. R. Shrestha, X. Sun, H. Wang, K. P. Cheung, and P. D. Ye, "Ultrafast measurements of polarization switching dynamics on ferroelectric and anti-ferroelectric hafnium zirconium oxide," *Applied Physics Letters*, vol. 115, no. 7, p. 072 107, 2019. DOI: `10.1063/1.5098786`.

135 R. Meyer, R. Waser, K. Prume, T. Schmitz, and S. Tiedke, "Dynamic leakage current compensation in ferroelectric thin-film capacitor structures," *Applied Physics Letters*, vol. 86, no. 14, p. 142 907, 2005. DOI: `10.1063/1.1897425`.

136 A. K. Saha and S. K. Gupta, "Multi-Domain Negative Capacitance Effects in Metal-Ferroelectric-Insulator-Semiconductor/Metal Stacks: A Phase-field Simulation Based Study," *Scientific Reports*, vol. 10, no. 1, p. 10 207, 2020. DOI: `10.1038/s41598-020-66313-1`.

137 A. K. Saha and S. K. Gupta, "Negative capacitance effects in ferroelectric heterostructures: A theoretical perspective," *Journal of Applied Physics*, vol. 129, no. 8, p. 080 901, 2021. DOI: `10.1063/5.0038971`.

138 T. S. Böscke, J. Müller, D. Bräuhaus, U. Schröder, and U. Böttger, "Ferroelectricity in hafnium oxide: CMOS compatible ferroelectric field effect transistors," in *2011 International Electron Devices Meeting*, Dec. 2011, pp. 24.5.1–24.5.4. DOI: `10.1109/IEDM.2011.6131606`.

139 S. Fichtner, N. Wolff, F. Lofink, L. Kienle, and B. Wagner, "AlScN: A III-V semiconductor based ferroelectric," *Journal of Applied Physics*, vol. 125, no. 11, p. 114 103, 2019. DOI: `10.1063/1.5084945`.

140 T. Mikolajick, U. Schroeder, P. D. Lomenzo, E. T. Breyer, H. Mulaosmanovic, M. Hoffmann, T. Mittmann, F. Mehmood, B. Max, and S. Slesazeck, "Next generation ferroelectric memories enabled by hafnium oxide," in *2019 IEEE International Electron Devices Meeting (IEDM)*, 2019, pp. 15.5.1–15.5.4. DOI: `10.1109/IEDM19573.2019.8993447`.

141 Y. W. So, D. J. Kim, T. W. Noh, J.-G. Yoon, and T. K. Song, "Polarization switching kinetics of epitaxial Pb(Zr0.4Ti0.6)O3 thin films," *Applied Physics Letters*, vol. 86, no. 9, p. 092 905, Feb. 2005. DOI: `10.1063/1.1870126`.

142 W. J. Merz, "Domain formation and domain wall motions in ferroelectric batiO₃ single crystals," *Phys. Rev.*, vol. 95, pp. 690–698, 3 Aug. 1954. DOI: `10.1103/PhysRev.95.690`.

143 Z. Li, C.-B.-W. Li, H.-C. Thong, Y.-Q. Jiang, J. Xu, Y. Hao, C.-F. Wu, Z. Dou, K. Bi, and K. Wang, "Grain size effect on piezoelectric properties of rhombohedral lead zirconate titanate ceramics," *Ceramics International*, vol. 49, no. 17, Part A, pp. 27733–27741, 2023. DOI: `https://doi.org/10.1016/j.ceramint.2023.05.209`.

144 J. Y. Jo, H. S. Han, J.-G. Yoon, T. K. Song, S.-H. Kim, and T. W. Noh, "Domain switching kinetics in disordered ferroelectric thin films," *Phys. Rev. Lett.*, vol. 99, p. 267602, 26 Dec. 2007. DOI: `10.1103/PhysRevLett.99.267602`.

145 M. Thesberg, M. N. K. Alam, B. Truijen, B. Kaczer, P. J. Roussel, Z. Stanojević, O. Baumgartner, F. Schanovsky, M. Karner, and H. Kosina, "On the modeling of polycrystalline ferroelectric thin films: Landau-based models versus monte carlo-based models versus experiment," *IEEE Transactions on Electron Devices*, vol. 69, no. 6, pp. 3105–3112, 2022. DOI: `10.1109/TED.2022.3167942`.

146 A. K. Saha and S. K. Gupta, "Multi-domain negative capacitance effects in metal-ferroelectric-insulator-semiconductor/metal stacks: A phase-field simulation based study," *Scientific Reports*, vol. 10, no. 1, p. 10207, 2020. DOI: `10.1038/s41598-020-66313-1`.

147 N. Siannas, C. Zacharaki, P. Tsipas, S. Chaitoglou, L. Bégon-Lours, C. Istrate, L. Pintilie, and A. Dimoulas, "Metastable ferroelectricity driven by depolarization fields in ultrathin hf0.5zr0.5o2," *Communications Physics*, vol. 5, no. 1, p. 178, 2022. DOI: `10.1038/s42005-022-00951-x`.

148 Y. Qi and K. M. Rabe, "Phase competition in HfO₂ with applied electric field from first principles," *Phys. Rev. B*, vol. 102, p. 214108, 21 2020. DOI: `10.1103/PhysRevB.102.214108`.

149 D.-H. Choe, S. Kim, T. Moon, S. Jo, H. Bae, S.-G. Nam, Y. S. Lee, and J. Heo, "Unexpectedly low barrier of ferroelectric switching in hfo2 via topological domain walls," *Materials Today*, vol. 50, pp. 8–15, 2021. DOI: `https://doi.org/10.1016/j.mattod.2021.07.022`.

150 D. H. Lee, G. T. Yu, J. Y. Park, S. H. Kim, K. Yang, G. H. Park, J. J. Ryu, J. I. Lee, G. H. Kim, and M. H. Park, "Effect of residual impurities on polarization switching kinetics in atomic-layer-deposited

ferroelectric $hf_{0.5}zr_{0.5}o_2$ thin films," *Acta Materialia*, vol. 222, p. 117 405, 2022. DOI: https://doi.org/10.1016/j.actamat.2021.117405.

151   S. Zhou, L. You, H. Zhou, Y. Pu, Z. Gui, and J. Wang, "Van der waals layered ferroelectric cuinp2s6: Physical properties and device applications," *Frontiers of Physics*, vol. 16, no. 1, p. 13 301, Sep. 2020. DOI: 10.1007/s11467-020-0986-0.

152   I. M. Gelfand and S. Fomin, *Calculus of Variations*. Prentice-Hall INC, Upper Saddle River, NJ, 1964.

153   M. Hoffmann, M. Pešić, S. Slesazeck, U. Schroeder, and T. Mikolajick, "On the stabilization of ferroelectric negative capacitance in nanoscale devices," *Nanoscale*, vol. 10, pp. 10 891–10 899, 23 2018. DOI: 10.1039/C8NR02752H.

154   A. Strauch, B. März, T. Denneulin, M. Cattaneo, A. Rosenauer, and K. Müller-Caspary, "Systematic Errors of Electric Field Measurements in Ferroelectrics by Unit Cell Averaged Momentum Transfers in STEM," *Microscopy and Microanalysis*, vol. 29, no. 2, pp. 499–511, Feb. 2023. DOI: 10.1093/micmic/ozad016.

155   D. D. Fong, G. B. Stephenson, S. K. Streiffer, J. A. Eastman, O. Auciello, P. H. Fuoss, and C. Thompson, "Ferroelectricity in ultrathin perovskite films," *Science*, vol. 304, no. 5677, pp. 1650–1653, 2004. DOI: 10.1126/science.1098252.

156   S. Ducharme, V. M. Fridkin, A. V. Bune, S. P. Palto, L. M. Blinov, N. N. Petukhova, and S. G. Yudin, "Intrinsic ferroelectric coercive field," *Phys. Rev. Lett.*, vol. 84, pp. 175–178, 1 Jan. 2000. DOI: 10.1103/PhysRevLett.84.175.

157   R. K. Behera, C.-W. Lee, D. Lee, A. N. Morozovska, S. B. Sinnott, A. Asthagiri, V. Gopalan, and S. R. Phillpot, "Structure and energetics of 180° domain walls in pbtio3 by density functional theory," *Journal of Physics: Condensed Matter*, vol. 23, no. 17, p. 175 902, Apr. 2011. DOI: 10.1088/0953-8984/23/17/175902.

158   D. Pantel, Y.-H. Chu, L. W. Martin, R. Ramesh, D. Hesse, and M. Alexe, "Switching kinetics in epitaxial BiFeO3 thin films," *Journal of Applied Physics*, vol. 107, no. 8, p. 084 111, Apr. 2010. DOI: 10.1063/1.3392884.

159   S. Takagi, N. Yasuda, and A. Toriumi, "Experimental evidence of inelastic tunneling in stress-induced leakage current," *IEEE Transactions on Electron Devices*, vol. 46, no. 2, pp. 335–341, 1999. DOI: 10.1109/16.740899.

160   R. Fontanini, J. Barbot, M. Segatto, *et al.*, "Interplay between charge trapping and polarization switching in beol-compatible bilayer ferroelectric tunnel junctions," *IEEE Journal of the Electron Devices Society*, vol. 10, pp. 593–599, 2022. DOI: 10.1109/JEDS.2022.3171217.

161   D. Esseni, L. Selmi, and P. Palestri, *Nanoscale MOS Transistors*. Cambridge University Press, 2011.

Acknowledgements